Synthesis, Characterization, and Growth Mechanism of Single-Walled Metal Oxide Nanotubes

A Dissertation
Presented to
the Academic Faculty

by

SANJOY MUKHERJEE

In Partial Fulfillment
of the Requirements for the Degree
Doctor of Philosophy in Chemical Engineering in the
School of Chemical and Biomolecular Engineering

Georgia Institute of Technology
August 2007

Synthesis, Characterization, and Growth Mechanism of

Single-Walled Metal Oxide Nanotubes

Approved by:

Dr. Sankar Nair, Advisor
School of Chemical and Biomolecular Engineering
Georgia Institute of Technology

Dr. Christopher W. Jones
School of Chemical and Biomolecular Engineering
Georgia Institute of Technology

Dr. Haskell W. Beckham
School of Polymer, Textile and Fiber Engineering
Georgia Institute of Technology

Dr. William J. Koros
School of Chemical and Biomolecular Engineering
Georgia Institute of Technology

Dr. Peter J. Hesketh
School of Mechanical Engineering
Georgia Institute of Technology

Date Approved: June 29th. 2007

Acknowledgements

I would like to express my sincerest gratitude to my advisor, Prof. Sankar Nair, for taking me on as his student and extending continuous encouragement, support and guidance. His support has been instrumental in keeping me motivated during moments of doubt and frustration. I would also like to thank Prof. Haskell Beckham, Prof. Peter Hesketh, Prof. Chris Jones, and Prof. William Koros for serving on my committee and providing valuable suggestions during this work. I am grateful to the Georgia Institute of Technology and the American Chemical Society for financial support of this research.

I wish to thank Dr. Yolande Berta for her assistance in the Transmission Electron Microscopy Center. I would also like to express my gratitude to Dr. Ashwini Sinha for his help with the X-ray Photoelectron Spectroscopy, Rebecca Shiels and Dr. Henry Cheng for their assistance with Nitrogen Adsorption measurements, and Yeny Hudiono and Dr. Weontae Oh for their assistance in AFM and X-ray Reflectivity measurements. I thank my friends Dr. Pratyay Basak, Suchitra Konduri, Yeny Hudiono, Paul Wissmann, Jason Hicks, John Richardson, and Mita Das for all their support.

The most important support has come from my parents, who have always stood beside me. I wish to thank my wife, Urbi, for offering her wholehearted support. I am also thankful to my grandparents for their blessings and my sister (Didi) for her constant encouragement. I have received moral support from every member of my family; they have always had great faith in me and have supported me during every step of my life.

Table of Contents

List of Tables

List of Figures

Summary

Nanotubes have numerous potential applications in areas such as biotechnology, electronics, photonics, catalysis and separations. Even though the unique shape, size and other structural features of nanotubes make them attractive for nanotechnological applications, there are several challenges to be overcome in order to realize their potential, such as: (1) Synthesis of monodisperse (in diameter and in length) single-walled nanotubes; (2) Quantitative understanding of the mechanism of formation and growth of nanotubes for development of novel functional materials; (3) Capability to engineer the nanotube size; (4) Low temperature synthesis process, preferably in aqueous phase; and (5) Synthesis of impurity free nanotubes.

Our investigation focuses on a class of metal oxide (aluminosilicate/germanate) nanotubes, which we propose as attractive nanotube materials for a number of reasons. They are single walled nanotubes with monodisperse inner and outer diameters, which can be synthesized in the laboratory by a low temperature (95ºC) process from mildly acidic aqueous solutions of aluminate and silicate precursors. The nanotubes can be obtained in pure form. Furthermore, the formation of the nanotubes from their precursors occurs on a time scale of hours, which makes it convenient as a model system to study the mechanisms of nanotube formation, and thus obtain new insights that address the nanotube science and engineering challenges enumerated above.

This work is focused on obtaining a qualitative and quantitative understanding of the mechanism of formation of aluminosilicate and aluminogermanate nanotubes. Understanding of the self-assembly, nucleation and growth of such a model system would enable precise predictive control of synthesis parameters for a wider range of nanoscale materials. This work is also focused on precise control of nanotube dimensions (length and diameter). In order to achieve this overall objective, this thesis consists of the following aspects:

(I) A systematic phenomenological study of the growth and structural properties of aluminosilicate and aluminogermanate nanotubes. The evolution of the aqueous-phase nanotube synthesis process over a period of 5 days, was carefully analyzed by a number of qualitative and quantitative characterization tools. In particular, the time-dependence of the nanotube size, structure, and solid-state packing was followed using electron microscopy, electron diffraction, X-ray diffraction, and dynamic light scattering. The essentially constant size and structure of the nanotubes over their entire synthesis time, the increasing nanotube concentration over the synthesis time, and the absence of significant polydispersity, strongly suggest that these nanotubular inorganic macromolecules are assembled through a thermodynamically controlled self-assembly process, rather than a kinetically controlled growth/polymerization process.

(II) Investigation of the mechanism of formation of single-walled aluminogermanate nanotubes and development of key insights into the process of hydrolysis and self-assembly of metal oxides in mildly acidic aqueous solutions. Here we employ solution-

phase and solid-state characterization tools to elucidate such a mechanism, particularly that governing the formation of short (20 nm), ordered, monodisperse (3.3 nm diameter), aluminum-germanium-hydroxide ('aluminogermanate') nanotubes in aqueous solution. The central phenomena underlying this mechanism are: (1) the generation (*via* pH control) of a precursor solution containing aluminate and germanate precursors chemically bonded to each other, (2) the formation of amorphous nanoscale (~ 6 nm) condensates *via* temperature control, and (3) the self-assembly of short nanotubes from the amorphous nanoscale condensates. This mechanism provides a model for controlled low-temperature assembly of small, monodisperse, ordered nanotube objects.

(III) Synthesis of mixed metal oxide (aluminosilicogermanate) nanotubes with precise control of elemental composition of the product nanotubes. Here we demonstrate that with the use of compositional control, we can precisely control the dimensions (external diameter and length) of the nanotubes.

(IV) Preliminary work towards generalization of the kinetic model developed for aluminogermanate nanotubes to a larger class of metal oxide nanotubes. It was found that the size of nanotubes is dependent on the amount of precursors that can be packed in a single ANP and in turn depends on the size of the ANP. With a simple calculation we have estimated that the diameter of ANP required to pack enough precursor material to make a 90 nm nanotube is 10 nm, and which is close to the value predicted by the kinetic model (12 nm). Furthermore, it is found that nanotube concentration is independent of

nanotube composition since the activation energy barrier for the formation of nanotubes from ANP is independent of composition.

This research therefore addresses three critical issues: It firstly explains how nanotube formation and growth occurs by self-assembly mechanisms in aqueous solutions, it secondly provides a kinetic and thermodynamic rationale for the mechanism, and it thirdly aims at generalizing the mechanism for applicability to a wide variety of systems. Understanding the growth mechanism is an important aspect of developing a synthetic method for generating nanotubes of desired material, size, and morphology. Unfortunately, syntheses of many nanoscale materials have been attempted without satisfactory knowledge of the underlying mechanism. Such an approach has a low probability of success when attempt to construct nanoscale objects of the level of structural complexity described in the following chapters. The present work imparts some basic conceptual, experimental, and theoretical tools and methodologies to assess the effects of experimental parameters that control the size, shape, and monodispersity of the nanotubes, and suggests future directions for research based on the results of the present work.

Chapter 1 : Introduction and Background

Nanotechnology has emerged as a promising vehicle for an emerging scientific and technological revolution [1-3]. Richard Feynman, in his seminal 1959 lecture [4], proposed a variety of potential nanomachines, which could be engineered to a higher level of functional efficiency than currently available manufactured devices by exploiting changes in the behavior of matter at the nanometer length scale. In order to realize this goal, scientists and engineers have to devise strategies to synthesize specified functional nanoparticles, and then learn how to incorporate them into devices in which they might function individually or in cooperation with other nanoparticles or devices. This "bottom up" approach of "nanoparticle design" followed by "device assembly from nanoparticles" is widely accepted as a promising route to nanotechnological applications, separate from a more traditional "top down" approach followed in semiconductor and electronics research. In recent years, "bottom up" nanotechnology has led to promising innovations in fields such as biotechnology [2, 5], electronics [6] and catalysis [1, 7]. This approach also could potentially address the ever-present need to miniaturize components, especially in the electronics industry.

Today it is widely accepted that reduction in size to a molecular level (nanometer scale) cannot be achieved with conventional "top down" methods (e.g. photolithography, etching etc) [1, 3, 5]. Thus, nanoparticle-based (or "single-molecule" based) device development is emerging as a fundamental requirement in realizing the goals of nanotechnology. Single-molecule devices can be faster, more precise, and more efficient

in energy utilization than devices made of bulk materials. Single functional molecules like molecular rectifiers were first designed and assembled [8-10] in IBM research laboratories. Numerous molecules having electronic properties have hence been identified and reported [11]. Single molecule logic gates and circuits have been theorized and detailed molecular designs have been put forward for actualization and incorporation in solid state electronics [6, 12-16]. Biotechnology is also stressing the need for nanoscale devices for a variety of applications, notably in DNA sequencing and biosensing [17, 18].

Single molecule devices require not only the creation of functional molecules but also substrates and platforms; i.e. the support systems that allow the active molecules to function with high efficiency and minimal degradation over time. In an enzyme, the "active centers" (biocatalytic sites) may be just a few tens of atoms in dimension, but are incorporated in a support protein of much larger size so that the active centers are stabilized and can perform efficiently in the desired environment. The nanometer scale of these structural features offers unique engineering challenges. First, there is little quantitative understanding of the processes governing the controlled synthesis of important synthetic nanoscale materials like nanotubes, nanowires and nanodots which could be used (in the form of sub-100-nm macromolecules) as components of such devices [1]. However, knowledge of these processes is essential for rational design of nanodevices, since fine control over dimensions, structure, and composition is key to producing nanomaterials suitable for incorporation in devices. Additionally, the properties of any nanoscale system are controlled by "molecular" physics and

confinement effects as opposed to "bulk" physics, and it is well known that the functional properties of nanomaterials are usually very different from the corresponding bulk materials. Once the synthesis-structure-size-shape-property relations of a nanoparticle are accurately determined, one can begin to rationally address the next set of problems such as manipulation of the nanoparticle and direction to a specific location in a device, and connection of the device to a larger system or collection of devices. In this work, we focus on synthesis-structure-size-shape-property relations in nanotube materials.

1.1 Nanotubes and Nanotechnology

Nanotubes are defined as hollow cylindrical objects having one or more dimensions within the nanometer regime. Due to their unique shape and size, nanotubular materials [19] are acknowledged as important "building blocks" of a future nanotechnology based on synthesis of functional nanoparticles and their assembly into nanoscale devices with novel applications in areas such as electronics [15], biotechnology [17, 20-25], sensing [26], separations [27], energy storage/management [28] and catalysis [29].

Figure 1-1 classifies nanotubes based on structure and composition. The discovery of carbon nanotubes [30] has stimulated extensive research on the synthesis, properties and applications of nanotubes, with the majority of studies being focused on its novel properties. Carbon nanotubes [24, 30] and their inorganic analogues (e.g., boron nitride and tungsten disulfide nanotubes) [31-33] continue to be extensively studied.

However, several problems in these nanotube technology remain to be overcome, e.g. the development of a low-temperature synthetic process with high yield as well as precise control over the nanotube dimensions and chirality, limitations of chemical composition, and the production of 'three-dimensionally nanoscale' nanotube objects (i.e., single-walled objects smaller than 10 nm in both length and cross-section). Inorganic oxide nanotubes [31, 34-38], on the other hand, are emerging as attractive materials due to their potentially wide range of tunable compositions and properties accessible by low-temperature solution-phase chemistry.

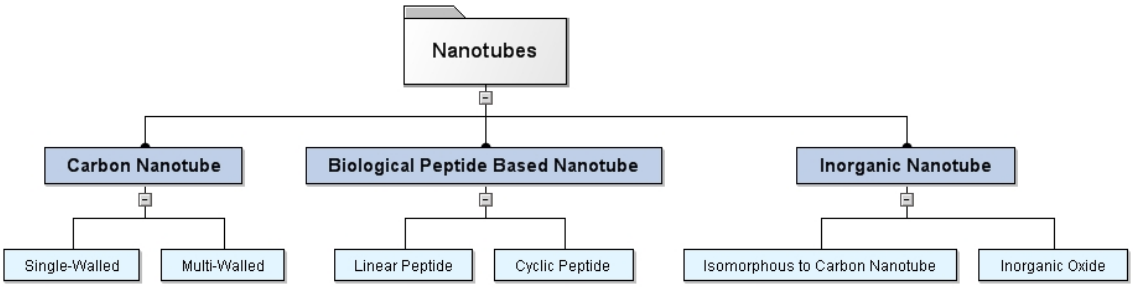

Figure 1-1: Classification of nanotubes based on their structure and composition.

An important goal of nanotube science and technology is the development of a low temperature synthetic process with precise control (at sub-100-nm length scale and sub-10-nm diameter scale) over nanotube dimensions to produce 'three-dimensionally nanoscale' nanotube objects [24, 39]. This would allow the optimal exploitation of many of their unique properties (e.g., tunable band gaps, ballistic transport of charge/heat/mass, and quantum confinement phenomena) that manifest themselves strongly at these small length scales. A short discussion is presented in the next few sections where these

objective goals of nanotechnology are discussed in the perspective of present nanotube technology.

1.1.1 Carbon and Isomorphous Nanotubes

The discovery of carbon nanotubes [30] has stimulated extensive research on the synthesis, properties and applications of nanotubes, with the majority of studies being focused on the novel properties of carbon nanotubes. There are two main types of structurally perfect carbon nanotubes; Single Walled NanoTubes (SWNT) comprises of a single graphene sheet rolled up to form a cylindrical nanotube and Multi-Walled NanoTubes (MWNT) are arrays of concentrically nested SWNTs (Figure 1-2). Although the nanotubes are structurally identical to a sheet of graphite (a semiconductor with zero band-gap), their properties range from metallic to semiconductor, depending on the sheet direction about which it is rolled to form the nanotube [22]. Furthermore, the nanotubes have superior tensile strength [40] and heat conductivity to that of a graphite sheet. These unique and advantageous properties of carbon nanotubes have inspired numerous investigations into their potential applications.

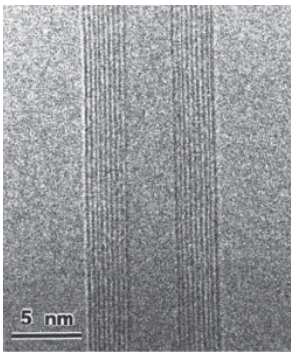

Figure 1-2: Transmission electron microscope image of a carbon MWNT with 9 nested SWNTs. Taken from [22].

Carbon nanotubes are synthesized by methods like arc-discharge, laser ablation and chemical vapor deposition on catalyst particles [41]. The details of these high-temperature (> 500 K) synthesis methods are not the subject of this thesis. The chemical vapor deposition method uses less energy and has lower cost than the other methods, but uses metallic catalysts (such as iron) which are retained by the product nanotubes. This fact may necessitate expensive purification techniques. High purity carbon nanotubes currently cost around $750/g and carbon nanotubes with substantial amounts of impurities costs around $60/g. Carbon nanotubes are commercially manufactured by catalytic gas-phase pyrolysis of heavy hydrocarbons [22]. The products generated by this process have high defect density and have only been used in polymer-nanotube composites to obtained improved mechanical strength. Furthermore, carbon nanotube products are rarely monodisperse and substantial additional cost is incurred in separating nanotubes by size (length and diameter) [42]. The nature of the above synthesis techniques creates difficulties in controlling the synthesis, because the main mechanistic events occur over a very short period of time (~ 1 ms – 1 s). This makes the control over dimensions, composition, folding directions of the graphene sheets, and the number of walls of the product nanotube, very difficult and reliant upon “Edisonian” experimentation.

Many layered inorganic compounds with two dimensional structures have been found [43] to form nanotubes. Isomorphous to carbon nanotubes, these inorganic nanotubes (also called inorganic fullerene-like nanotubes) [31] are being increasingly investigated for nanotechnological applications owing, among several factors, to the vast

range of potential physicochemical properties afforded by inorganic materials. For example, WS_2 nanotubes have been shown to have superior solid lubrication properties. Unlike carbon nanotubes, which are built from a monatomic sheet of graphite, inorganic nanotubes comprise of "molecular" sheets. In the case of WS_2, the repeating structure is the sandwich of three layers of W-S-W, with covalent tetrahedral W-S bonds and weak van der Waals forces holding the adjacent sulfur layers (Figure 1-3). This layered structure is considered as one reason for the much more common observation of multi-walled inorganic nanotubes than carbon nanotubes.

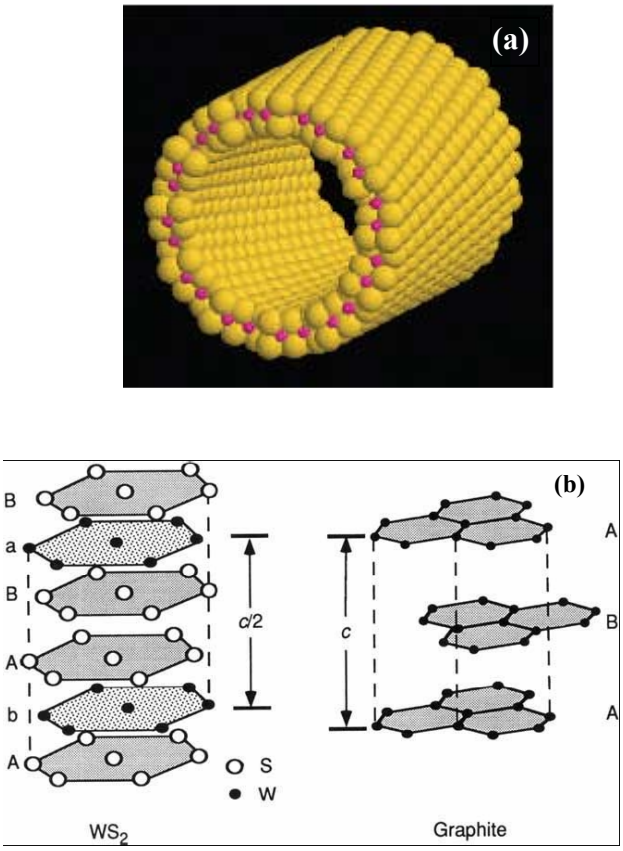

Figure 1-3: (a) Schematic representation of WS_2 nanotube where the pink and yellow atoms are W and S respectively. Taken from [39]. (b) Layered structure of graphite and WS_2. Taken from [43].

Synthesis of layered inorganic nanotubes is achieved by using reactive metal oxide, metal halide, or metal carbonyl precursors. Progress on various synthesis routes are discussed in detail in many reviews [32, 39, 44]. Halides or carbonyls of metals react almost instantaneously with H_2S to form metal sulfide materials. In such a highly reactive environment, there is little scope for rational control over the polydispersity of dimensions, number of walls, defect concentration etc. In recent years, it has been demonstrated that through soft-chemistry, some control over nanotube synthesis can be achieved [45]. Overall, the fullerene-like inorganic nanotubes synthesized to date are polydisperse and/or multiwalled materials [31, 33, 44, 46].

1.1.2 Biomolecular Nanotubes

Biolmolecules like proteins, carbohydrates, and cyclic peptides can self-assemble to form nanotube-like structures. An important feature of biological nanotubes is the possibility of building in molecular recognition capabilities based on well-known interactions between amino acid residues [47, 48]. This feature has enabled researchers to achieve molecular level manipulation of nanomaterials for molecular electronics applications [49] and selective binding for drug delivery applications [50]. Furthermore, peptide and protein based nanotubes are biologically compatible and requires simple lab-scale equipment to synthesize. Disadvantages include their poor temperature stability and sensitivity of their structural integrity to solution conditions.

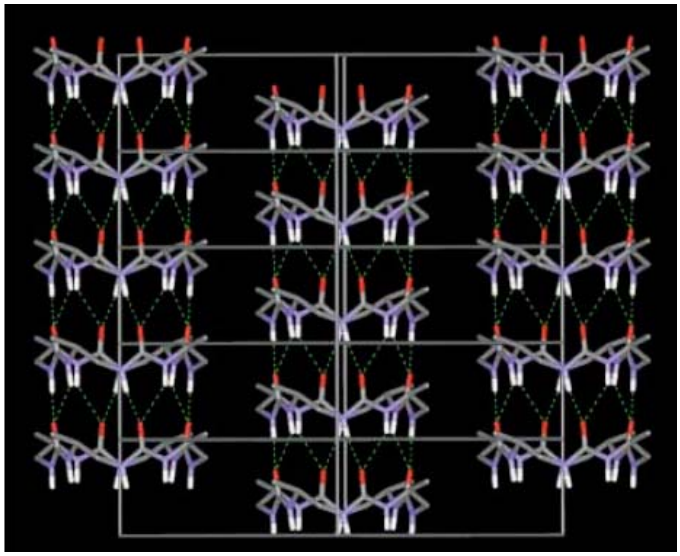

Figure 1-4: Nanotubular organization of a cyclic peptide. The dotted lines represent the hydrogen bonds. The unit cell is shown with grey lines. Taken from [51].

Peptide nanotubes can be assembled from either linear or non-linear peptide monomers [52]. The details of the synthesis processes are beyond the scope of this thesis. Broadly, however, peptide nanotube are formed either by attachment of linear peptides to shape-directing amphiphiles [53] or by self-assembly of cyclic peptides monomers [54, 55]. The later forms nanotubes where the individual units are connected with hydrogen bonds as shown in Figure 1-4. In almost all the peptide nanotubes the stability of the structure is dependent on the pH and temperature of the solution in which it is stored. Absence of covalent bonds between the peptide monomer units makes these structures unstable in the absence of proper solvent pH and temperature. Furthermore, the reagents used in the synthesis are expensive and so the nanotubes are associated with high per unit costs.

1.1.3 Metal Oxide Nanotubes

Metal oxides are a diverse class of materials with a range of technologically important properties. For example, ZnO and TiO_2 have electronic band gaps of 3.4 eV and 3 eV (rutile structure) respectively, and are important in piezoelectric, optoelectronic, photovoltaic, and photochemical applications [56]. In_2O_3 has a band gap of 3.75 eV, which makes it optically transparent and an important material for use in liquid crystal displays [57]. Fe_3O_4 has ferromagnetic properties [58]. The diversity of structure-property relations in metal oxides has led to extensive research on the synthesis of metal oxide nanotubes and nanowires, with the objectives of shrinking the device dimensions and ultimately taking advantage of nanoscale electron confinement effects to further control the properties of these materials [59]. Many important metal oxides, e.g. those of Zn, In, Fe, V, Ti, Cu and Ga, have been synthesized in the form of multi-walled nanotubes [60]. Synthetic metal oxide nanotubes have been successfully demonstrated as field-effect transistors, logic gates, light emission diodes, photodetectors, photovoltaic devices, chemical sensors and field emitters [60].

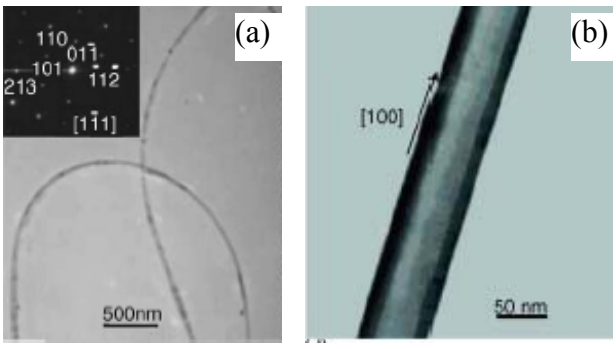

Figure 1-5: (a) Low magnification TEM image with ED inset and (b) High magnification image of α-Fe_2O_3 nanowire. Taken from [61].

Several synthetic processes have been developed for the synthesis of metal oxide nanotubes. They are often synthesized via an evaporation technique, wherein the metal vapor and oxygen gas are contacted over a solid seed material (Vapor-Liquid-Solid process) [62] or a dispersed liquid phase seed material (Vapor-Liquid process) [63]. Vapor-phase syntheses are conducted at high temperature, and offer very little rational control over the dimensions of the resulting structures, because of the number of poorly-understood variables in the synthesis. The products are usually multiwalled and quickly grow beyond nanoscale dimensions [31, 34, 64]. Since the diameter of the inner porous region may be much smaller than the external diameter of the multi-walled material, they are often referred to as nanowires rather than true nanotubes. There has also been development of solution-phase growth methods for multi-walled nanotubes, using templates such as anodic alumina substrates and carbon nanotubes [65]. Recently there has been increasing interest in the synthesis of metal oxide nanotubes from water soluble salts and organic templates by hydrothermal processes [66-68]. Such hydrothermal ("soft" chemistry) processes occur at 200°C to 300°C and slightly above 1 atm pressure. Metal oxide nanotubes like ZnO [68], CuO [69], TiO_2 [70], Fe_2O_3 [71] and In_2O_3 [57] have been synthesized using this process. Although the hydrothermal route offers a low cost process, nanoscale engineering (particularly, control of dimensions and defects) is yet to be achieved since the mechanistic aspects are little understood for these systems [19, 34, 35]. Furthermore, templated approaches have not yielded single-walled metal oxide nanotubes.

Metal oxide nanotubes also encompass a few naturally occurring minerals. Multi-walled nanotubes of minerals like chrysotile (magnesium hydroxide silicate) [72] and kaolinite (aluminosilicate clay) have been discovered [73]. It is notable that Pauling [73] appears to have been the first to speculate on a thermodynamic basis for nanotube formation using the chrysotile model. It was proposed that bond energy mismatches on the inner and outer walls generate a bending strain that might favor a cylindrical rather than flat (layered) material under certain conditions.

1.2 Imogolite: An Metal Oxide Aluminosilicate Nanotube

The natural and synthetic versions of the nanotube mineral imogolite [74] have been investigated to a significant extent over the years [74-79]. In contrast to other metal oxide materials, imogolite is a single-walled nanotube (Figure 1-6). Its wall structure is identical to a layer of aluminum (III) hydroxide (gibbsite); with isolated silicate groups pendent from the inner wall. The nanotube has a periodic wall structure composed of six-membered aluminum hydroxide rings, with a repeat unit of approximately 0.84 nm along the nanotube axis [74]. The empirical formula of imogolite is $(OH)_3Al_2O_3SiOH$. The presence of hydroxyl groups on walls and rims makes the nanotube hydrophilic. Naturally occurring imogolite has an external diameter of around 2.0 nm and an internal diameter of around 1.0 nm [76]. The structural model of imogolite shown in Figure 1-6 was proposed [74-76] based on solid-state NMR, TEM and XRD studies that established its close relation to the layered structure of gibbsite as well as the coordination and environment of the Al and Si atoms.

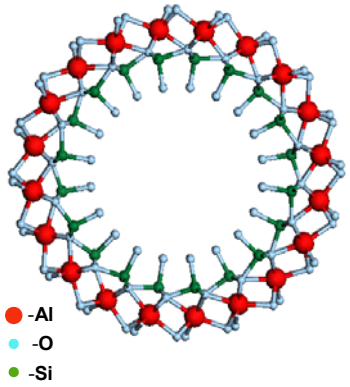

Figure 1-6: Cross sectional view of the aluminosilicate nanotube imogolite.

Synthetic imogolite was prepared [77] from a millimolar aluminosilicate precursor solution at a temperature of 95ºC. The typical solid-state structure consists of nanotube bundles or ropes several microns in length. An aluminogermanate analog (not naturally occurring) has also been successfully synthesized by substitution of silicon with germanium in the synthesis solution [80]. However, from the limited amount of characterization data available, the aluminogermanate (AlGe) analogs are considerably shorter (< 50 nm) than the aluminosilicate (Al-Si) nanotubes and the diameters are about 50% larger.

1.3 Synthesis and Growth Mechanisms of Aluminosilicate Materials

There are many natural and synthetic aluminosilicates whose existence is made possible by the unique aqueous chemistries of silicon and aluminum. For example, silicates hydrolyze easily at pH > 9 with limited solubility in more acidic solutions [81-83]. Silicon forms tetrahedral coordination complexes with water both in acidic and basic aqueous solutions. Aluminum, on the other hand, prefers tetrahedral coordination at pH >

9 and the octahedral arrangement at pH < 9 [81]. This variability in coordination chemistry, and variation of parameters like pH, temperature and concentration, can lead to a host of materials. For instance, more than 200 types of zeolites [84] (crystalline nanoporous aluminosilicates used widely as molecular sieves and catalysts) have been synthesized. Different zeolites can be synthesized by changing parameters such as temperature or the organic template [84, 85]. In the case of zeolites (sodalite, chabazite etc.) where no organic templates are used for synthesis, it has been proposed that the alkali-metal cations act as templates, forming an ordered shell of water around themselves and which is subsequently displaced by the tetrahedrons of silicon and aluminum under basic conditions [84]. Thus, changing the alkali metal cation can alter the resulting zeolite structure. The pore systems of such materials tend to have spherical/isotropic cages rather than channels of specific shape. In the case of the templated zeolites, the templating (structure-directing) function is carried out by an organic molecule which influences the pore shape and structure of the product material.

Comprehensive kinetic data (easily available for organic polymers) is usually missing in the case of aluminosilicate polymers. Most of the structures synthesized are through empirical experimentation. Concrete mechanistic insights into the formation of aluminosilicates are necessary to develop engineering principles for synthesis of these structures. Even though there exists a large array of aluminosilicates, and though they are a valuable base for a range of nanotechnology applications, much remains unknown about their mechanisms of formation [84, 85].

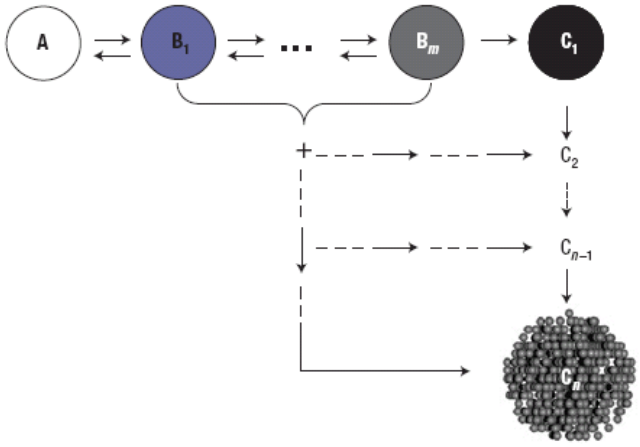

Figure 1-7: Kinetic model of formation of Zeolite. Taken from [86].

Zeolites have attracted a number of mechanistic studies [85-87] due to their variety of complex structures and many applications. The synthesis of defect-free and controllable pore size zeolites (and zeolite films) has remained a significant challenge. Zeolites are made by a hydrothermal synthesis involving sols of precursor material and possibly an organic structure directing agent (depending on the type of zeolite) [84]. There is a consensus in the zeolite community that the sol consists of nanoparticles [85-88]. However, the structure of the nanoparticles, and the mechanism by which they contribute to the growth of zeolite crystals, is still a matter of some controversy [85, 87]. In a recently published work [86], it has been demonstrated by systematic time-dependent (~ 1 year) characterization, that zeolite crystals can evolve by structural transformation and aggregation from amorphous nanoparticles which actively participate in the zeolite nucleation and growth. The kinetic model developed (Figure 1-7) shows that amorphous precursor nanoparticles (*A*) gradually transforms to zeolite nuclei (*C*) through additive intermediates (B_n). The growing crystal is depicted as C_1 to C_n.

The synthesis process of zeolites has similarities to the synthesis of aluminosilicate nanotubes, in the sense that both are hydrothermal processes and involve similar precursors (sols of Al and Si). However the differences are also significant. Aluminosilicate nanotubes are synthesized using dilute precursors in mildly acidic aqueous solutions, whereas zeolites are synthesized in concentrated sols in basic pH. Little work has been done on the mechanism of formation of the aluminosilicate nanotubes from the precursors, and previous authors refer to a speculative mechanism proposed in 1977 [77, 78]. It was proposed that the formation of imogolite occurs through a intermediate called "proto-imogolite" [78]. However, its structure could not be detected by TEM and its existence is proposed based on the structure of the final product. It was suggested [89, 90] that the formation of "proto-imogolite" precursors took place early in the reaction, and these precursors provided nuclei to the growth and formation of nanotubes by polymerization. However, definitive experimental proof of this mechanism has been lacking.

1.4 Overall Objective and Strategy

This thesis is focused on obtaining a quantitative understanding of the mechanism of formation and growth of a class of metal oxide nanotubes, namely the aluminosilicate (and analogous aluminogermanate) nanotubes. Ideally, the mechanistic model should explain how growth occurs, provide a kinetic and thermodynamic rationale for the nanotube growth, and additionally allow insights that might make possible the control of nanotube shape and size as well as the synthesis of potentially new materials using the

same mechanistic principles. The above overall objective has been achieved through a set of specific steps as follows. In *Chapter 2*, a detailed phenomenological study of the growth and structural properties of aluminosilicate and aluminogermanate nanotubes is presented. The evolution of the aqueous-phase nanotube synthesis process over a period of 5 days, was analyzed by a number of qualitative and quantitative characterization tools. In particular, the time-dependence of the nanotube size, structure, and solid-state packing was followed using electron microscopy, electron diffraction, X-ray diffraction, and dynamic light scattering. In *Chapter 3*, the mechanism of formation of single-walled aluminogermanate nanotubes is presented, with the development of key insights into the processes of hydrolysis and self-assembly of the oxide precursors in mildly acidic aqueous solutions. Here we employ solution-phase and solid-state characterization tools to elucidate such a mechanism. Based on observations from this mechanistic study and previous phenomenological study, a quantitative kinetic model was developed. The kinetic parameters of the model were obtained by fitting of experimental data. Chapter 2 and Chapter 3 together, provide a basic thermodynamic and kinetic rationale for understanding and controlling the growth of such materials. In *Chapter 4*, we show the capability of controlling the dimensions (diameter and length) by synthesizing mixed metal oxide (AlSiGe) nanotubes. In *Chapter 5*, we discuss results of preliminary work towards generalizing the kinetic model of formation of the AlGe nanotubes (developed in Chapter 3) to the entire spectrum of AlSiGe nanotubes. *Chapter 6* summarizes the present work and discusses future directions for engineering the nanotube materials, along with relevant preliminary data.

Chapter 2 : Phenomenology of the Growth of Aluminosilicate and Aluminogermanate Nanotubes

2.1 Introduction and Objective

In the present study, we undertake a systematic investigation of the growth of imogolite aluminosilicate [75, 76] and aluminogermanate [80] nanotubes. Our approach is based on the use of a number of complementary characterization techniques to probe the dimensions, structure and morphology of the nanotubes both in solid state as well as aqueous phase, as a function of synthesis time. In particular, samples withdrawn at specific times (up to 120 hours) from the nanotube synthesis reactor are then characterized using transmission electron microscopy (TEM), selected area electron diffraction (SAED), x-ray diffraction (XRD) and dynamic light scattering (DLS). TEM and XRD data were used to extract information on the morphology of the nanotubes and to propose a model for their packing in the solid state. SAED was used to ascertain the internal structure of the nanotubes as a function of growth time. Detailed mathematical analysis of DLS data provided quantitative information on the dimensions of the nanotubes in solution. The combination of characterization techniques revealed new aspects of the process of nanotube formation and structure, which are discussed below. The experimental evidence obtained here is then discussed in the context of the two possible types of nanotube formation mechanisms. The phenomenology of aqueous phase AlSi and AlGe nanotube growth as developed here is a required step towards

understanding the mechanisms of formation of these nanoscale materials, and further using the insights gained to synthesize and apply new classes of functional nanomaterials.

2.2 Possible Mechanistic Pathways to Nanotube Formation

Our investigations into the synthesis and properties of inorganic nanotubes indicate that imogolite Al-Si and AlGe nanotubes have unique properties (e.g., short length, hydrophilicity, ability to disperse in aqueous phase, well defined structure, and monodispersity) which make them attractive candidates for the above applications. Despite the potential nanotechnological applications of imogolite-like nanotubes, the phenomenology and mechanism of its formation are not well understood. Previous investigators have suggested a mechanism based on the formation of sheets/layers of gibbsite which eventually develop curvature due to the binding of silicate groups [90, 91]. The curvature results from the differing bond lengths of the Al-O and Si-O bonds (0.19 nm and 0.16 nm respectively), i.e., the tetravalent silicon atoms pull the oxygen atoms in the aluminum hydroxide layer into a curved cylinder. As mentioned earlier, the formation of imogolite has been proposed to occur from the intermediate "proto-imogolite", which is said to possess some structural characteristics of imogolite but not its distinct nanotubular morphology [78]. Its structure could not be detected by TEM. It was also observed that the quantity of nanotubes seemed to grow substantially with the reaction time, with all the precursors being consumed by about 120 hours of synthesis time [90]. Thus it was suggested [89, 90] that the formation of "proto-imogolite" precursors took place early in the reaction, and these precursors provided nuclei to the

growth and formation of nanotubes by polymerization. However, definitive experimental proof of this mechanism is lacking.

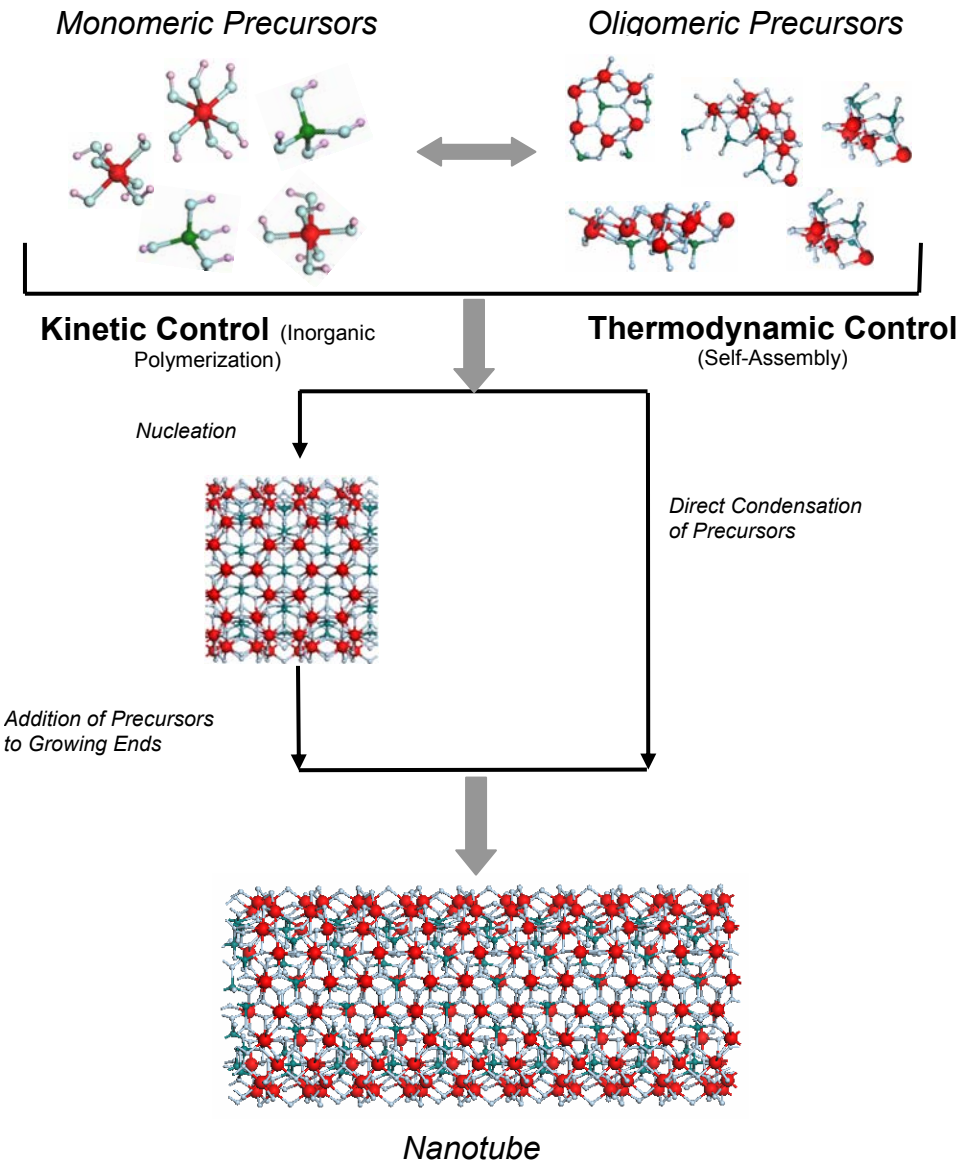

Figure 2-1: Schematic of possible mechanistic pathways leading to the formation of short aluminosilicate and aluminogermanate nanotubes in aqueous phase.

Figure 2-1 shows a schematic of the main events that are likely to occur in two generally possible mechanisms. In a "kinetically driven" growth, the nanotube length

would increase substantially with synthesis time as growth units are added to the end of a previously nucleated nanotube; whereas in a "thermodynamically controlled" self assembly process, nanotubes could self-assemble as dictated by the precursor solution properties and the temperature. Depending on which type of mechanism operates, one would require different approaches towards controlling the nanotube structure.

2.3. Experimental Section

2.3.1. Synthesis

Tetraethylorthosilicate (TEOS) was added drop-wise to a stirred solution of 5 millimolar (mM) $AlCl_3$ solution until the Al:Si ratio was 1.8, and left to stand for 45 mins under vigorous stirring. Then a 0.1 N NaOH solution was added at the rate of 0.3 ml/min until the pH of the solution reached 5.0. The pH was brought down immediately to 4.5 by drop-wise addition of a solution containing 0.1 M HCl and 0.2 M of acetic acid. The resulting clear solution was allowed to stir for 3 hrs and then reacted at 95ºC under reflux conditions. A similar procedure was followed for the aluminogermanate nanotube except that TEOS was substituted by $GeCl_4$.

For DLS analysis, 5 ml of the sample was filtered through a 0.2 μm pore size syringe filter to produce a dust-free sample containing only nanoscale particles. A drop of the sample was deposited on a formvar-backed copper TEM grid for electron microscopy and diffraction analysis. The remaining sample was transferred into a vessel under

vigorous stirring. 0.1 N ammonia solution was added carefully until the pH reached 8.0. At this point the solution turned opaque and was centrifuged at 3000 rpm for 20 min. The supernatant was discarded and the gel acidified with a few drops of 12 N HCl. The resulting solution was immediately dialyzed against deionized water for 120 hrs to remove any unreacted precursors as well as sodium and chlorine ions. A schematic of the synthesis and purification process is shown in .5 ml of dialyzed solution was evaporated over a glass slide to deposit a film of nanotubes amenable to XRD and XPS (X-ray Photoelectron Spectroscopy) analysis. A portion of the dialyzed sample was freeze-dried for nitrogen adsorption measurements.

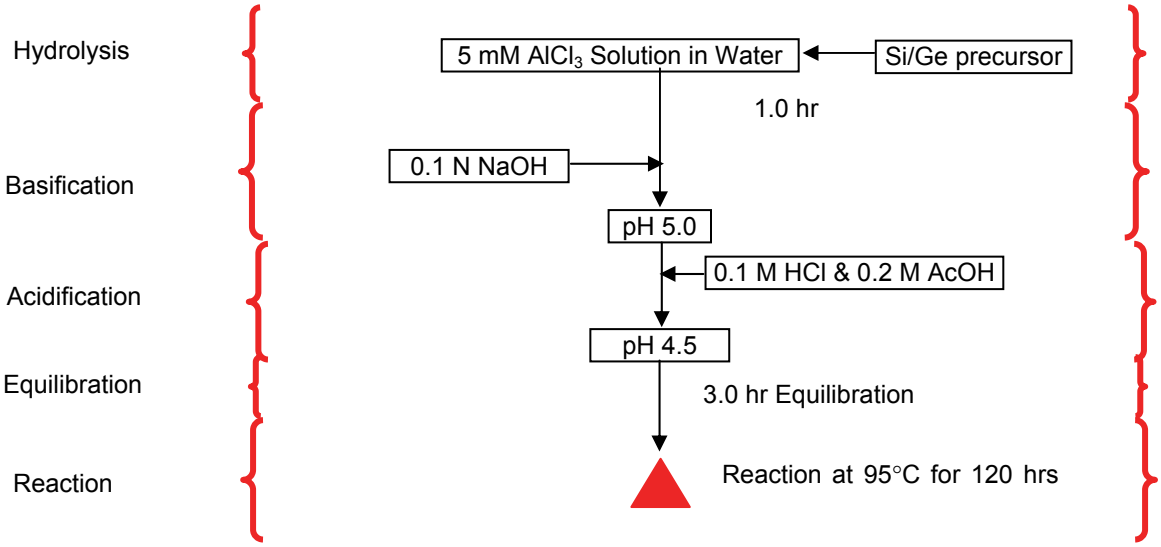

Figure 2-2: Aluminosilicate/Aluminogermante nanotube synthesis process.

2.3.2. Characterization

TEM images and SAED patterns were obtained with a JEOL JEM 100CX transmission electron microscope operated at 100 kV. Due to the low contrast of the nanotubes, imaging was restricted to slight underfocus conditions. Since the converging electron beam tends to destroy the sample, the ED patterns were recorded first. A parallel, rather than convergent, electron beam was used to reduce electron dosage while obtaining the ED patterns. Thin film XRD analysis was performed on a PAnalytical X'pert Pro diffractometer operating with a Cu Kα source and equipped with a diffracted beam collimator and a Miniprop detector. The data were collected in grazing angle incidence mode, with the incident beam at a fixed grazing angle of 1º with respect to the sample plane, and the detector scanning over angles from 2º to 30º with respect to the same plane. The nanotube films were analyzed for surface composition with a PH1 Model SCA 1600 XPS instrument equipped with a monochromatic Al Kα source (1486.4 eV) and a spherical capacitor analyzer operating at 187.85 eV pass energy. High resolution spectra (0.05 eV/step and 50 ms/step) were collected for bond information by peak deconvolution using Gauss-Lorentzian peaks.

Nitrogen adsorption measurements were performed at 77 K using a Micrometrics ASAP 2000M adsorption analyzer. The samples were first outgassed for 12 hrs at 250ºC. A static volumetric method was used to obtain the volume of nitrogen adsorbed as a function of relative pressure in the range of 10^{-3} to 10^{0} was used. This was sufficient to scan the expected range of the nanotube pore size. The pore size distribution was

determined using the Horvath-Kawazoe [92] model (developed for slit shaped pores) with the Saito-Foley [93] modification for cylindrical pores. DLS data were collected with a Protein Solutions DynaPro instrument. The scattering angle was 90º and the laser wavelength was 720 nm. The autocorrelator delay time (τ) was 1 μs. At least 20 scans were performed on each sample, each with a 10 s acquisition time. Initial cumulant analysis [94] was used to discard uncharacteristic or erroneous scans affected by scattering from stray particles (e.g. dust) in the sample.

2.4. Results and Discussion

2.4.1 Structure, Packing and Composition of Nanotubes

2.4.1.1 Transmission Electron Microscopy and Selected Area Electron Diffraction

Figure 2-3 shows the SAED pattern of an Al-Si NT sample after 120 hours of synthesis. Since the Al-Si and AlGe nanotubes are similar in molecular structure, the ED patterns obtained were the same. The Miller-indexed peaks and corresponding *d*-spacings of the five most prominent rings in the ED pattern are tabulated in Table 2-1. The SAED patterns mainly probe the structure within the individual nanotubes, and are important for tracking the formation of the nanotubes. With the crystallographic *c*-axis along the nanotube axis, the (006) and (004) reflections occurring at *d*-spacing of 0.14 nm and 0.21 nm are sharp and intense [74, 76, 79, 80, 95, 96], and arise from the periodic unit cell of approximately 0.85 nm in the *c*-direction.

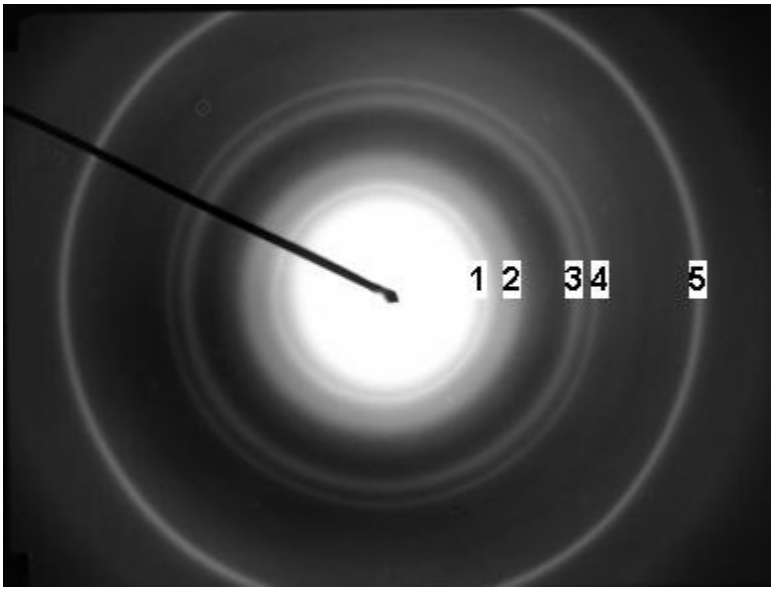

Figure 2-3: Selected Area Electron Diffraction Pattern of Al-Si nanotubes. The numbers on the rings correspond to those in Table 2-1.

Table 2-1: The d-spacings of rings appearing in the SAED pattern of Al-Si NTs (Figure 2-3). The (hkl) indices are in the cylindrical C_{24h} space group.

Reflections	**d-spacing (nm)**	**hkl**
1	0.14	006
2	0.21	004
3	0.22	063
4	0.32	071
5	0.43	002

The diffraction spots due to the packing of the tubes are located very close to the central beam and can only be identified for very low selected areas (< 20 μm) and low exposure times. The nanotube packing is better elucidated using XRD, as discussed later in this paper. Due to the cylindrical (C_{24h}) symmetry of these nanotubes, the odd reflections along the *c* axis are absent. A similarly intense (006) reflection, as well as the (004) reflection, are observed for the AlGe nanotubes. The absence of the (003) or (005)

reflections also supports the assignment of C_{24h} symmetry of the AlGe nanotubes. The (006) and (004) rings are thus taken as characteristic signatures that differentiate the nanotubes from any amorphous materials or other crystalline structures existing in the samples at various times during the reaction.

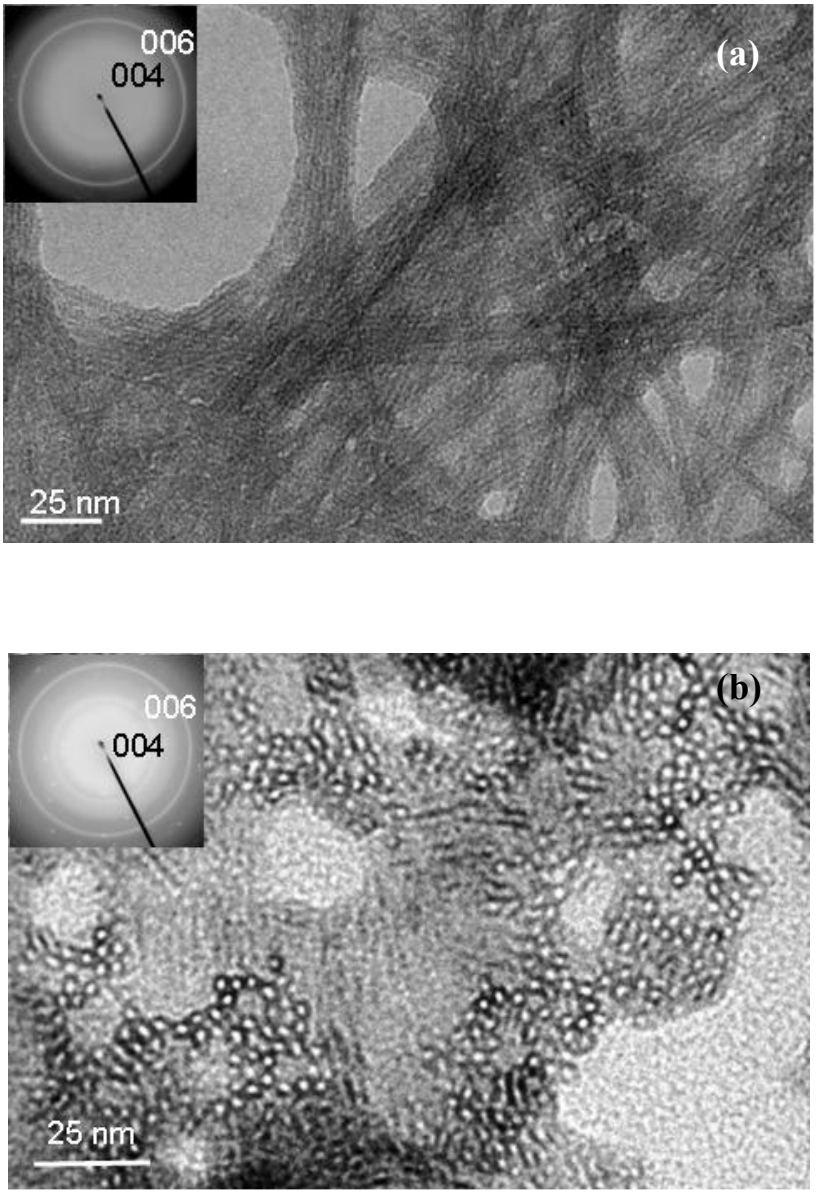

Figure 2-4: Transmission Electron Micrographs of (a) Al-Si and (b) AlGe nanotubes at a synthesis time of 120 hours. Inset are SAED patterns obtained from the same samples.

Figure 2-4 shows TEM micrographs of the Al-Si and AlGe nanotubes at a synthesis time of 120 hours. The morphology of the AlSi samples is that of bundles of close-packed nanotubes, the lengths of the bundles being close to a micron. The bundles form a random fibrous network. On the other hand, the AlGe nanotubes are much shorter, do not form any fibrous structures, and display a morphology consisting of nanotubes often standing upright on the surface of the polymeric TEM sample film. This distinct feature arising from the short length of the AlGe nanotubes enabled us to obtain clear TEM images down the axis of the AlGe nanotubes (Figure 2-4b). The diameters of the AlSi and AlGe nanotubes appear to be highly monodisperse, being measured as 2.2 nm and 3.3 nm (outer diameter) respectively.

2.4.1.2 X-Ray Diffraction

Figure 2-5 shows the characteristic XRD spectra of AlSi and AlGe nanotubes. While a fully quantitative understanding of XRD spectra from nanotube materials has not been achieved to date, these spectra can be used in estimating the external diameter of the nanotubes. The sharp and intense first peak is always strongly correlated to the external diameter. As can be seen in the nanotube TEM images (Figure 2-4), the AlSi nanotubes are long and exhibit substantial packing, which may further contribute to the sharpness of the first peak. AlGe nanotubes on the other hand are short and show less packing order. Thus, the first intense reflection, while still representative of the nanotube diameter, is broader and leads to a less accurate estimate.

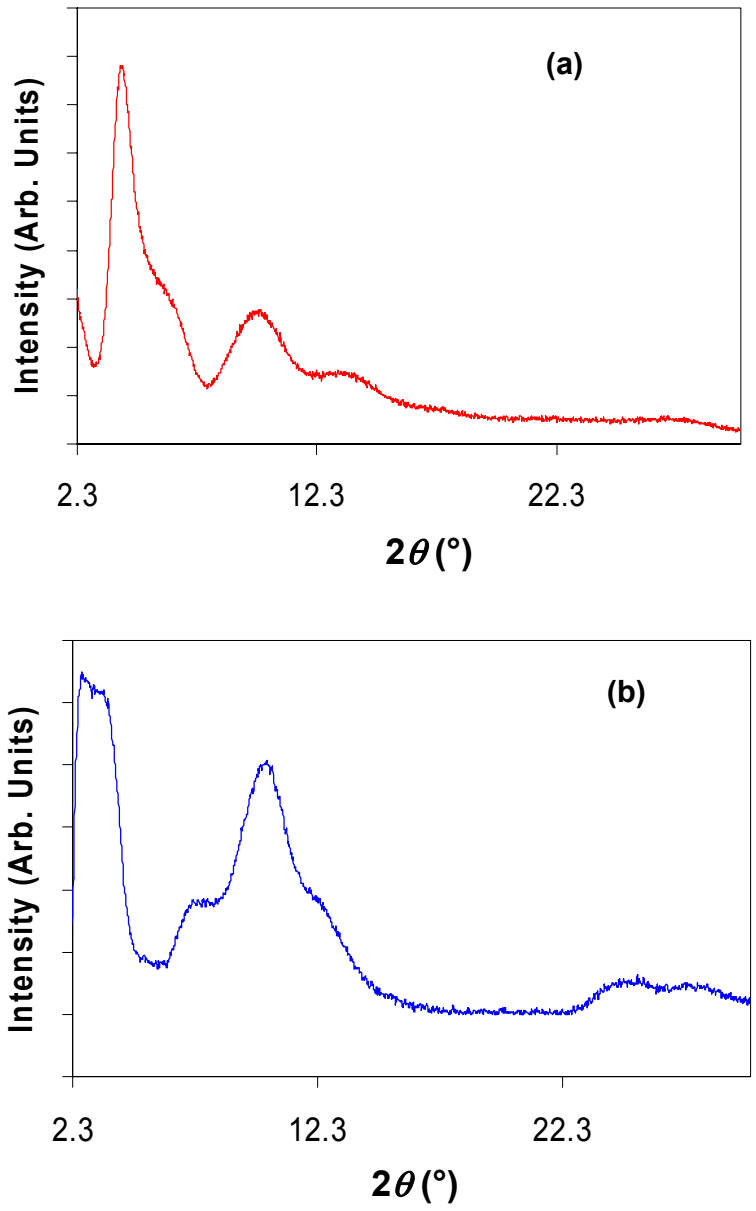

Figure 2-5:Grazing angle incidence XRD spectra from thin films of (a) AlSi and (b) AlGe nanotubes obtained after 120 hours of synthesis.

To calculate the external diameter of the nanotubes from the XRD spectra, the spectra were fitted with Gaussian peaks. The respective spectra along with the Gaussians are shown in Figure 2-6. Then the peak position of the first reflection was used to calculate the estimated diameter of the nanotubes. The diameter of the AlSi nanotube

calculated from this method is quantitatively more accurate than the AlGe counterpart, as explained previously.

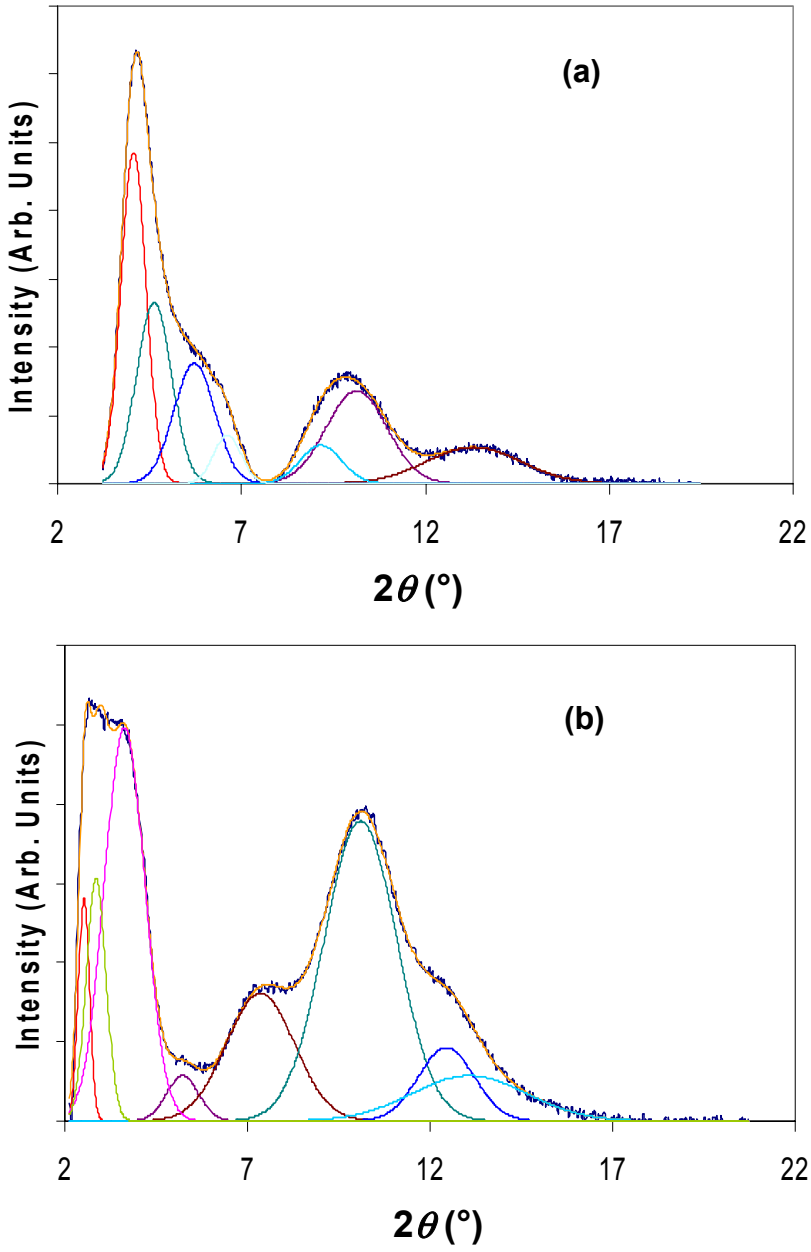

Figure 2-6: Fitted XRD spectra of (a) AlSi and (b) AlGe nanotubes.

2.4.1.3 Nitrogen Adsorption

Figure 2-7a shows the nitrogen adsorption isotherms at 77 K for AlGe and AlSi nanotubes (synthesized by a 120 hr reaction, purified by dialysis, and outgassed at 250ºC for 12 hrs). The lower limit (10^{-3}) of the relative pressure (P/P_{sat}) was determined by the capability of the instrument to equilibrate at low pressures. Figure 2-7b shows the differential pore size distribution of the AlGe and AlSi nanotubes. The pore size distribution was estimated using a modification for cylindrical pores [93, 97] of the HK model [92]. The results agree very well with earlier adsorption studies on natural and synthetic imogolite [98] with the exception that no mesoporosity was observed in our samples. Both AlGe and Al-Se nanotubes show a narrow distribution of pore sizes centered at effective pore diameters of ~ 0.9 nm and ~0.65 nm respectively. The pore size distributions are monomodal which strongly indicates a monodisperse diameter and an open-ended (uncapped) structure of the nanotubes. The diameter of the AlGe nanotubes is substantially larger than that of AlSi nanotubes. These conclusions are in agreement with TEM observations (Section 2.4.1.1). The effective pore diameters measured by nitrogen adsorption are lower than those visible by TEM. As argued by previous authors [92], the exact values of the pore size should be taken with caution, being based on a number of assumptions regarding the pore geometry and the packing of nitrogen in the pores [92, 93, 99].

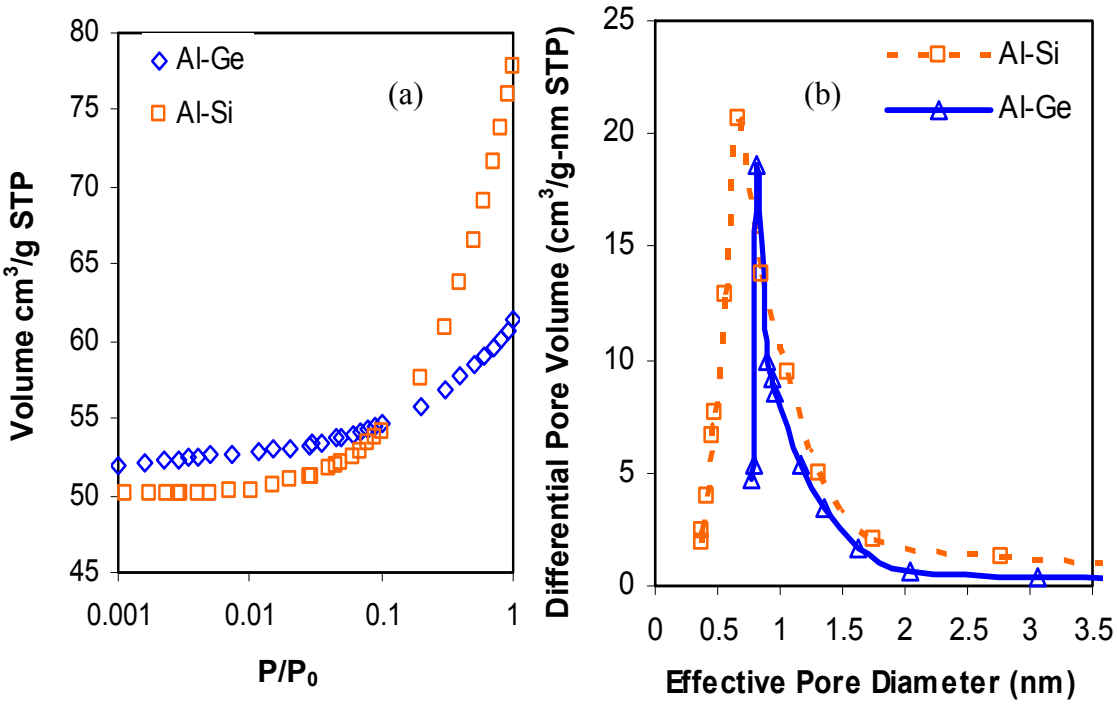

Figure 2-7: (a) Nitrogen adsorption isotherms at 77 K for freeze dried AlSi and AlGe nanotubes outgassed at 250ºC. (b) Differential pore size distributions of AlSi and AlGe nanotubes.

2.4.1.4 X-ray Photoelectron Spectroscopy

XPS survey spectra for the AlSi and the AlGe NT films are shown in Figure 2-8a and Figure 2-8b respectively. The following photoelectron bands were used to calculate the composition of the sample: Al2p (71.8 eV), Al2s (116.79 eV), Ge2p3/2 (1217.2 eV), Ge3d (29.15 eV), Ge2p1 (1220.7 eV), Si2s (150.2 eV) and Si2p (99.4 eV). The atomic concentrations were obtained from fitting of the peaks were 10.99% Al and 6.44% Si for the AlSi NT film, and 16.56% Al and 6.18% Ge for the AlGe NT film. The atomic concentration ratios (Al:X , X = Si or Ge) are thus close to 2, conforming to the expected chemical composition of the nanotubes.

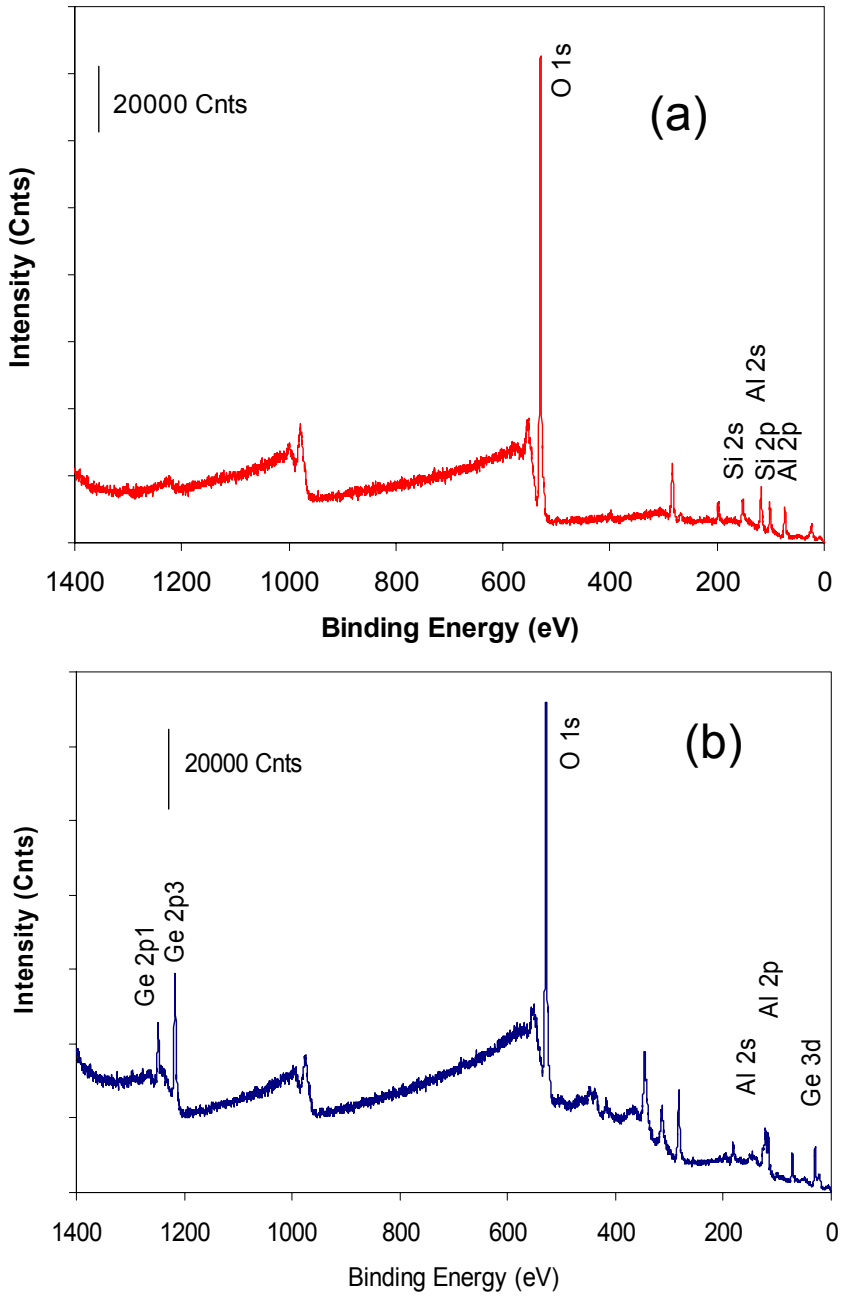

Figure 2-8: X-ray Photoelectron Spectroscopy survey spectra of thin films of (a) AlSi and (b) AlGe nanotubes. The positions of the oxidation states of the elements are indicated.

2.4.2 Morphology Dependence on the Growth Time

2.4.2.1 X-Ray Diffraction

Figure 2-9 shows the XRD patterns of AlSi and AlGe nanotubes extracted from the reactor samples at reaction times of 10, 24, 48, 72 96 and 120 hrs. All the peaks seen in the 120-hr samples are visible even at shorter reaction times (10 hrs). All the peaks increase in intensity as the reaction time is increased, showing that the nanotubes are increasing in quantity. Since the volume of sample dried on the glass slide was the same in all cases, the concentration of the nanotubes must be increasing with reaction time.

2.4.2.2 Transmission Electron Microscopy and Selected Area Electron Diffraction

A series of TEM micrographs (Figure 2-10) shows the samples prepared directly from the AlSi nanotube synthesis reactor at reaction times of 10, 24, 48, 72, 96 and 120 hrs respectively. The SAED patterns are also inset in the Figures. It is clear that nanotubes form as early as 10 hrs. This is inferred from the morphology of the TEM images, and is well supported by the occurrence of the (006) and (004) reflections in all the SAED patterns. Figure 2-11 show the TEM micrographs of AlGe nanotubes at intermediate growth times of 10, 24, 48, 72, 96 and 120 hrs; and the insets show the SAED patterns. All the micrographs clearly show the presence of nanotubes from as early as 10 hrs, and the reduction of amorphous materials with the increase in synthesis time. In the AlGe NT case however, the nanotubes are relatively short (~10 nm) as indicated

before. Qualitative comparison of the images does not indicate any appreciable changes in the nanotube length and diameter, or observable high polydispersity in either the length or the diameter.

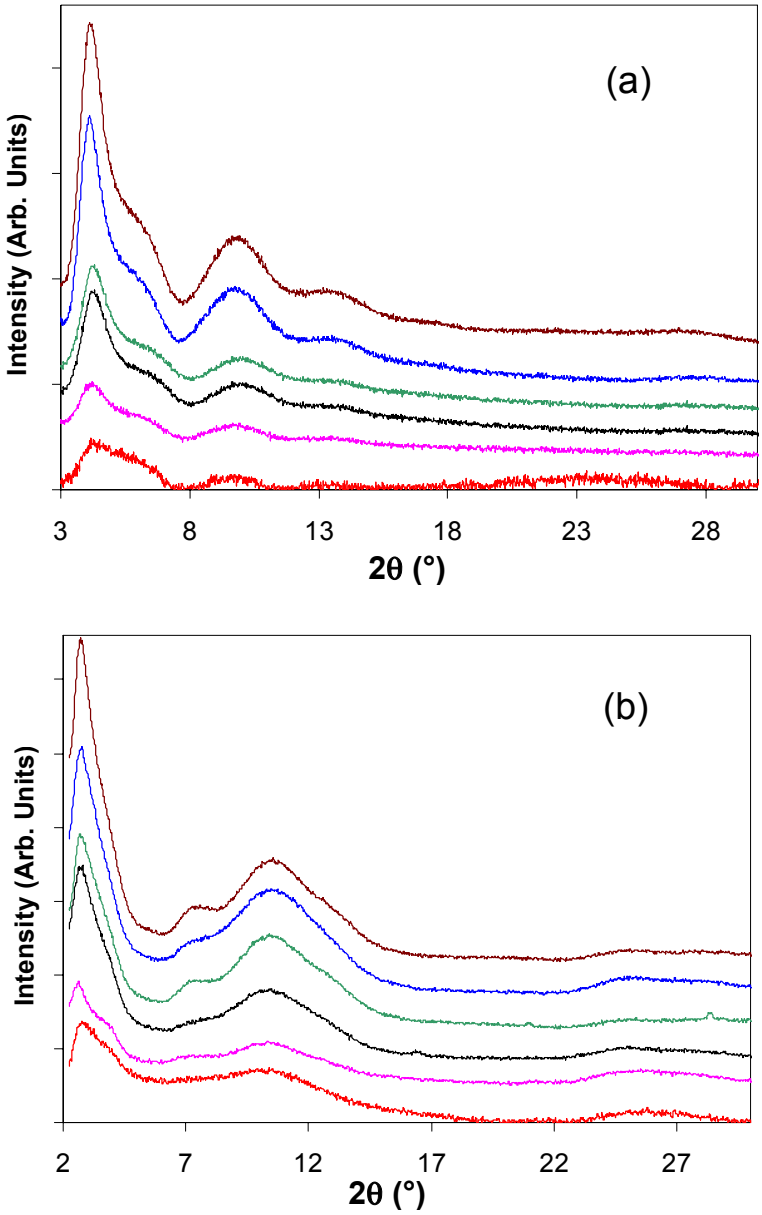

Figure 2-9: X-ray diffraction spectra of (a) AlSi and (b) AlGe nanotubes at synthesis time of 10 hrs, 24 hrs, 48 hrs, 72 hrs, 96 hrs and 120 hrs respectively, arranged from bottom to top with increasing synthesis time.

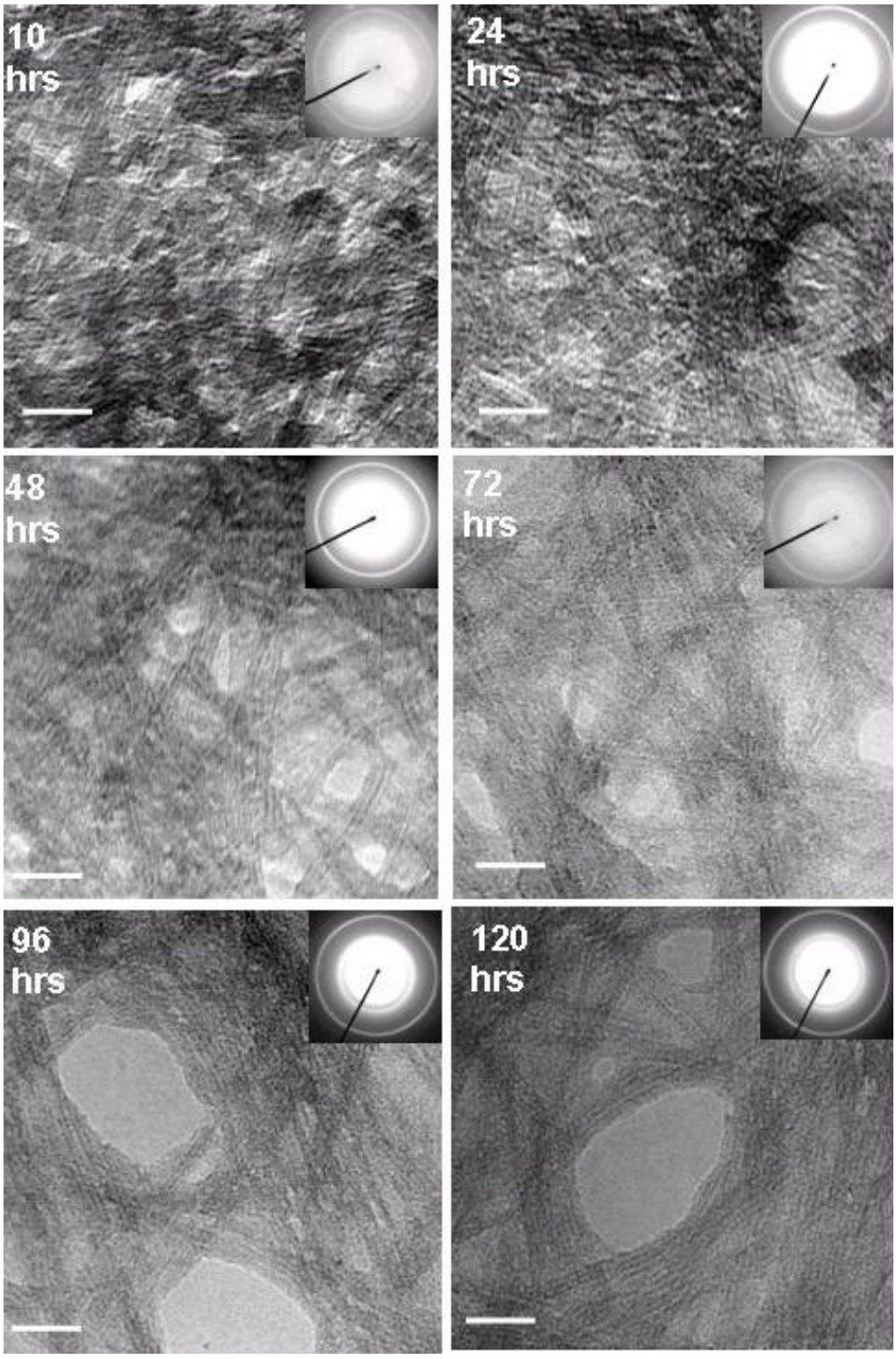

Figure 2-10: TEM micrographs with SAED insets of AlSi nanotubes as a function of synthesis time as indicated in the figures. The scale bar is 25 nm.

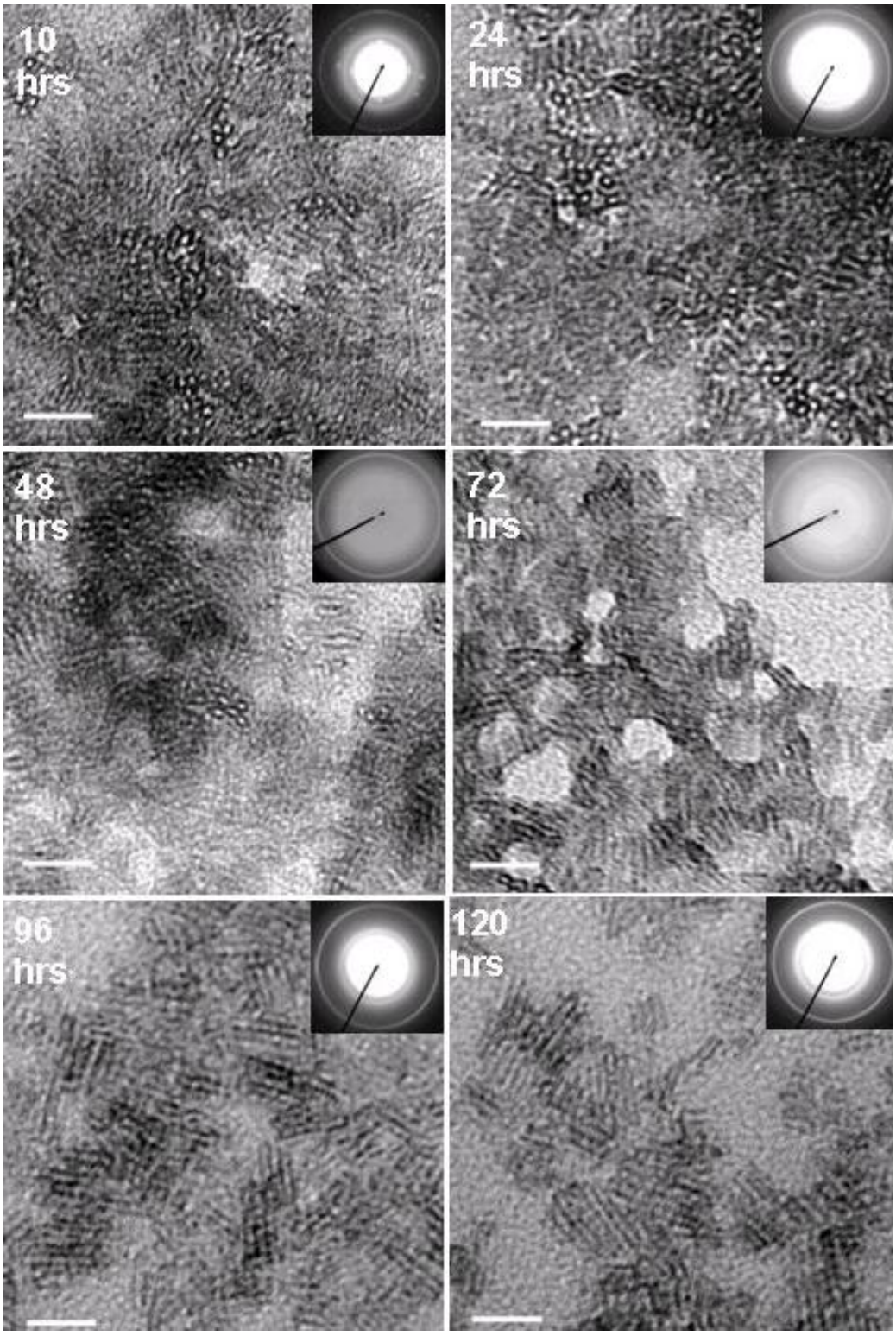

Figure 2-11: TEM micrographs and SAED insets of AlGe nanotubes as a function of synthesis time as indicated in the figures. The scale bar is 25 nm.

2.4.3 Quantitative Analysis of Nanotube Growth by Dynamic Light Scattering

2.4.3.1 Dynamic model

DLS is a useful technique for studying the dimensions of nanoparticles in solution at dilute concentrations. The present synthesis produces micromolar concentrations of nanotubes in solution. This situation is ideal for DLS measurements, but unfavorable for techniques such as small-angle X-ray scattering (SAXS) which require higher concentrations of nanoparticles to obtain quantitatively useful data. The characteristics of self-diffusion of rigid and flexible rod-like nanoparticles in dilute isotropic solutions have been the subject of extensive theoretical treatment[100-104] and have been used to fit DLS data and to determine the dimensions and polydispersity of rod-like nanoparticles such as viruses[105] and inorganic whiskers [106]. In this section we discuss briefly the theoretical details applicable to the system under investigation, and then present the results of our DLS investigations into AlSi and AlGe nanotube synthesis.

For a rigid rod nanoparticle undergoing Brownian translational and rotational motion in a solvent, the translational and rotational diffusivity coefficients D and Θ respectively are related as [104]:

$$\frac{L^2\Theta}{D} \sim 9 \qquad (2.1)$$

In particular, Θ has an L^{-3} dependence, where L is the length of the rod. When the rod length is short, the rotational diffusion becomes very rapid. If the time taken to rotationally circumscribe a sphere approaches the delay time ($\tau \sim 1\ \mu s$) of the

autocorrelator, then the rapidly rotating rod can be approximated as a translationally diffusing sphere whose diameter equals the length of the rod. In our experiments the measured diffusion coefficients for the AlGe nanotubes were of the order of 5×10^{-7} cm^2/s, and the nanotube length as obtained from TEM micrographs was ~10 nm. Then $\Theta = 4.5 \times 10^6$ rad^2/s. The time taken to circumscribe a sphere is given as:

$$\frac{2\pi^2}{\Theta} = 4.4 \quad \mu s \tag{2.2}$$

This is close to the delay time of the autocorrelator. Thus, to the autocorrelator the rapidly rotating short rod is indistinguishable from a spherical nanoparticle whose diameter equals the length of the rod. Therefore, in the case of the short AlGe nanotubes, the length can be obtained in a simple manner from the diffusivity D via the Stokes-Einstein equation:

$$\frac{3\pi\eta_0 L}{kT} = D \tag{2.3}$$

With an increase in the length of the rods (AlSi nanotubes) the rotational motion becomes more sluggish and a full model for diffusion (described below) can be used for data analysis.

The Siegert equation [101] relates the normalized intensity autocorrelation function $g_2(t)$ with the field autocorrelation function $g_1(t)$ as:

$$g_2(t) = 1 + \beta |g_1(t)|^2 \tag{2.4}$$

Here β, the coherence factor [101], is an adjustable parameter (taken as unity in dilute aqueous suspensions). The full model for the field autocorrelation function of a suspension of nanorods of uniform diameter but polydisperse length is [100, 107, 108]:

$$g_1(t)=\int_0^\infty \left[a_0 \exp(-Q^2 Dt + Q^4 D^2 t/120\Theta) + a_2 \exp(-Q^2 Dt - 6\Theta t - Q^2 Dt/7)\right] P(L)\,dL \qquad (2.5)$$

Here Q is the momentum transfer given by $Q = (4\pi n/\lambda)\sin(\theta/2)$, where n is the refractive index of water, λ is the wavelength of the incident light, and θ is the scattering angle (90° in the present study). The function $P(L)$ is the distribution function of the rod lengths. The prefactors a_0 and a_2 are given as:

$$a_0 = 1 - Q^2L^2/36 + 13Q^4L^4/32400 + Q^4L^2D/1080\Theta - Q^4D^2/720\Theta^2 \qquad (2.6)$$

$$a_2 = Q^4L^4/6480 - Q^4L^2D/1080\Theta + Q^4D^2/720\Theta^2 \qquad (2.7)$$

This model can be used to obtain the nanotube length from DLS data, employing the expression for the translational diffusivity D of a slightly bending nanorod [100, 107, 108]:

$$\frac{3\pi\eta_0 LD}{kT} = ln\left(\frac{L}{d}\right) + 0.3863 + 0.67(\chi L) + 0.01883(\chi L)^2 + O(\chi L)^3 \qquad (2.8)$$

Here η_0 is the viscosity of the aqueous solvent (0.89 cP at 25°C), χ is the inverse Kuhn length [109] which parameterizes the bending of the rods and which converges to zero for a perfectly rigid rod, L is the length of the rod and d is the outer diameter. The observed signal intensity was in the region of 10,000-250,000 counts per second in all cases. The autocorrelator produces $g_2(t)$ with a high signal-to-noise ratio by means of repeated scans

on the sample (see Experimental Section). Then $g_1(t)$ was obtained from $g_2(t)$ according to the Siegert relation, and the diffusion model (Equations 1-3) was directly fitted to $g_1(t)$ via a nonlinear least squares algorithm developed in-house. Initially, a monodisperse suspension was assumed. The only fit parameters are the nanotube length (L) and the inverse Kuhn length (χ). The diameter of the AlSi nanotubes was taken as d = 2.2 nm based on the TEM images. The values of the nanotube length were used in a subsequent fit incorporating a length distribution function $P(L)$ of Gaussian form, i.e.

$$P(L) = \left(1/\sqrt{2\pi}\sigma_L\right).exp\left[-(L-\bar{L})^2/2\sigma_L^2\right] \tag{2.9}$$

2.4.3.2 Results

Examples of the nonlinear least squares fits of the measured $g_2(t)$ data are shown in Figure 2-12. The open circles are the experimental autocorrelation functions of samples taken at different synthesis times, and the solid lines correspond to the calculated autocorrelation functions using the final values of the fitted parameters. The fits are of excellent quality and the residuals are less than 1%. For the case of the AlSi nanotubes where the inverse Kuhn length (χ) was included as a fitting parameter, it was found that this parameter always converged to zero, i.e., the nanotubes behave as rigid rods in solution. This coincides with a result from previous work which used natural imogolite fibers dispersed in water [107], wherein no bending effects of the AlSi nanotubes were observed. In the case of the AlGe nanotubes, no bending effects are expected at all, owing to their extremely short lengths. Finally, the inclusion of the Gaussian distribution of lengths (to describe polydispersity) resulted in no appreciable standard deviation in the

nanotube lengths. The fitted standard deviations are in the range of 0-1 nm, which are not statistically significant. Hence, the nanotubes are regarded as monodisperse in length, to the limits of dynamic light scattering measurement from nanoparticles[110].

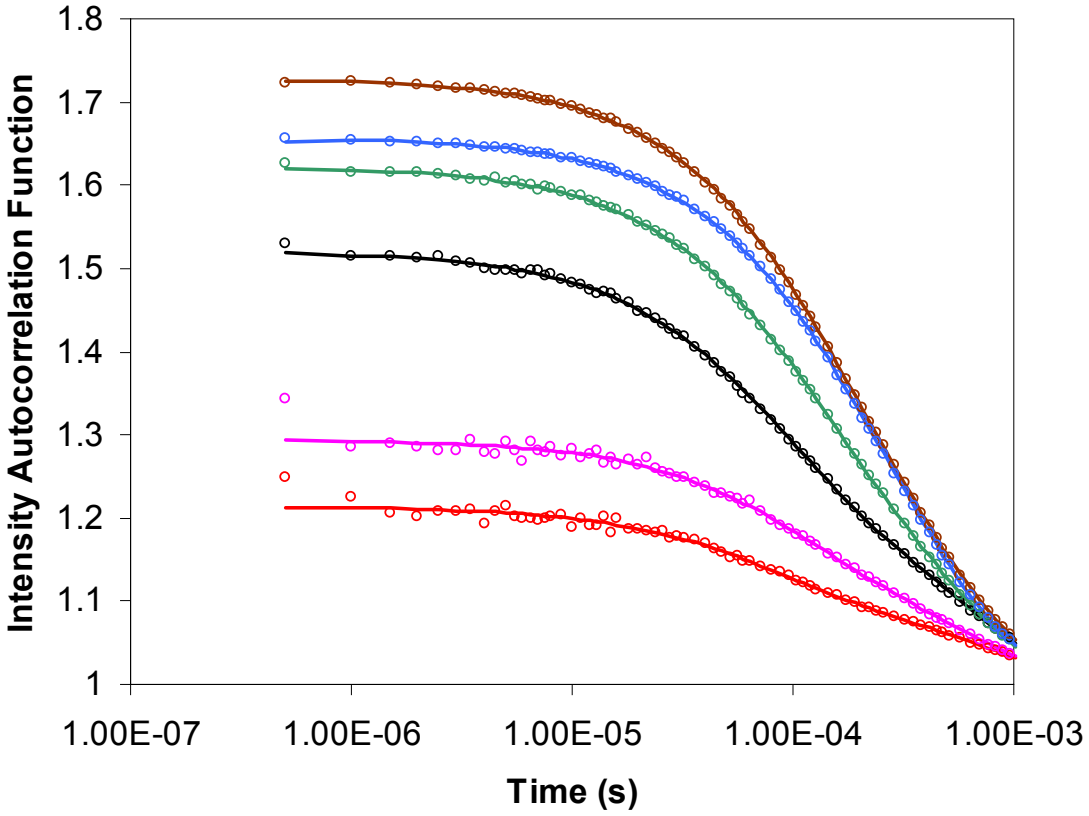

Figure 2-12: Photon intensity autocorrelation functions obtained from DLS measurements on AlSi nanotube solutions at synthesis times of 10 hrs, 24 hrs, 48 hrs, 72 hrs, 96 hrs and 120 hrs, arranged from bottom to top.

The fitted lengths of the nanotubes as functions of synthesis time are shown in Figure 2-13, for both AlSi and AlGe nanotubes. The error bars on the fitted lengths are obtained by averaging the results from 4 independent samples taken in different experiments. An important result of this analysis is that the nanotubes do not grow in

length substantially as a function of synthesis time. Considering the error bars on the data, there does not appear a physically significant "growth rate" for the nanotube lengths. Small increases, if any, in the fitted lengths could also be due to some aggregation of the nanotubes at higher concentrations. The AlSi NTs average about 100 nm in length, whereas the AlGe nanotubes are about 15 nm in length. These results are well consistent with the detailed TEM observations.

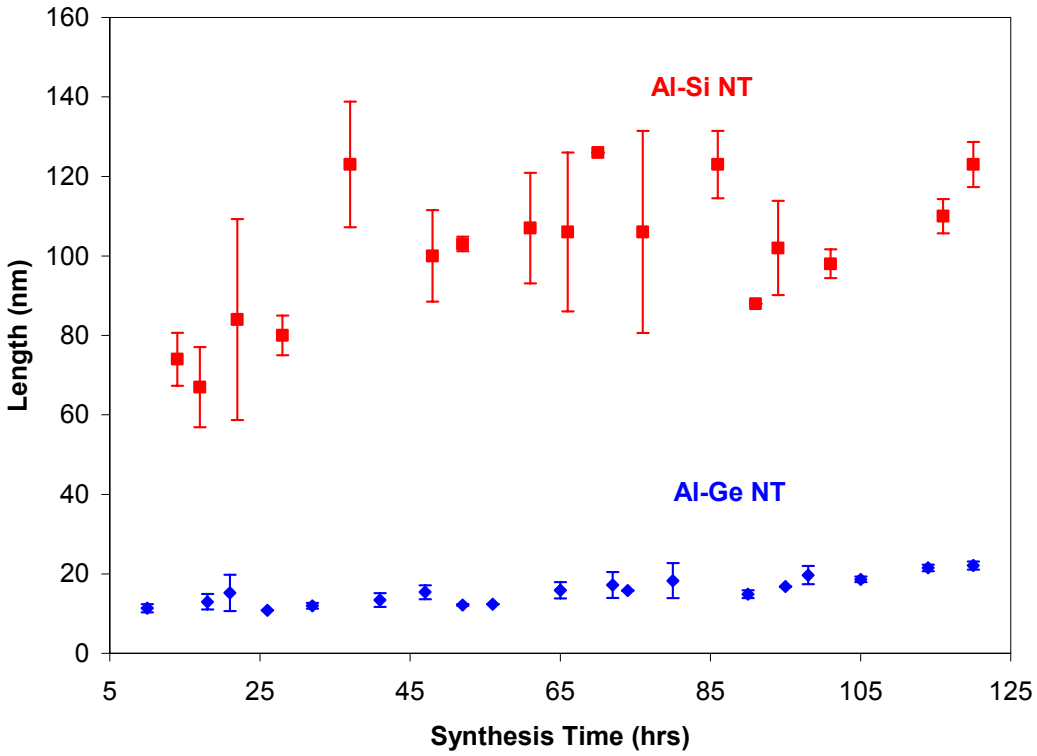

Figure 2-13: Fitted lengths of AlSi and AlGe nanotubes obtained from DLS experiments, as a function of synthesis time from 10 hours to 120 hours.

The practically constant length of the nanotubes throughout the synthesis time (of over 100 hrs) appears to favor a self-assembly mechanism, over a kinetic mechanism involving the formation of 'proto-nanotube' intermediates which increase in length by

addition of precursors. The samples, after filtration through a 0.2 μm filter, do not reveal any other significant population of nanoparticles except for the nanotubes themselves. This indicates that the nutrient sources for nanotube formation are either sub-nanometer aluminosilicate oligomers which cannot be detected by DLS, or a few large gel-like particles suspended in solution and which are removed by filtration. The former possibility is also consistent with NMR spectroscopic studies of acidic gibbsite-forming aluminum (III) hydroxide solutions, wherein no oligomeric precursors other than the monomer and the dimer have been conclusively established [111]. It should be noted that acidic aluminosilicate solutions, with aluminum in primarily octahedral coordination [91, 111], are completely different at a molecular level from the large variety of precursors seen in alkaline solutions [112]. In addition, the highly dilute solutions used here may favor only the formation of a small number of oligomeric precursors. While none of the techniques can provide conclusive evidence regarding the polydispersity of the nanotube length; the DLS fit results, presence of a well-ordered solid state structure, as well as qualitative observation of the TEM images do not support a high polydispersity in nanotube length.

In the light of the present phenomenological work, it is suggested that the nanotubes are the product of a "thermodynamically-controlled" molecular self-assembly process. In other words, the formation of a small (10-100 nm in length) nanotubular molecule of monodisperse diameter, is the final step of the reaction rather than a intermediate step for the growth of longer nanotubes. In this case, control over the nanotube dimensions is unlikely to be obtained by increasing the synthesis time or adding

reactants continuously to the synthesis reactor in the hope of extending the nanotube length, but rather by thermodynamic control over the reaction chemistry. For example, the substitution of silicon with germanium leads to a substantial, yet precise and reproducible, change in the nanotube diameter and length. Other possible methods of thermodynamic control include the use of organosilane precursors (which contain a Si-C bond). These could potentially lead to the formation of well-defined nanotubes with organic-functionalized interiors. From the viewpoint of technological applications, the prevalence of thermodynamic control has advantages in terms of the ability to obtain nanotubes whose dimensions are governed more precisely by the thermodynamics of the self assembly process.

2.5 Conclusion

The phenomenology of formation of single walled aluminosilicate and aluminogermanate nanotubes has been examined by a combination of characterization techniques (TEM ,SAED, XRD, XPS, N_2 Adsorption, and DLS) to probe the nanotube structure, composition, packing, and dimensions as a function of synthesis time. By TEM and DLS analysis, it is found that the dimensions of the aluminogermanate nanotubes are 3.3 nm in diameter and approximately 15 nm in length, whereas those of the aluminosilicate nanotubes are 2.2 nm and approximately 100 nm respectively. The Al/Si and Al/Ge atomic ratios are found to be 1.71 and 2.68 respectively by XPS analysis, consistent with the accepted structural model of these nanotubes. Nitrogen adsorption clearly shows the monodisperse diameter of the nanotubes. The combined TEM, SAED,

and XRD data shows clearly that nanotube materials are formed at an early stage in the reaction, and that the structure of the nanotubes remains essentially identical throughout the synthesis. However, the nanotube concentration increases with synthesis time. XRD analysis shows that their solid-state packing is well ordered in an apparently monoclinic, and not hexagonal, arrangement. Furthermore, the synthetic nanotubes are individually dispersed in an acidic aqueous solution, allowing quantitative analysis of their dimensions by DLS. The present evidence strongly indicates that their dimensions (both length and diameter) do not change significantly with synthesis time. The sum total of the experimental data lends substance to our proposal that self-assembly thermodynamics of the aluminosilicate precursor solution, rather than kinetic kinetic (inorganic nucleation and end-growth) processes, exert control over the nanotube formation. In addition, the confirmation of well defined, uncapped, hydrophilic, dispersible, synthetic nanotube materials is of significance for a number of potential nanotechnological applications.

Chapter 3 : Mechanism of Formation of Aluminogermanate Nanotubes

3.1 Introduction

In the phenomenological study of Chapter 2 [38], we observed that the aluminogermanate nanotube size did not appear to change appreciably during several days of synthesis time, whereas the concentration of nanotubes appeared to increase substantially (as evinced by XRD). This indicated a fundamental and important difference between the present system and the conventional routes [35, 46, 113] for nanotube growth. In the latter cases, growth occurs by catalytic addition of molecular or atomic precursors to the ends of the nanotube to produce long (~ 1 μm) carbon/BN/WS_2 nanotubes, or it may occur by a combination of crystal nucleation, growth and organic templating effects (during liquid-phase growth) to produce long, multi-walled oxide nanotubes. In the above works, the use of organic-templating strategies have not yielded single-walled nanotubes, e.g., templated metal oxide nanotubes are multi-walled and are several tens of nm in outer diameter.

In this Chapter, we describe an investigation that establishes the main aspects of a novel nanotube formation mechanism. We chose the aluminogermanate nanotubes for this work, since they are truly nanoscale objects with length not more than 20 nm. Since the aluminogermanate nanotube synthesis proceeds over a time scale of days to weeks, we were able to employ a number of solution-phase (dynamic light scattering and UV-Vis absorbance spectroscopy) and solid-state (vibrational spectroscopy and electron

diffraction) characterization tools. After careful interpretation of all available evidence, we are in a position to elucidate a mechanism for the self-assembly of short, highly ordered nanotube materials. The mechanism suggests a route to nanotube materials of small (sub-100-nm) and controllable dimensions. This route consists of controlling chemical bonding between precursors in solution *via* pH control, followed by the use of temperature control to form nanoparticle condensates, which sets the stage for self-assembly processes that work to assemble small, ordered objects from the amorphous condensate.

3.2 Experimental Section

3.2.1 Nanotube Synthesis

3.2.1.1 Batch Synthesis

Tetraethylorthogermanate (TEOG) was added drop-wise to a stirred solution of 2.5 millimolar (mM) aluminum chloride ($AlCl_3$) solution until the Al:Ge ratio was 1.8, and left to stand for 45 minutes under vigorous stirring. Then a 0.1 M NaOH solution was added at the rate of 0.3 mL/minute until the pH of the solution reached 5.0. The pH was brought down immediately to 4.5 by drop-wise addition of a solution containing 0.1 M HCl and 0.2 M acetic acid. The resulting clear solution was allowed to stir for 3 hours and then reacted under reflux conditions at different temperatures, as described in the following sections.

3.2.1.2 Semi-Batch Synthesis

A semi-batch synthesis process was designed to supply a steady supply of precursors during the reaction (Figure 3-1). A 150 ml synthesis batch process was set up (Section 3.2.1.1). A precursor batch was prepared using the same procedure, except that the final step was omitted. The precursor solution was slowly added to the synthesis reactor from the beginning of the reaction step. The rate of addition of precursors was 1.8 ml/h. A low rate of addition was preferable to prevent any "shock" (sudden pH change, concentration change etc), which might hinder the reaction. Samples were withdrawn at regular intervals to ensure that the reactor volume remains constant at 200 ml. The samples withdrawn were used for characterization. To prevent any precursor degradation, a fresh batch of precursor solution was prepared and added to the reaction every 24 h.

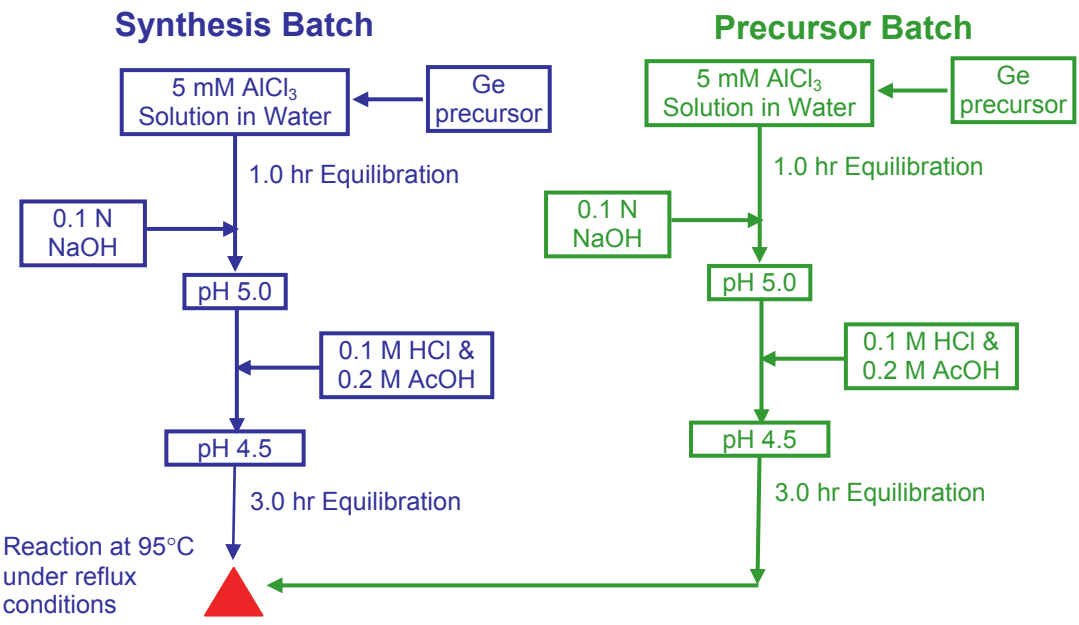

Figure 3-1: Semi-batch synthesis process.

3.2.1.3 Seeded-Batch Synthesis

A seeded batch synthesis was designed in order to supply enough precursors to the "seeds" (purified AlGe nanotubes obtained after 120 h of batch synthesis), so as to increase the length 3 times. The seeds were obtained after synthesis and purification of AlGe nanotubes (Section 2.3.1) and were added to the synthesis batch after the 3 h equilibration step. Assuming the AlGe nanotube length L = 18 nm and a 100 % conversion of the batch synthesis. The empirical formula of AlGe nanotube is $Al_2GeO_7H_4$ [74, 76], with an empirical formula weight of 243 gm/mol. One unit cell of AlGe nanotube is L_o = 0.84 nm long and has N_o = 72 Al atoms in it [38, 114]. In a batch synthesis, 0.181 gm of $AlCl_3.6H_2O$ (Mol. Wt. = 241.5 gm/mol) is added, or N_{Al} = 0.00075 mol of Al is added and V = 15 ml of purified nanotube solution is obtained. Assuming 100% conversion to nanotubes, concentration of nanotubes:

$$C_N = \frac{N_{Al}}{N_O \times \frac{L}{L_O} \times V} \tag{3.1}$$

Substituting, we obtain $C_N = 1.6 \times 10^{-8}$ mol/ml.

The quantity of AlGe nanotube "seeds" added to the batch synthesis is $N_S = C_N \times V = 2.4 \times 10^{-7}$ mol. Now, to increase the length of the seeds to $3L$ = 54 nm, enough precursors must be introduced for an extra $2L$ = 36 nm of AlGe nanotube. Reordering Equation 3.1, the amount of Al required for such growth is:

$$N_{Al} = (C_N \times V) \times N_O \times \frac{2L}{L_O} = N_S \times N_O \times \frac{2L}{L_O} \tag{3.2}$$

Substituting, N_{Al} = 0.00042 mol, which is much smaller than the amount of Al added to the batch reaction i.e. 0.00075 mol. Thus, enough precursors are introduced in the seeded batch synthesis that the seeds could grow to an average length 3*L* if the mechanism is dominated by end-growth.

3.2.2 Characterization Methods

For DLS and UV-Vis analyses, 5 mL samples were withdrawn from the reactor and filtered through a 0.2 μm pore size syringe filter to produce a dust-free sample containing only nanoparticles. DLS data were collected with a Wyatt DAWN EOS instrument. The scattering angle was 108º and the wavelength of the laser was 690 nm. The autocorrelator delay time (τ) was 1 μs. A series of 120 scans were performed on the sample, each with a 1-second acquisition time. UV-Vis data was obtained on a HP 8453 UV-Vis spectrophotometer. A quartz cuvette was used as a sample holder since it is optically transparent to UV radiation. FT-Raman and FT-IR were performed on freeze-dried samples. 100 ml of liquid samples were taken directly from the reactor and immediately frozen at -20°C before application of vacuum. FT-Raman spectra were obtained on a Bruker IFS-66/FRA-106 instrument operating with a Nd:YAG laser. FT-IR spectra were collected under vacuum conditions on a Bruker IFS 66v/S spectrometer. At least 2048 scans were collected for each FT-Raman and FT-IR spectrum, with a resolution of 8 cm^{-1}. Other qualitative characterizations (TEM and electron diffraction) were carried out with a JEOL 100CX TEM operating at 100 kV. X-ray diffraction was carried out by a PANalytical X'Pert Pro instrument with a CuKα wavelength (0.154 nm).

3.3 Results and Discussion

3.3.1 Control of Chemical Bonding in the Precursor Solution

The established synthesis process [38, 80] can be divided into five steps, all carried out under vigorous stirring: (I) *Hydrolysis*, i.e. dissolution of aluminum and germanium precursors in water at pH ~3.5, (II) *Basification*, i.e. slow ramping of the pH to 5.0 by addition of sodium hydroxide, (III) *Partial Re-acidification* to pH 4.5 by addition of acid, (IV) *Equilibration* at room temperature, and (V) *Heating* above room temperature under reflux conditions. Steps I, IV, and V are common in the synthesis of inorganic oxide materials. However, Steps II and III are unusual and have no explanation in the literature, though they were empirically found to be necessary for the formation of nanotubes rather than dense crystalline or amorphous materials [95, 98]. Indeed, we also found that successful nanotube synthesis - while completely reproducible - was critically dependent on the correct execution of the sequence of Steps I-V. It was first verified by TEM imaging of the products (Figure 3-2) that carrying out the synthesis with omission of Steps II and III results in the formation of dense crystalline boehmite (aluminum oxyhydroxide, AlOOH) irrespective of the presence of germanium. This evidence indicated that Steps II and III facilitate a controlled chemical interaction between aluminum and germanium precursors that enables the formation of aluminogermanate nanotubes in Step V.

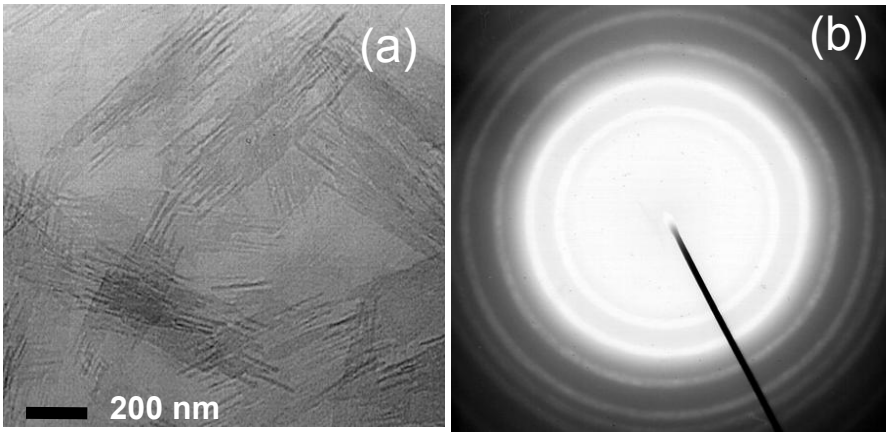

Figure 3-2: (a) TEM image of boehmite (AlOOH) "rafts" formed in the synthesis when Steps II and III were omitted. (b) Electron diffraction pattern of the boehmite "rafts".

To study the events occurring during Steps I-IV in more detail, we first used dynamic light scattering (DLS) to probe nanoparticle evolution during these steps. DLS was found to be preferable over small angle X-ray scattering, since the latter gives a very weak signal at the nanoparticle concentrations of interest (1-10 μM). Figure 3-3 shows DLS autocorrelation functions of liquid samples from the reactor at various stages. These experiments have been reproduced several times to ensure their validity. Complete dissolution of precursors (i.e., lack of nanoparticles) in Step I is evinced by the flat autocorrelation function. Upon increasing the pH (Step II), no nanoparticles are detected until the pH reaches 5, whereupon a well-defined autocorrelation function appears corresponding to nanoparticle condensates 20 nm in size (Figure 3-4). However, these nanoparticles quickly disappear upon partial re-acidification (Step III) and do not reappear during equilibration (Step IV).

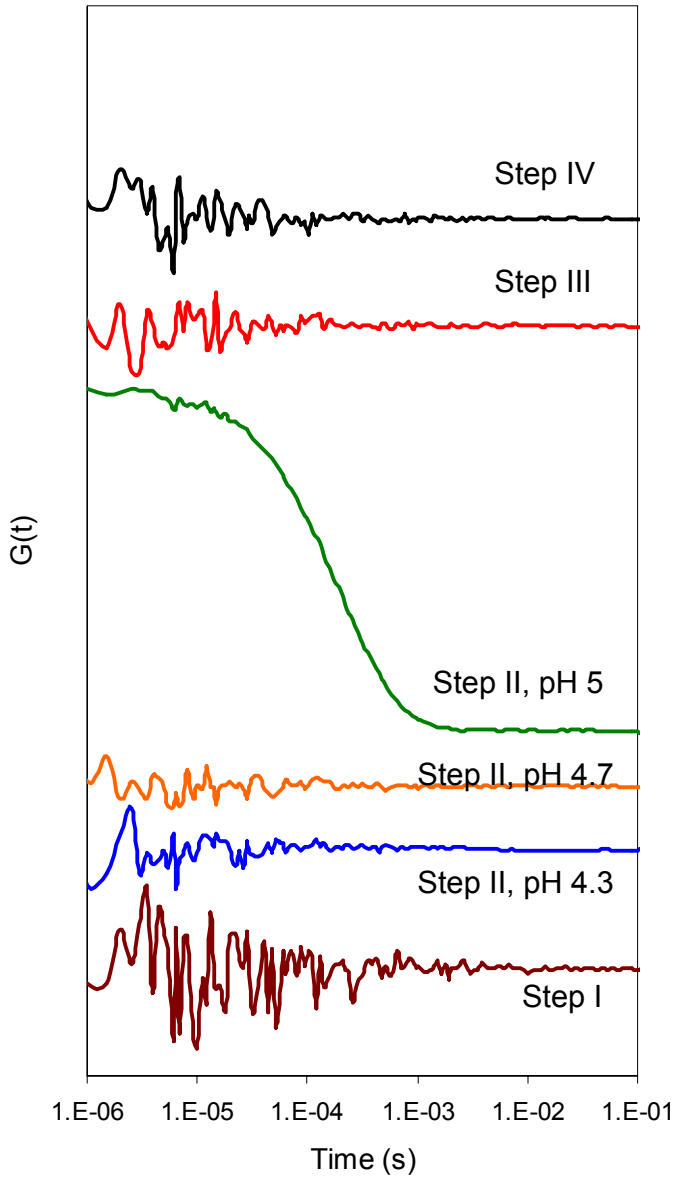

Figure 3-3: Autocorrelation functions G(t) obtained from dynamic light scattering during Steps I-IV of nanotube synthesis.

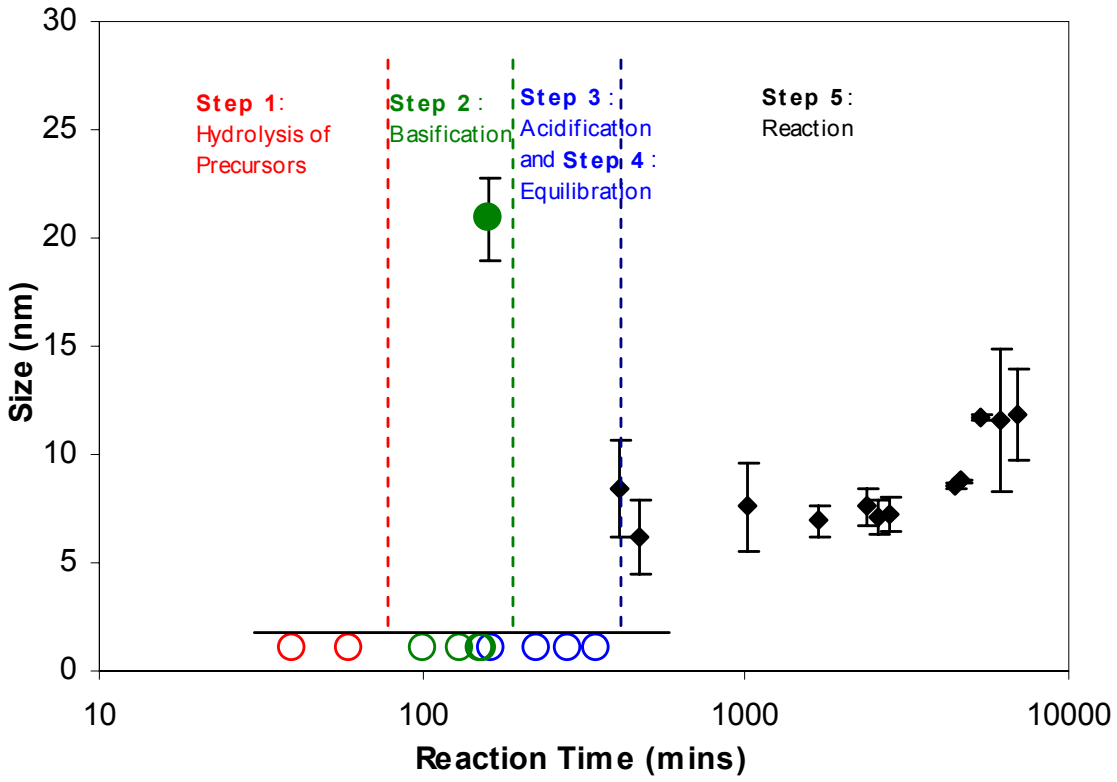

Figure 3-4: Average particle size from DLS analysis for Step 1-5 of the aluminogermanate synthesis.

We then investigated Steps I-IV in greater detail with Raman and infrared (IR) spectroscopy (Figure 3-5). As expected, liquid-phase spectroscopy failed to produce sufficient Raman scattering or IR absorption signal at the concentrations of interest. Thus, solid-state spectroscopy was performed on freeze-dried samples removed from the reactor during these four steps. The Raman and IR spectra corroborate the following main points, based on analysis of the 450-1000 cm^{-1} region that is of importance [80] in identifying the aluminogermanate nanotube material. Firstly, the main change in the bonding environment of the precursors is between Steps I and II (i.e., upon basification), whereas there are only minor changes in the vibrational spectra thereafter (through Steps

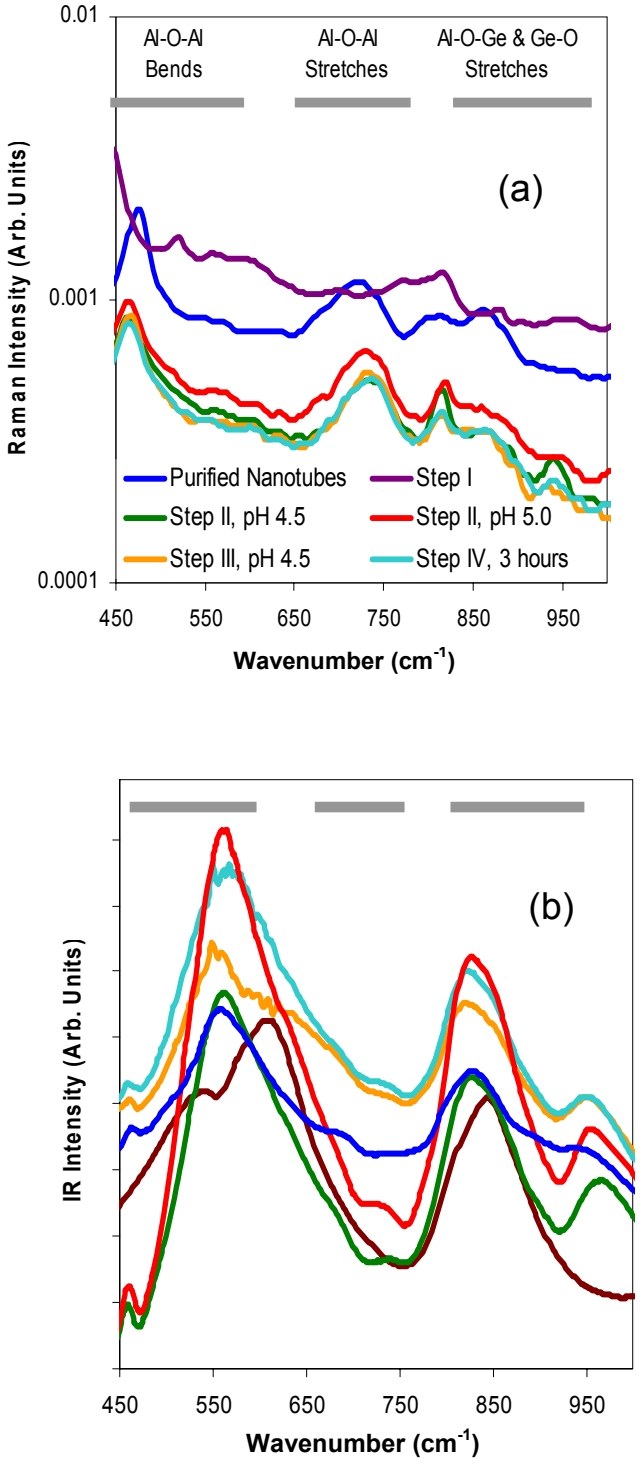

Figure 3-5: (a) Raman spectra of freeze-dried samples during Steps I-IV, and the purified nanotube product. (b) Infrared spectra of the same samples. The legend for both figures is the same. Important vibrational band regions are labeled identically in both figure.

II-IV). Secondly, the vibrational spectra of the precursors in Steps II-IV are very similar to that of the purified nanotubes obtained as the final product of an independent synthesis experiment. In particular, they show that Al-O-Al and Al-O-Ge linkages have been formed with similar Raman and IR frequencies as in the nanotube product, whose vibrational bands have been assigned qualitatively in previous work [80]. The 'Al-O-Al bending and stretching' frequency regions, as well as the 'Al-O-Ge and Ge-O stretching' frequency regions for the nanotube product are labeled. Note that bands with high Raman intensity usually have low IR intensity, and vice versa. For example, the Al-O-Al mode at 450 cm^{-1} is intense in the Raman and weak in the IR spectrum, whereas the modes around 550 cm^{-1} are weak in the Raman and intense in the IR spectrum. Similarly, the Al-O-Al stretching mode at 700 cm^{-1} is intense in Raman and weak in the IR spectrum. The Al-O-Ge and Ge-O stretching bands at 810, 850, and 950 cm^{-1} are relatively weak in the Raman spectrum but more intense in the IR spectrum.

Finally, we used liquid-phase UV-Vis spectroscopy to prove that there are no structurally ordered species at any stage of the Steps I-IV. UV-Vis spectroscopy is an excellent probe of structural order in oxide materials (also see following sections), and allows us to easily distinguish between ordered nanotubes and amorphous nanoparticles or precursors even at nanomolar concentrations. The UV-Vis spectra of the solutions in Steps I-IV are completely featureless, as expected from aqueous solutions of aluminate and germanate precursors (whether monomeric or oligomeric). No ordered materials are observed by TEM, electron diffraction, or XRD on the solid products after freeze-drying.

Together, the DLS, Raman, IR, and UV-Vis data provide insight on how control of chemical bonding in the precursor solution can influence nanotube synthesis. The role of Step II (basification) is to promote co-condensation of aluminum and germanium precursors into small (sub-nanometer) aluminogermanate precursors in which the chemical bonding resembles that of the aluminum and germanium atoms in the final nanotube product. The role of Step III (partial re-acidification to pH 4.5) is to prevent precipitation of amorphous materials that begins when basification reaches pH 5 (as evinced by the appearance of nanoparticles in the DLS measurements). Furthermore, our data confirm the existence of only *sub-nanometer precursors* before temperature changes are applied, save for the temporary appearance of *amorphous nanoparticles* (only in Step II, when pH ~ 5).

3.3.2 Nanotube Formation

Next, we studied the formation of nanotubes during Step V, as a function of reaction time (up to 300 hours) and temperature (65°C-95°C) in a batch reactor configuration. Additional seeded-batch and semi-batch experiments were carried out at 95°C. Together, these experiments provide critical information on the nanotube growth mechanism and eliminate other possible models. In each case, multiple experiments were carried out over a total period of more than a year to ensure reproducibility and realistic error estimates on the quantitative measures of nanotube growth. We can quantitatively obtain *average nanoparticle sizes* in the reactor from DLS autocorrelation functions, as well as the *mass concentration of only nanotubes* from UV-Vis absorption intensities. We

can also obtain (semi-quantitatively) the *total concentration of all nanoparticles* (nanotubular as well as amorphous) from DLS photon scattering signal intensities.

3.3.2.1 Average Nanoparticle Size and Concentration

Figure 3-6 shows the average nanoparticle size obtained from DLS as a function of reaction time and reaction temperature. Nanoparticles of size 5-7 nm appear immediately upon heating but do not exist prior to this step. Thereafter, we see a slow increase in the average particle size. The 'apparent rate of growth' of the nanoparticles varies from 0.04 nm/hr at 95°C to 0.001 nm/hr at 65°C. If interpreted in terms of a model that involves addition of precursors to nanotube ends, this rate of growth is negligible.

Figure 3-7 shows the photon scattering signal intensity (measured during DLS experiments) as a function of reaction time. The intensity has been normalized by the nanoparticle size (obtained simultaneously from the DLS autocorrelation function). This is because the intensity is proportional to the product of the concentration and the molecular weight (which in the case of a 1-D nanotube is proportional to its length) [94]. Thus, the normalization to the particle size semi-quantitatively isolates the contribution from increasing nanotube concentration. As in the case of the UV-Vis spectra, the total concentration of nanoparticles in the solution is seen to be increasing substantially with time at higher temperatures of reaction.

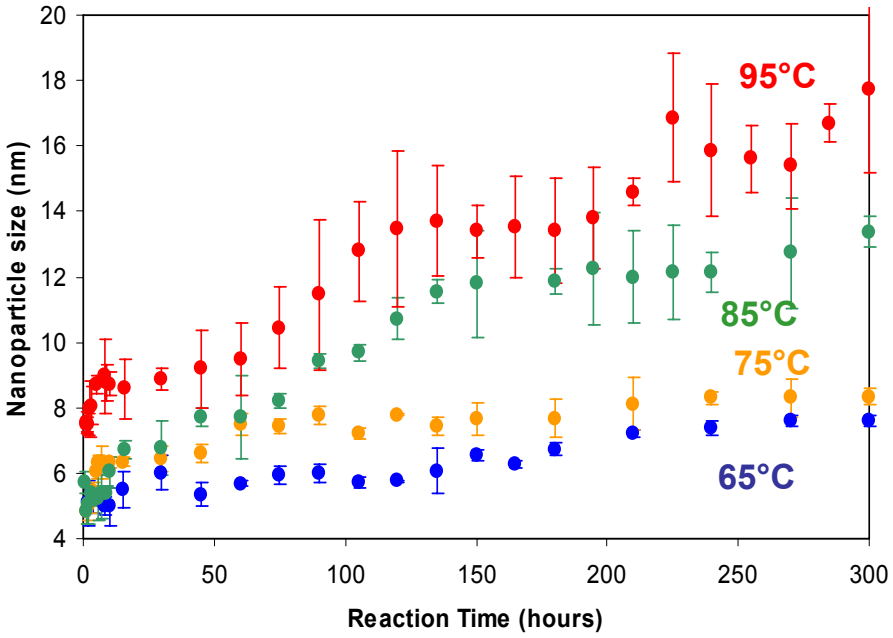

Figure 3-6: Average nanoparticle size versus time obtained from dynamic light scattering.

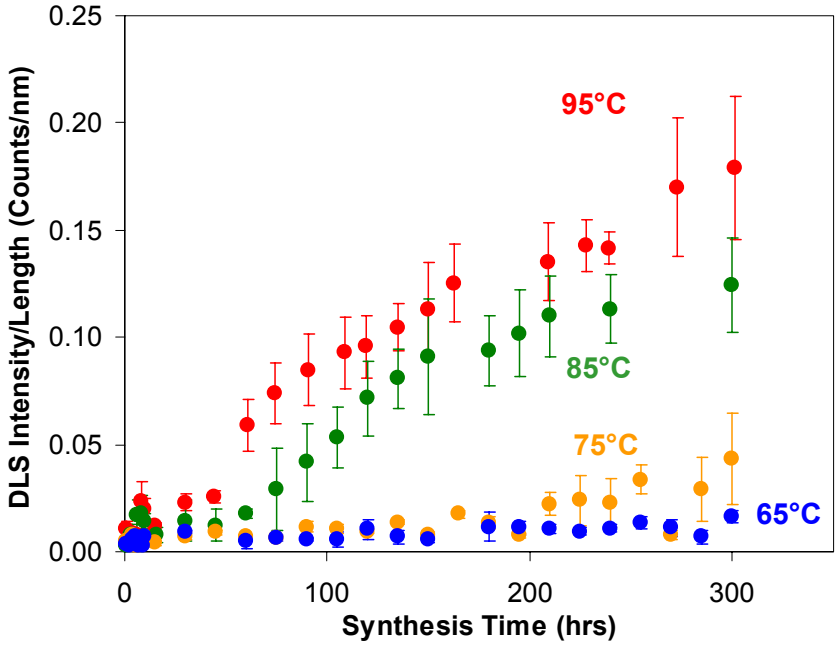

Figure 3-7: Semi-quantitative measurement of total nanoparticle concentration versus time, from dynamic light scattering signal intensity.

3.3.2.2 Effect of Excess Precursors on Nanotube Growth

We also carried out other experiments to examine the possibility of growth by NT nucleation in solution followed by addition of dissolved precursors to the NT ends. Figure 3-8 presents DLS particle sizes measured during seeded-batch and semi-batch experiments at 95°C in comparison to the batch experiment data. In seeded growth, 5 mL of a suspension of purified NTs (of size 19 nm as obtained by a prior DLS measurement) was added to the reactor at the onset of Step V. The amount of nanotubes added was such that their average length would increase by a factor of 3 during the reaction time if the nanotube formation was dominated by end-growth. However, Figure 3-8 shows that the particle sizes do not increase substantially, and both the batch and seeded-batch reactions tend to converge to a similar nanoparticle size at long times. The main difference is the initially larger average particle size in the seeded-growth experiment, owing to the addition of NTs at the beginning of Step V. Another important fact is that the nanotube length is not limited by declining precursor concentration in the batch reactor experiments, even as the nanotube concentration continues to increase after long reaction times of 300 hours at 95°C. This point was further verified by a semi-batch experiment, in which reactants were continuously added to the reactor during the synthesis. In this case, the initial concentration of the precursors was the same as in the batch reaction, but the initial volume of solution was only 25 mL. Precursor solution was continuously added to the reactor at a rate of 5 mL/hr. The evolution of the average nanoparticle dimensions measured by DLS (Figure 3-8) shows no substantial differences from the batch experiments at long times. Finally, the size of the purified NTs (obtained by dialysis of

the solution after reaction) was almost constant (at 19±2 nm) irrespective of the growth method (Figure 3-8).

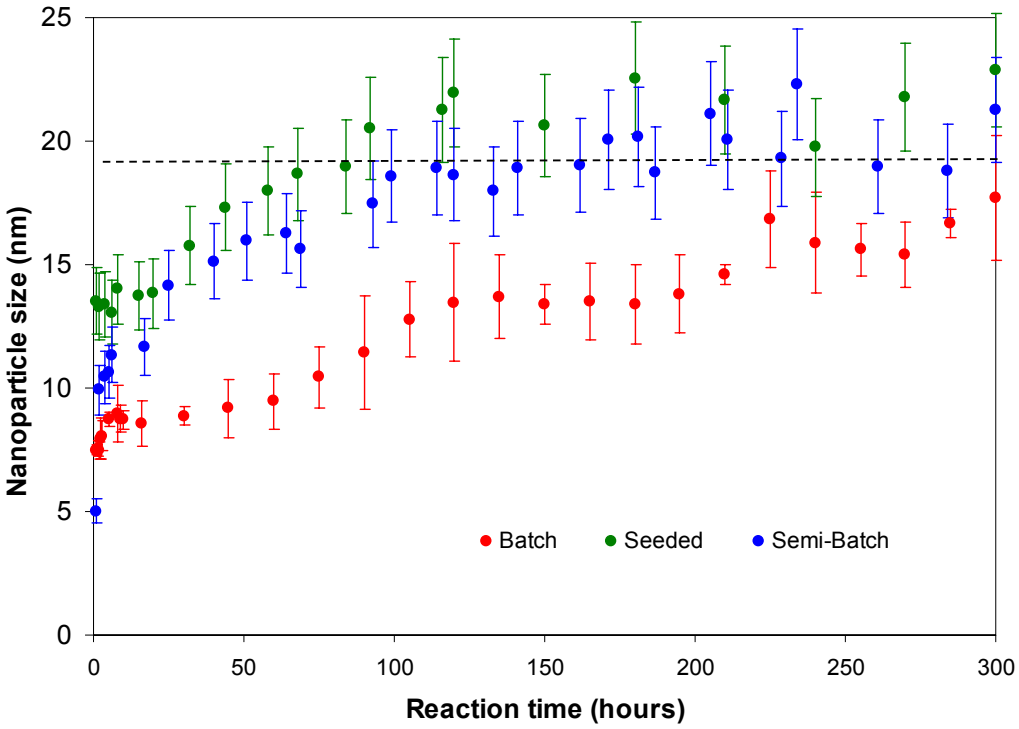

Figure 3-8: Comparison of DLS nanoparticle sizes obtained from batch, seeded-batch, and semi-batch growth. The dashed line shows the nanoparticle size measured from purified (dialyzed) nanotube products of the three reactions after 300 hours.

3.3.2.3 Nanotube Concentration

3.3.2.3.1 UV-Vis Analysis

UV-Vis spectroscopy, unlike DLS, is capable in identifying ordered materials. Figure 3-9 shows the UV-Vis spectra obtained at 95°C for different reaction times. This

is also the first report of the optical properties of these materials, which are wide band gap semiconductors (with E_g = 3.6 eV). The sharp, intense peaks may reveal the presence of confined excitons and other phenomena that are currently of considerable interest in the photonic applications of nanoparticles [88, 115-119]. The spectra differ only in the intensity of the peaks, which is proportional to the concentration of nanotubes in the solution. According to Beer-Lambert's law, the absorbance varies linearly with the concentration of ordered material in solution, i.e $A = \varepsilon bC$, where A = absorbance, C = concentration of nanotubes, ε = molar absorptivity and b = path length. The molar absorptivity and path length are constant if the structure of the absorbing material (in this case the nanotubes) and the experimental set-up remain unaltered, as is the case here. Using this linear relationship, the concentration of the nanotubes can be calculated from the absorption spectra.

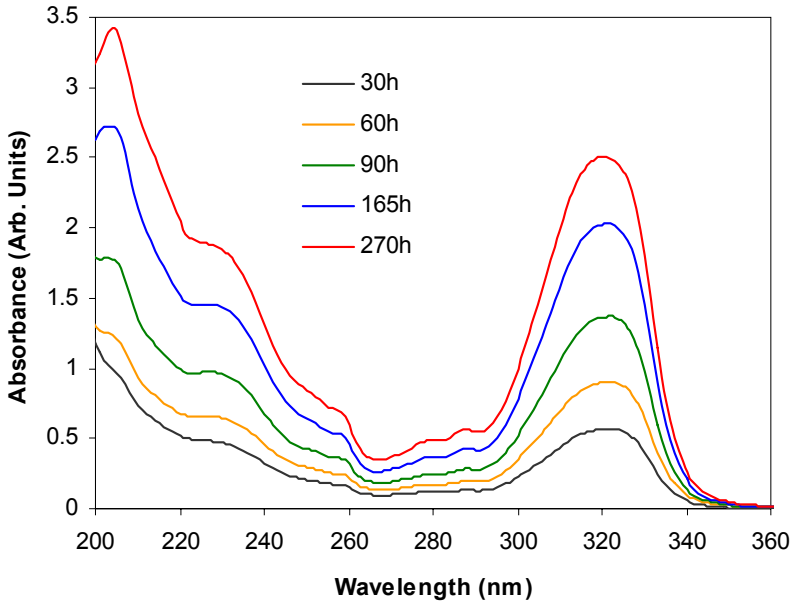

Figure 3-9: UV-Vis spectra of the solution at various times during reaction at 95°C.

As seen in Figure 3-9, the AlGe nanotubes absorb in the 200-400 nm regime with the most intense absorption at around 320 nm. With increase in synthesis time the intensity of all the peaks increases, but the 320 nm peak was the most distinguishable. Thus, the total area under the 320 nm peak was used to track the nanotube concentration.

For each spectra, a double exponential background subtraction was followed by fitting the spectra with the minimum number of Gaussians [117]. An example of a fit is shown in Figure 3-10, where the hollow circles represent the data (95°C synthesis at 165h) and the solid line represents the fit. The black solid line is the double exponential background and the Gaussians are shown in solid curves. Here, the total absorbance (*A*) due to ordered AlGe nanotubes in solution is represented by the total area under the 3 Gaussians fitting the intense 320 nm peak.

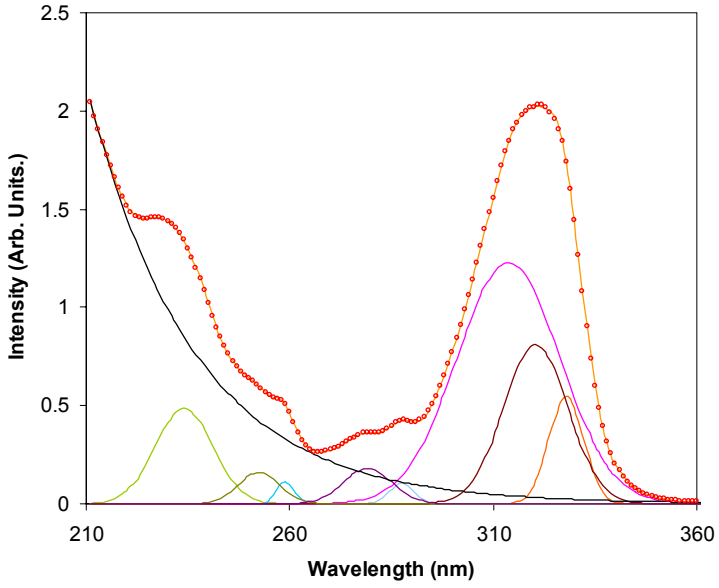

Figure 3-10: Fitted UV-Vis spectra of AlGe nanotube at 165 h and 95°C.

3.3.2.3.2 Results

Figure 3-11 shows detailed UV-Vis data obtained at four synthesis temperatures. The spectra differ only in the intensity of the peaks, which is proportional to the concentration of nanotubes in the solution as explained in the previous section. Using Figure 3-11, we construct the plot of Figure 3-12 which shows the evolution of the nanotube concentration as a function of time.

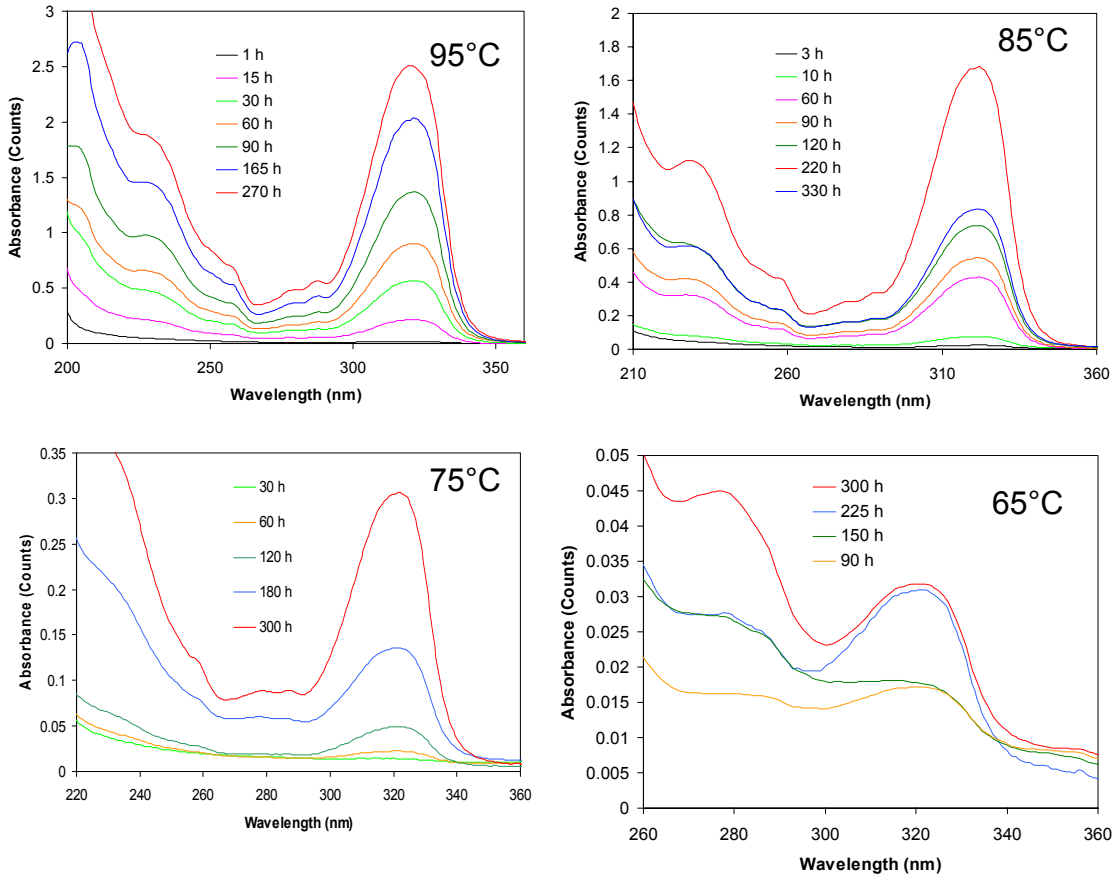

Figure 3-11: UV-Vis spectra of AlGe nanotubes as a function of synthesis time and temperature.

While for the 95°C and 85°C synthesis, the appearance of ordered nanotube structures are visible early (~ 1h) in the synthesis. On the other hand for the 75°C and 65°C synthesis the nanotubes are detected only after 30h and 90h of synthesis respectively. It should be noted, however, that from DLS analysis (Figure 3-6) nanoparticles appear early (~ 1h) even for the 65°C and 75C synthesis temperatures. These observations indicates the presence of disordered nanoparticles, which forms early in the reaction. Moreover, the concentration of nanotubes for the 65°C synthesis is 2 orders of magnitude lower than the 95°C counterpart, which indicates that the transition of the nanoparticles to nanotubes is an activated process.

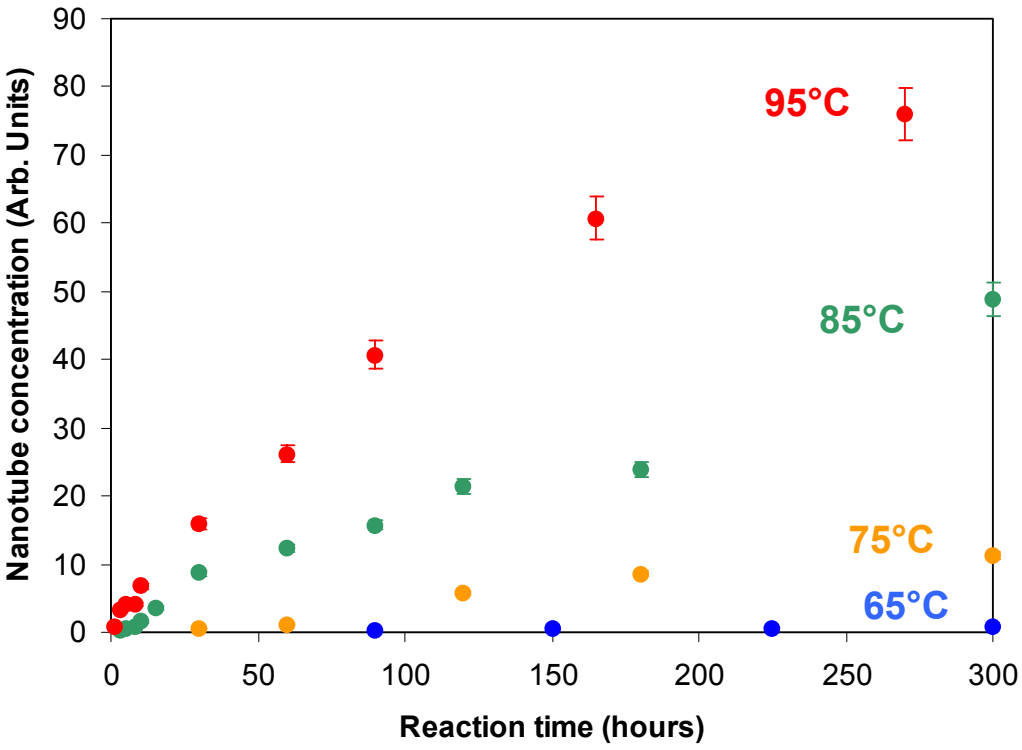

Figure 3-12: Concentration of nanotubes, obtained from the 320 nm excitation as a function of growth time.

Together, Figure 3-6 to Figure 3-12 reveal the central mechanistic aspects of the nanotube growth. The temperature rise at the onset of Step V results in the condensation of Amorphous NanoParticles ('ANPs') of size ~ 5-7 nm (Figure 3-6) and low concentration (Figure 3-7). At the higher reaction temperatures, ordered NanoTubes ('NTs') begin to emerge at an early stage (a few hours) as evinced by the appearance of peaks in UV-Vis spectra (Figure 3-11 and Figure 3-12). The UV-Vis spectra remain practically the same (except for the increasing intensity) throughout the reaction, and result from increasing concentrations of the same ordered material as the reaction proceeds. At the same time, the average nanoparticle size increases slowly over the reaction time of 300 hours.

Based on all the results, the apparent increase of nanoparticle size during the reaction (as observed in DLS) is not primarily due to the increase in the nanotube length by solution-phase addition of growth units to the ends, but rather due to evolution of the ANPs into low-density (porous), short, ordered NTs by self-assembly as evinced by the UV-Vis spectra. Simultaneously, limited aggregation of the ANPs may increase the average nanoparticle size and size distribution. In the next section, we explain the mechanistic implications of the combined DLS and UV-Vis studies described above.

3.3.3 Overall Mechanism and Quantitative Kinetic Model

We are now in a position to propose a nanotube formation mechanism (Figure 3-13) that we believe to be conclusive in its essential aspects. The initial Steps I-IV

induce the formation of aluminogermanate precursors that are capable of assembly into the nanotube structure. The formation of ANPs from precursors in Step V can be considered (in general) as a reversible reaction. Having excluded the possibility of liquid-phase growth of the NTs, the ANPs (once formed) must be evolving irreversibly into ordered NTs primarily through internal self-assembly as indicated in Figure 3-13. There is a unique energy minimum in this system as a function of the nanotube diameter [114, 120], which is likely to be important in causing self-assembly into NTs of monodisperse diameter within the confines of the ANPs. Regarding the role of amorphous nanoparticles and their evolution to ordered materials, we also note a remarkable similarity between the nanotube formation mechanism deduced here (following our speculation in a previous work [38]) and the reported mechanisms of nanoporous crystal (zeolite) formation [86, 121-123]. In the latter case, aggregation processes are additionally important for the formation of bulk crystalline materials [124]. On the other hand, the much more dilute concentrations encountered in the nanotube system can be expected to limit the aggregation processes and lead to the formation of nanoscale (rather than bulk) materials. In other words, each NT can be formed from only a few ANPs (and from a minimum of one ANP). One objective of our ongoing investigations is to ascertain quantitatively the role of aggregation that may occur in parallel to the ANP → NT transformation processes. The role of amorphous nanoparticles has also been suggested to be of profound importance in biomineralization at the interface of biological structures with aqueous environments [124, 125]. Very recently, pH-influenced condensation has also been shown to influence the formation of dense germanium oxide nanoparticles [126].

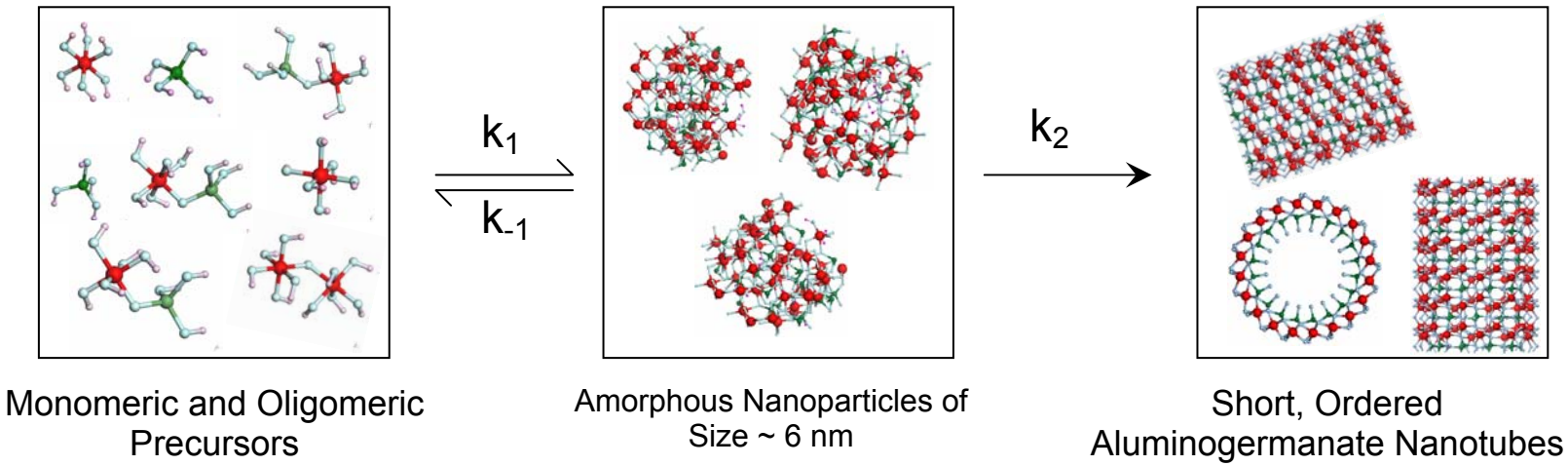

Figure 3-13: Schematic representation of the aluminogermanate nanotube growth mechanism. Red: aluminum, green: silicon, light blue: oxygen, grey: hydrogen.

3.3.3.1 Quantitative Kinetic Model

The UV-Vis concentration data and the DLS particle size data can be well fitted (Figure 3-14 and Figure 3-15) to a simple two-step mathematical model based on Figure 3-13, that involves reversible first-order formation of ANPs from precursors, followed by irreversible first-order formation of NTs. Note that the ANP evolution to NTs may involve a series of rearrangements (involving hydrolysis and condensation) of atoms within the ANPs, and even limited aggregation of the ANPs. Here, we use bulk concentrations $C_A(t)$ and $C_N(t)$ to represent the concentration of ANPs and the fully evolved NTs respectively, with the internal rearrangements, precursor-ANP exchange, and any aggregation processes being represented by effective rate constants shown in Figure 3-13.

Such a 'minimalist' model can be used to capture the main features of the nanotube assembly mechanism, and similar models have been applied to describe crystal growth by nanoparticle aggregation [86, 127]. A quasi-steady-state assumption is made for the ANP concentration, which remains low throughout the reaction as seen in the experiments carried out at 65°C and 75°C (Figure 3-12). Thus, the model relates the concentrations of the precursors (C_P), ANPs (C_A) and NTs (C_N) through the three first-order rate equations:

$$\frac{dC_p}{dt} = -k_1 C_P + k_{-1} C_A \tag{3.3}$$

$$\frac{dC_A}{dt} = \left(\frac{k_1}{N_P}\right) C_P - \left(\frac{k_{-1}}{N_P}\right) C_A - k_2 C_A \tag{3.4}$$

$$\frac{dC_N}{dt} = k_2 C_A \tag{3.5}$$

Here N_P is the number of precursors condensing into a single ANP. The rate equations can then be integrated analytically, and the resulting $C_A(t)$ and $C_N(t)$ can be used to fit the effective overall rate constant (K) for nanotube formation, as well as that for the ANP → NT transformation (k_2). The QSS approximation ($dC_A/dt \sim 0$) leads to the following three expressions:

$$C_P(t) = C_{P0} e^{-Kt} \tag{3.6}$$

$$C_A(t) = \left(\frac{KC_{P0}}{k_2 N_P} \right) e^{-Kt} \tag{3.7}$$

$$C_N(t) = \left(\frac{C_{P0}}{N_P} \right) (1 - e^{-Kt}) \tag{3.8}$$

Here, K is the overall pseudo-first-order rate constant for NT formation and C_{P0} is the initial precursor concentration, where:

$$K = \frac{k_1 k_2}{\left(\frac{k_{-1}}{N_P} + k_2 \right)} \tag{3.9}$$

3.3.3.2 Model Fitting to Obtain Kinetic Parameters

We first fit the measured UV-Vis intensity which is proportional to the NT concentration (Figure 3-14):

$$I_{UV} = \alpha_1 C_N = \alpha_1' (1 - e^{-Kt}) \tag{3.10}$$

Here α_1 is the instrumental calibration factor where:

$$\alpha_1' = \frac{\alpha_1 C_{P0}}{N_P} \tag{3.11}$$

This fit has only two parameters: K and α_1'. Figure 3-14 shows the resulting least square fit and the subsequent fit parameters are shown in Table 3-1.

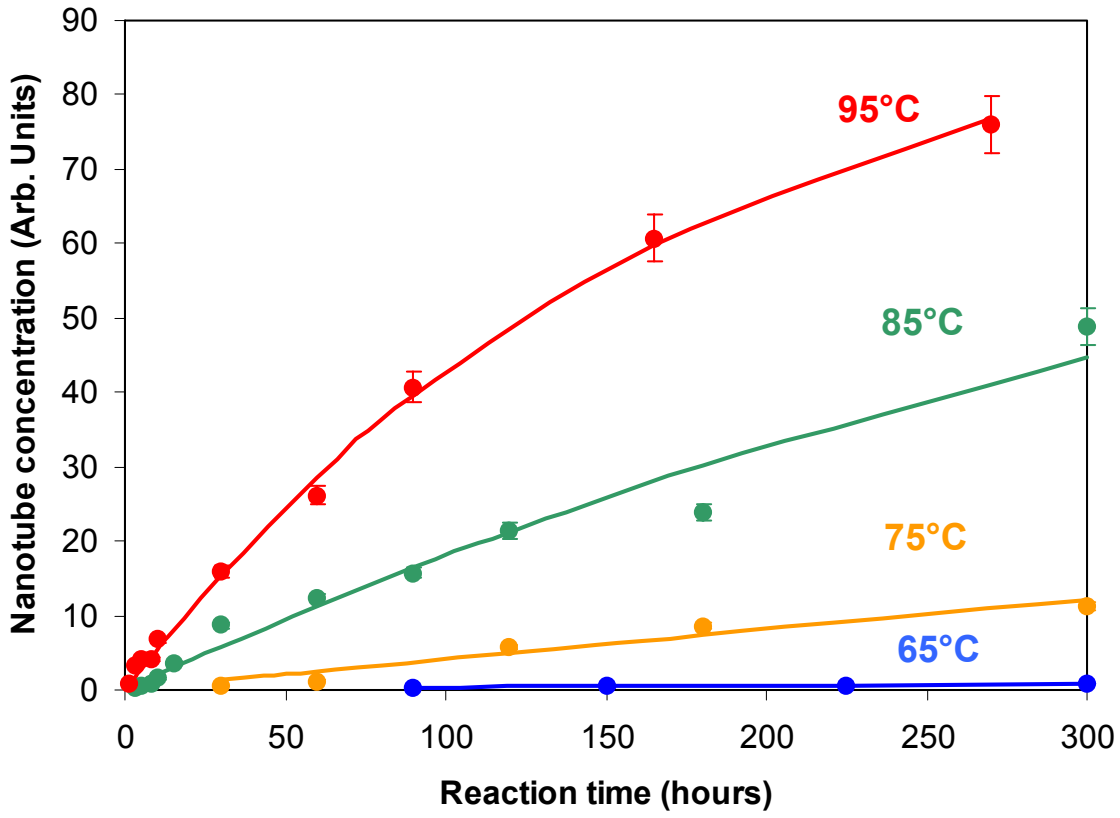

Figure 3-14: Nanotube concentration obtained from UV-Vis analysis. The solid lines show the least square fits.

Then we fit the measured average DLS particle size (Figure 3-15), which at low concentrations is well described by an arithmetic average of the sizes of ANPs (L_A) and NTs (L_N):

$$\bar{L}_{DLS} = \frac{L_A C_A + L_N C_N}{C_A + C_N} \tag{3.12}$$

Substituting the model expressions for C_A (Equation 3.7) and C_N (Equation 3.8) the fit of the DLS particle size over the four temperatures involves three parameters: L_A, L_N, and k_2 (since K is already determined). The fitted DLS data is shown in Figure 3-15.

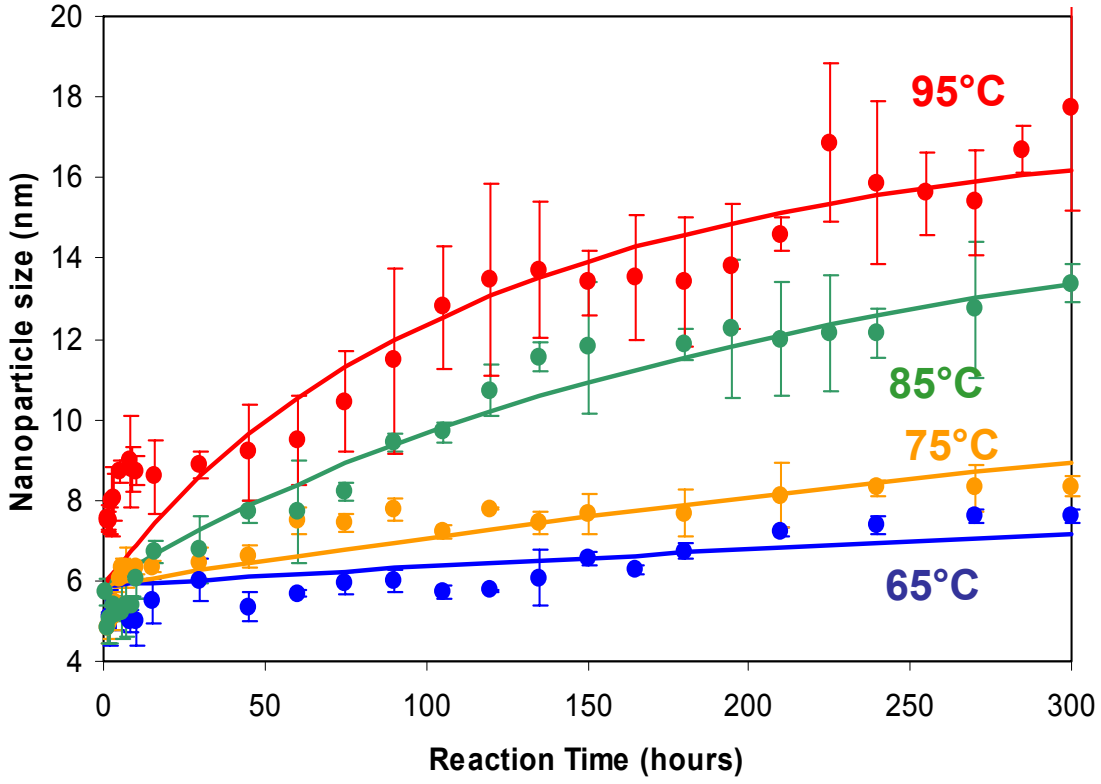

Figure 3-15: Average nanoparticle size from DLS analysis. The solid lines show the least square fits.

Overall, this simple model captures all the trends in the evolution of nanoparticle size and NT concentration. The ANP and NT sizes can be fitted as practically independent of temperature within the range of conditions investigated. The fit results

can easily be improved by specifying a temperature-dependent ANP size, although this leads to introduction of a larger number of parameters.

Table 3-1: Summary of model fit parameters.

T (°C)	Fitted K (h^{-1})	Fitted k_2 (h^{-1})	Fitted α_1'
95°C	5.78×10^{-3}	9.16×10^{-3}	97.45
85°C	2.05×10^{-3}	4.29×10^{-3}	97.45
75°C	4.39×10^{-4}	1.11×10^{3}	97.45
65°C	2.87×10^{-5}	4.15×10^{-4}	97.45
Fitted Length of Nanotube (L_N) = 18 nm			
Fitted Diameter of Amorphous Nanoparticle (L_A) = 6 nm			

The value of α_1' is found to be temperature-independent, and is assumed as such during the nonlinear least squares. The fitted sizes of the nanotube and the amorphous nanoparticle were initially assumed to be temperature-dependent, but the results were within the resolution of DLS. Hence, the fit was performed again with the assumption of temperature-independent nanotube and amorphous nanoparticle size, to yield the final set of parameters listed in the Table 3-1. The determination of the effective activation energies from the fitted rate constants is shown below in Figure 3-16.

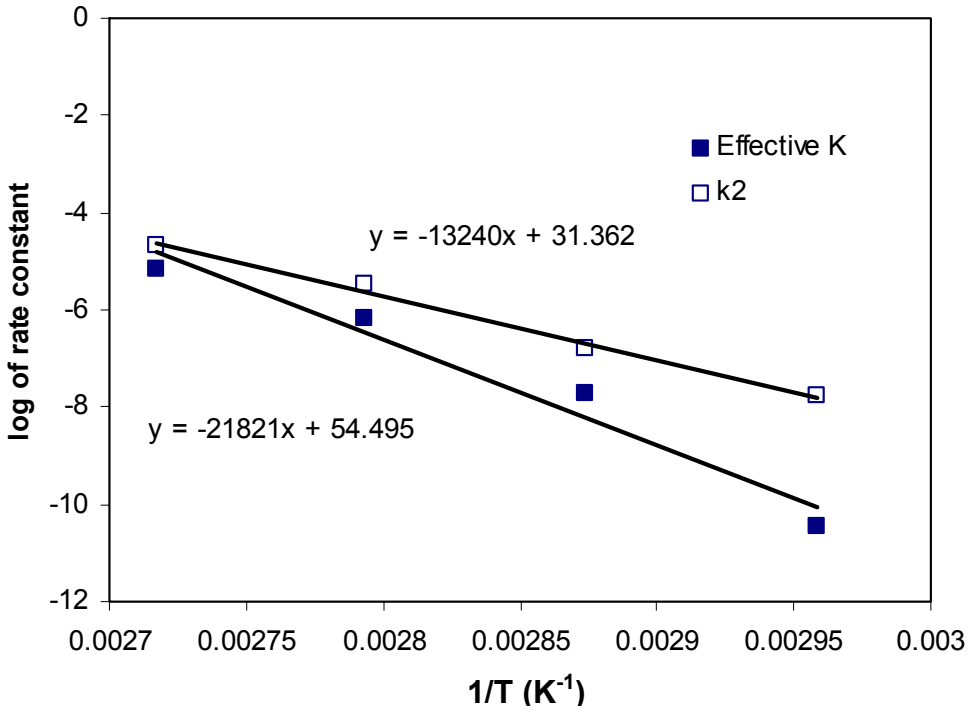

Figure 3-16: Activation energies for the two fitted rate constants K and k_2.

The fitted rate constants K and k_2 were well described by Arrhenius expressions to yield the activation energies as shown in Figure 3-16. The kinetic experiments done at four temperatures yield effective activation energies of 181±6 kJ/mol and 110±7 kJ/mol for K (overall 'precursors → NT') and k_2 ('ANP → NT') respectively (see Supplementary Information for further details), which are well within physical possibility for oxide formation [124, 128]. The fitted ANP size (6 ± 1 nm) and the fully-evolved NT length (18 ± 3 nm) are in agreement with the DLS and TEM [38] observations of the pure dialyzed materials. As mentioned earlier, the changing particle sizes measured in DLS experiments are not primarily because of an increase in NT length due to solution-phase growth by precursor addition, but rather because the concentration

of the (longer) NTs continues to grow in proportion to that of the (compact) ANPs. Hence, the average particle size measured by DLS increases with time.

We further emphasize that the mechanism does not preclude the concurrent role of processes such as aggregation of the ANPs, which would have the effect of increasing the average size (and size distribution) of the ANPs and thus causing an increase in the average length (and length distribution) of the NT that is eventually formed. The possible role of aggregation processes, as well as the effects of parameters such as increasing precursor concentration, are under investigation and are considered to be outside the scope of this investigation. However, the central aspect of the mechanism is the discovery that the dissolved nanotube precursors are condensed into amorphous nanoparticles containing localized precursors, thus allowing the assembly of ordered nanotubes of small sizes and whose structure is controlled by the nature of the precursors.

This is a novel concept as pertaining to nanotube synthesis, and for the synthesis of highly ordered nanoscale metal oxide objects in general. The application of this mechanism in combination with metal oxide chemistry and variations in parameters such as the ionic strength (which can influence nucleation, growth, and aggregation processes), precursor concentration, and even the solvent, may allow development of more generalized processes based on amorphous nanoparticle condensation and self-assembly to yield very small metal oxide nanotube objects of tunable composition and functionality - a highly desirable goal of nanomaterials science and technology. As illustrated here, such routes could exploit the fact that a large number of metals are well known to form

layered oxides, oxyhydroxides, and hydroxides [129]. Such a tendency can potentially be diverted to induce nanotube formation *via* co-condensing ions (such as germanate, silicate, and phosphate) that alter the chemical bonding and energetics of the system as seen in the current synthesis. Furthermore, the fact that the ANPs necessarily contain only a few thousand atoms may allow computational prediction/design of their self-assembly into ordered objects leading to synthesis of new classes of nanomaterials.

3.4 Conclusion

We have described in this Chapter, the essential mechanistic aspects of a route towards the assembly of very small (~ 20 nm), structurally ordered, single-walled aluminogermanate nanotubes in aqueous conditions. A combination of solution phase (dynamic light scattering and UV-Vis spectroscopy) and solid phase (Raman, FTIR, electron diffraction, TEM) characterization methods with necessary variations of the basic synthesis process, leads to a mechanism that involves first the use of pH control to generate alumiongermanate precursors with appropriate chemical bonding conducive to assembly into nanotubes, followed by the use of temperature control (at 65-95°C) to condense these precursors into amorphous nanoparticles (ANPs) of size ~ 6 nm, and finally the self-assembly of short, ordered aluminogermanate nanotubes (NTs) of size (~ 20 nm) from these amorphous condensates. A two-step kinetic model of this process can capture the main features of the mechanism, *viz.* increasing NT concentration and slowly changing average nanoparticle size, both of which are due to the ANP→NT transformation.

Chapter 4 : Dimension Control of Mixed Metal Oxide Nanotubes

4.1 Introduction

The unique properties of nanoscale materials can be primarily attributed to the shape and size of the functional features in the material. For example, the size and shape of the pores or channels in a zeolite determines its particular separation applications. In electronics and photonics, the size and shape of semiconductor nanomaterials determines the shape and height of the potential well in which an electron or hole can be confined [130, 131]. Such semiconductor nanomaterials, also called quantum dots [130], have created a field of active research targeted at a wide range of photonic applications. Recently, there have been significant interest in semiconductor nanomaterials with tunable dimensions [132] e.g. cadmium selenide nanorods. It has also been shown that the emission photoluminescence spectra of these materials change with both the diameter and length of the nanorods [115].

Although shape and size control of nanomaterials are clearly important in controlling their properties, there is little systematic knowledge of these aspects in the case of nanotube materials. Most 1-D nanomaterials (nanotubes, nanorods, nanobelts etc) are assumed to be a product of various crystal nucleation and growth mechanisms [34]. Although this model is adequate to explain the growth mechanism in some of the materials, it has not led to an effective method to control size and shape. Ultimately, nanoscale material synthesis would require adequate control of parameters so as to

effectively change product properties (specifically the dimension and composition) and produce materials for specific applications.

In this Chapter, we demonstrate the capability of synthesizing AlumuminoSilicoGermante (AlSiGe) nanotubes with desired Si to Ge ratio. Here, we investigate the change of dimensions with composition of the nanotubes. XPS analyses, as well as a quantitative FTIR method developed here, have been used to measure the composition of the product nanotubes vis-a-vis that of the precursor solution composition. XRD analysis was used to calculate the external diameter of the product nanotubes as a function of composition. DLS analysis was used to obtain the length of the nanotubes.

4.2 Experimental Section

4.2.1 Synthesis

Depending on the desired content of Ge in the mixed metal oxide nanotubes, TetraEthylOrthosilicate (TEOS – Si precursor) and TetraEthylOrthoGermanate (TEOG – Ge precursor) were added drop-wise to a stirred solution of 5 millimolar (mM) $AlCl_3$ solution until the Al:(Si+Ge) ratio was 1.8, and left to stand for 45 mins under vigorous stirring. Then a 0.1 N NaOH solution was added at the rate of 0.3 ml/min until the pH of the solution reached 5.0. The pH was brought down immediately to 4.5 by drop-wise addition of a solution containing 0.1 M HCl and 0.2 M of acetic acid. The resulting clear

solution was allowed to stir for 3 hrs and then reacted at 95ºC under reflux conditions for 120 h. Then the solution was cooled to room temperature and 0.1 N Ammonia solution was added carefully until the pH reached 8.0. At this point the solution turned murky and was centrifuged at 3000 rpm for 20 min. The supernatant was discarded and the gel acidified with a few drops of 12 N HCl. The resulting solution was immediately dialyzed against deionized water for 120 hrs to remove any unreacted precursors as well as sodium and chlorine ions. For DLS analysis, 5 ml of the sample was filtered through a 0.2 μm pore size syringe filter to produce a dust-free sample containing only nanoscale particles. 5 ml of dialyzed solution was evaporated over a glass slide to deposit a film of nanotubes amenable to XRD and XPS (X-ray Photoelectron Spectroscopy) analysis. A portion of the dialyzed sample was freeze-dried for FTIR measurements.

4.2.2. Characterization

Thin film XRD analysis was performed on a PAnalytical X'pert Pro diffractometer operating with a Cu Kα source and equipped with a diffracted beam collimator and a Miniprop detector. The data were collected in grazing angle incidence mode, with the incident beam at a fixed grazing angle of 1º with respect to the sample plane, and the detector scanning over angles from 2º to 30º with respect to the same plane.

The nanotube films were analyzed for surface composition with a PH1 Model SCA 1600 XPS instrument equipped with a monochromatic Al Kα source (1486.4 eV)

and a spherical capacitor analyzer operating at 187.85 eV pass energy. High resolution spectra (0.05 eV/step and 50 ms/step) were collected for bond information by peak deconvolution using Gauss-Lorentzian peaks. DLS data were collected with a Wyatt DAWN EOS instrument. The scattering angle was 108º and the wavelength of the laser was 690 nm. The autocorrelator delay time (τ) was 1 μs. A series of 120 scans were performed on the sample, each with a 1-second acquisition time. FT-IR was performed on freeze-dried samples. The dialyzed liquid samples were immediately frozen at -20°C before application of vacuum. FT-IR spectra were collected with a resolution of 8 cm^{-1} under vacuum conditions on a Bruker IFS 66v/S spectrometer.

4.3 Results and Discussion

4.3.1 Chemical Composition of the Nanotubes

Once the AlSiGe nanotubes are synthesized, it is important to analytically estimate the actual composition of the products. This is to ensure that the amount of the Si to Ge ratio intended to be present in the nanotubes during synthesis is reflected accurately in the products. Two independent elemental composition techniques have been used for comparison; XPS and FTIR. Using XPS, elemental composition of a sample is performed by running multiplex scans at specified energy ranges. This procedure is also called deconvolution scanning. Using this data an elemental composition estimate is supplied by the software in atomic percentages. Obtaining composition from FTIR analysis required more intensive approach described below.

4.3.1.1 Determination of Chemical Composition from FTIR Analysis

The IR peak intensity is a function of number concentration of the particular vibration it represents [133] given by the Beer-Lambert law. For example, the intensity of the Al-O stretching peak at 450 cm^{-1} would linearly increase in intensity with the number concentrations of the Al-O bonds. Thus, quantitative composition information can be indirectly derived from IR spectra. For solid-state IR, however, there are peak broadening effects which make calibration with intensities very inaccurate [134]. Instead, peak areas are considered an accurate calibration measure [135] for all spectroscopic technique and which can be linearly related to the number concentrations.

In order to quantitatively compare composition of different set of samples, the IR spectrum needs to be normalized with respect to any one of the element that has a fixed composition in all the respective samples. In the case of the AlSiGe nanotubes it is the Al, since amount of Al in the synthesis remains constant and the Ge to Si ratio is altered. The amount of sample used in a particular experiment is subject to experimental error, which may/may not be substantial for any quantitative analysis. To avoid such errors the spectra was normalize on the basis of Al content. The IR peaks from 400 cm^{-1} to 790 cm^{-1} corresponds to the Al-O and Al-O-H vibrations [76, 79, 80, 96]. The complete spectra was normalized with respect to the area under the spectra in the 400 cm^{-1} to 790 cm^{-1} range. This means that regardless of the amount of nanotube sample in the path of the IR, the spectra suggests that the Al content irradiated by the IR beam is the same for all samples.

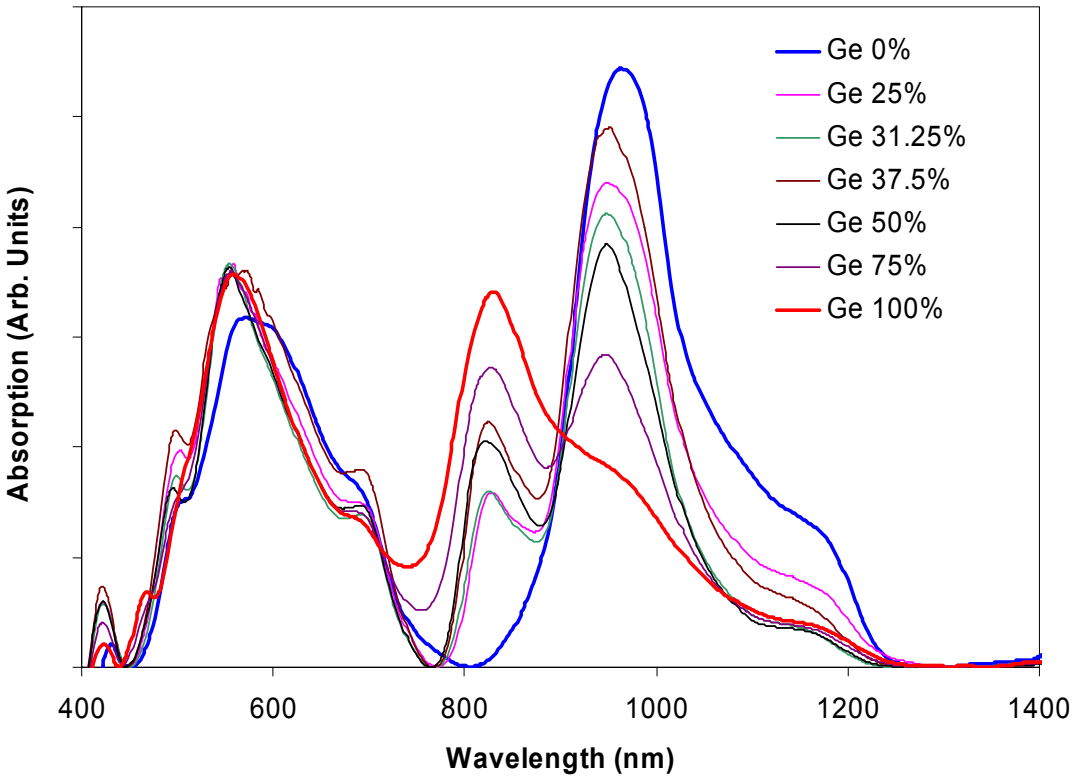

Figure 4-1: FTIR spectra of freeze dried mixed metal oxide nanotubes. The legend indicates Ge content in the respective nanotubes.

Figure 4-1 shows the Al normalized FTIR spectra of the purified and freeze-dried mixed metal oxide nanotubes. The pure AlGe and pure AlSi nanotube spectra are shown in bold red and blue respectively for clear visual comparison. The legend shows the experimental composition of the metal oxide nanotubes represented as the percentage Ge, i.e. mathematically Ge/(Ge+Si) × 100. As mentioned in the previous paragraph the peaks from 400 cm^{-1} to 790 cm^{-1} corresponds to the Al-O and Al-O-H vibrations, which remains unaltered in all the samples. A clear difference is noted between the AlGe and

AlSi nanotube spectra with the shift of the most intense peak from 810 cm^{-1} to 910 cm^{-1} as the Ge content decreases. This observation is in agreement with previous reports [80].

In order to quantify the Ge to Si ratio in the mixed metal oxide nanotubes a rigorous curve fitting procedure was developed. Firstly, the pure nanotube (AlGe and AlSi nanotube) spectra were fitted to minimum number of Gaussians to obtain an accurate fit. Then, keeping the peak positions fixed and varying the intensity and peak widths of all the Gaussians in the pure nanotube spectra, all the respective AlSiGe nanotube spectra was fitted. The peak fits for the mixed metal oxide nanotubes are shown in Figure 4-2. From previous work on these materials [80] it is known that the peak positions in the 800 cm^{-1} to 1000 cm^{-1} range is of interest in compositional analysis. For pure AlGe nanotubes they are the Ge peaks (Ge-O and Ge-O-H vibrations) and for the pure AlSi nanotube spectra, they are the Si peaks (Si-O and Si-O-H vibrations). In the AlSiGe nanotubes, however, all the Si and Ge peaks coexist and ratio of the areas of the respective peaks gives the ratio of the respective elements in the product nanotube. The Ge and Si peak areas in the AlSiGe nanotubes are shown in Table 4-1, along with the Ge content of the nanotubes calculated from the areas of the fitted peaks.

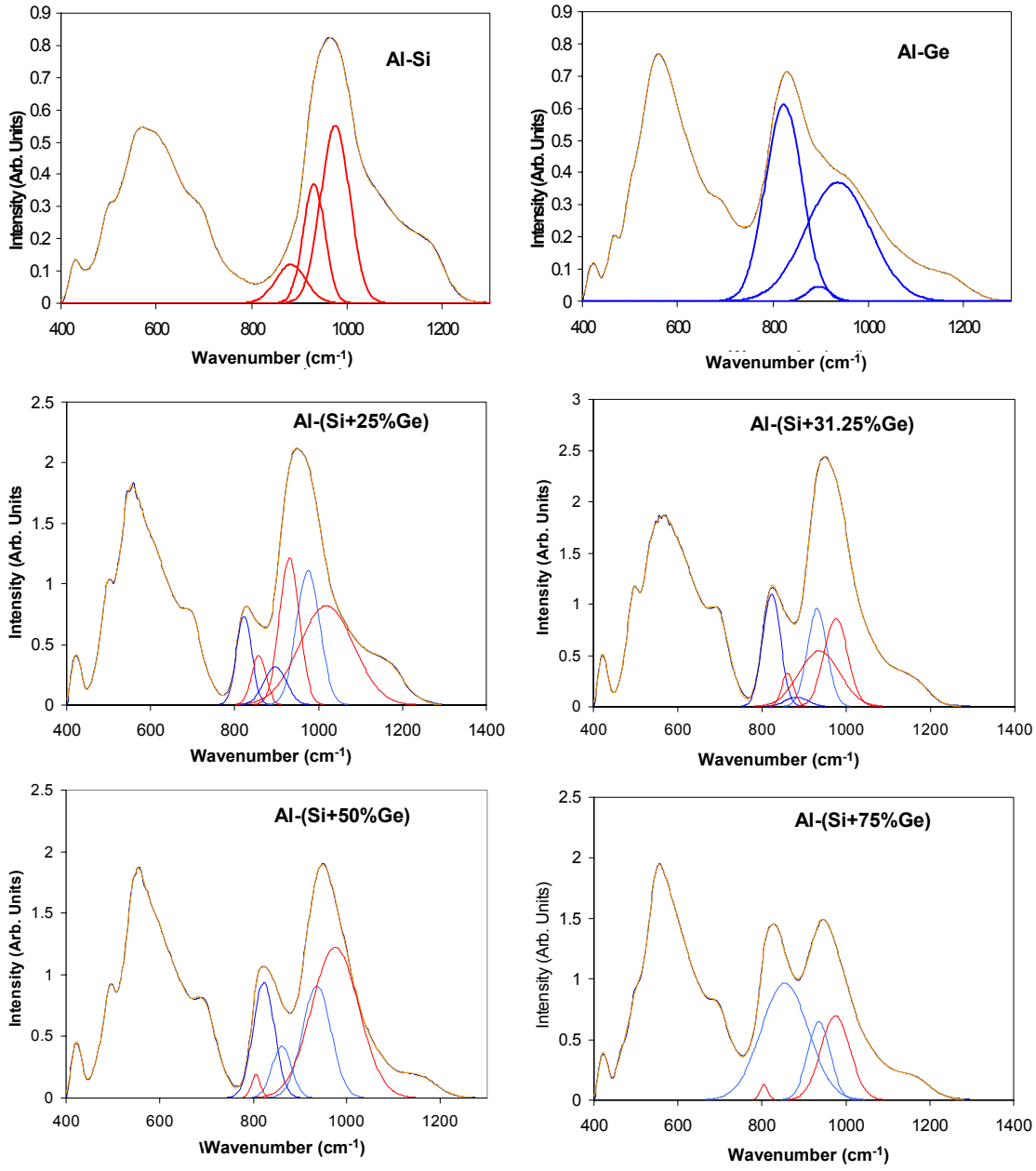

Figure 4-2: Deconvoluted FTIR spectra of mixed metal oxide nanotubes. The Gaussians indicated in red are vibrations involving Si-O bonds and blue are vibrations involving Ge-O bonds.

Table 4-1: Fitting results of FTIR spectra of mixed metal oxide nanotubes and composition calculations.

Experimental Ge content (%) : $\frac{Ge}{Ge+Si}\times 100$	**FTIR Analysis Results**		
	Total area from:		$\frac{Ge-O}{Ge-O+Si-O}\times 100$
	Si-O vibrations	**Ge-O vibrations**	
0.00	72	0	0.00
25.00	150	54	26.67
31.25	119	46	28.00
37.50	121	94	43.60
50.00	154	149	49.22
75.00	61	219	78.30
100.00	0	125	100.00

4.3.1.2 Results

The values obtained from FTIR compositional analysis, shown in Table 4-1 is plotted in Figure 4-3 along with the elemental composition given by XPS. The solid line corresponds to the composition line where the amount of Ge added is equal to the amount of Ge in the product nanotube (as obtained from analytical techniques). The error bars in the XPS data was obtained by performing the elemental analysis in 3 different sample areas.

It is clear from Figure 4-3 that the Ge content in the product nanotube follows the solid line (precursor composition) closely. Since the nanotube used for the analysis were purified using dialysis so that no amorphous synthesis products remains, the signal

coming from XPS and FTIR analysis are coming entirely from the nanotubes. This suggests that the Ge content in the product nanotube can be readily controlled.

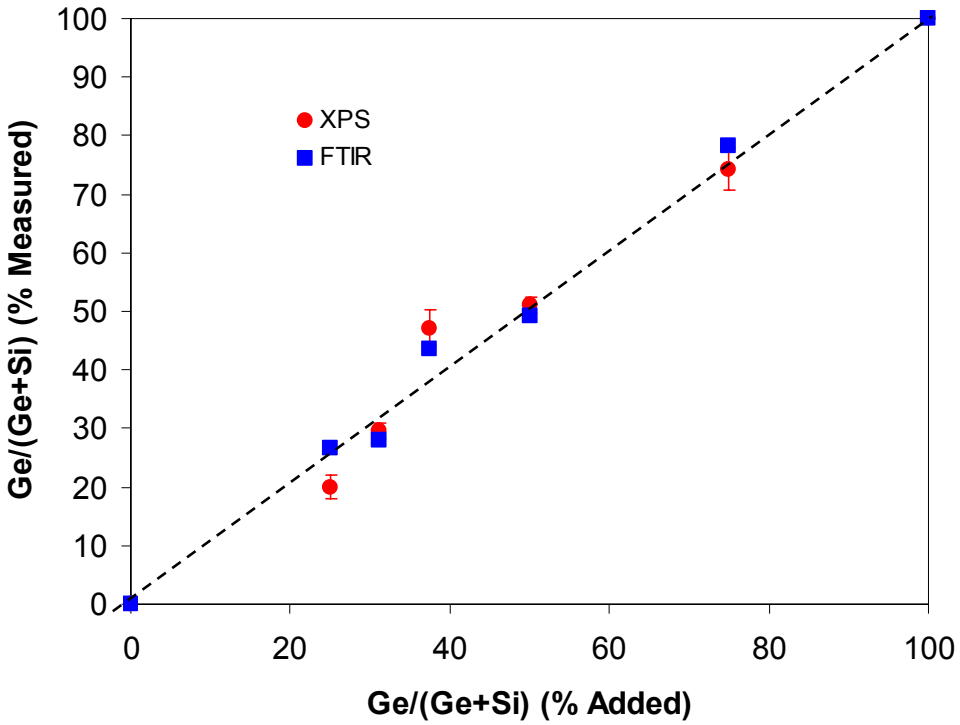

Figure 4-3: Comparison of the results of FTIR and XPS compositional analysis of the product nanotubes.

4.3.2 External Diameter of the Nanotubes

Recently, our group has reported that the monodisperse diameter of the AlSi nanotubes is a result of a unique strain energy minimum [114] in the material as a function of diameter. This energy minimum determines the external diameter of the AlSi nanotubes, particularly because the energetics governs the number of building units in the circumference (Figure 4-4). AlSi and AlGe nanotube has an external diameter of 2.1 nm

3.3 nm respectively. This increase in diameter can be explained partly by the observation that the Ge-O bond length of 0.175 nm is longer than the Si-O bond length (~0.16 nm). However, this does not fully explain why there are more building units in the circumference of the AlGe nanotubes than the AlSi nanotubes. To explain the phenomena of the increase in diameter, the strain energy minima model needs to be extended to AlGe nanotubes. More recent work in our group extends the theoretical calculations done on the AlSi nanotubes to the AlGe nanotube, and validates the model with the experimental data presented below.

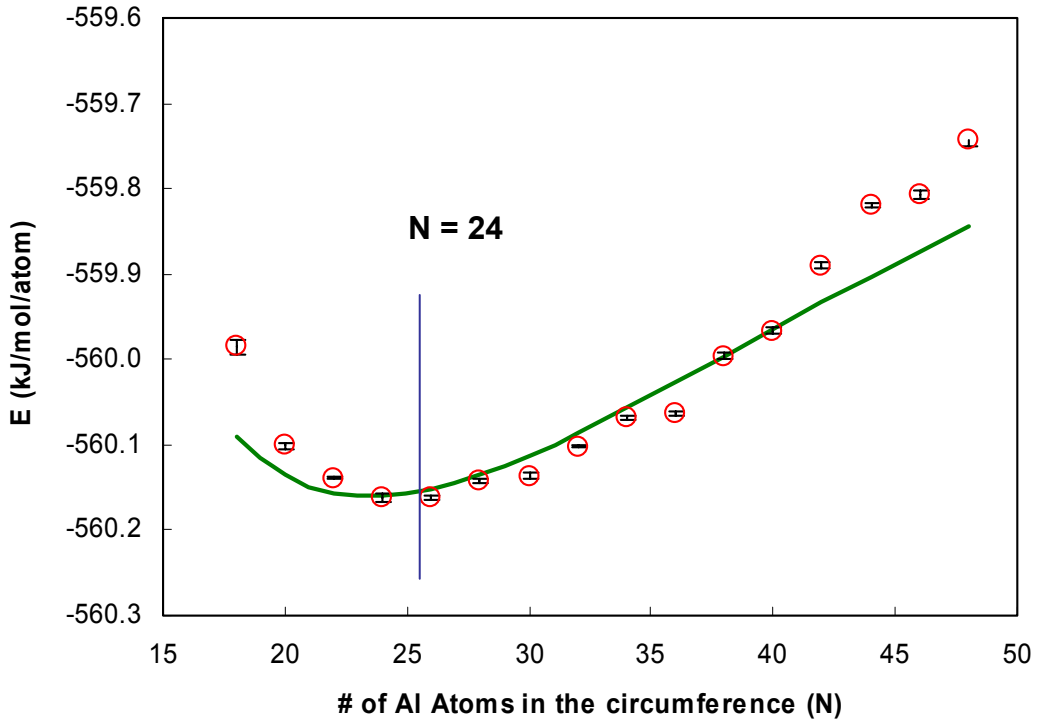

Figure 4-4: Strain energy of AlSi nanotubes as a function of building units [114].

We have shown in the previous section that the composition of the nanotubes (the ratio of Ge to Si) can be controlled accurately. Figure 4-5 shows the XRD spectra of the mixed metal oxide nanotubes and Ge content is indicated. Qualitatively the plot shows a visible shift towards lower 2θ values with the increase in Ge content, suggesting an increase in inter-tube spacing. The first intense peak corresponds to the (100) reflection, and we can calculate the inter-nanotube spacing by fitting the background subtracted XRD spectra with minimum number of Gaussians. This gives us an accurate estimate of the position of the first intense reflection, which is then used to calculate the inter-nanotube spacing.

Figure 4-6 shows the diameter of the mixed metal oxide nanotubes as a function of Ge content. It is clear that the external diameter of the nanotube is increasing with increase in Ge content. However, from TEM imaging it has been observed that with the increase in Ge content in the nanotubes, the length of the nanotubes also decreases, a fact that may lead to more irregular packing of the nanotubes. Qualitatively, this is also observed in the XRD spectra, wherein, with the increase of Ge content in the nanotubes the intensity of the first reflection significantly decreases coupled with peak broadening. In other words the closely packed model of the nanotubes is only semi-quantitative for short nanotubes with high Ge content.

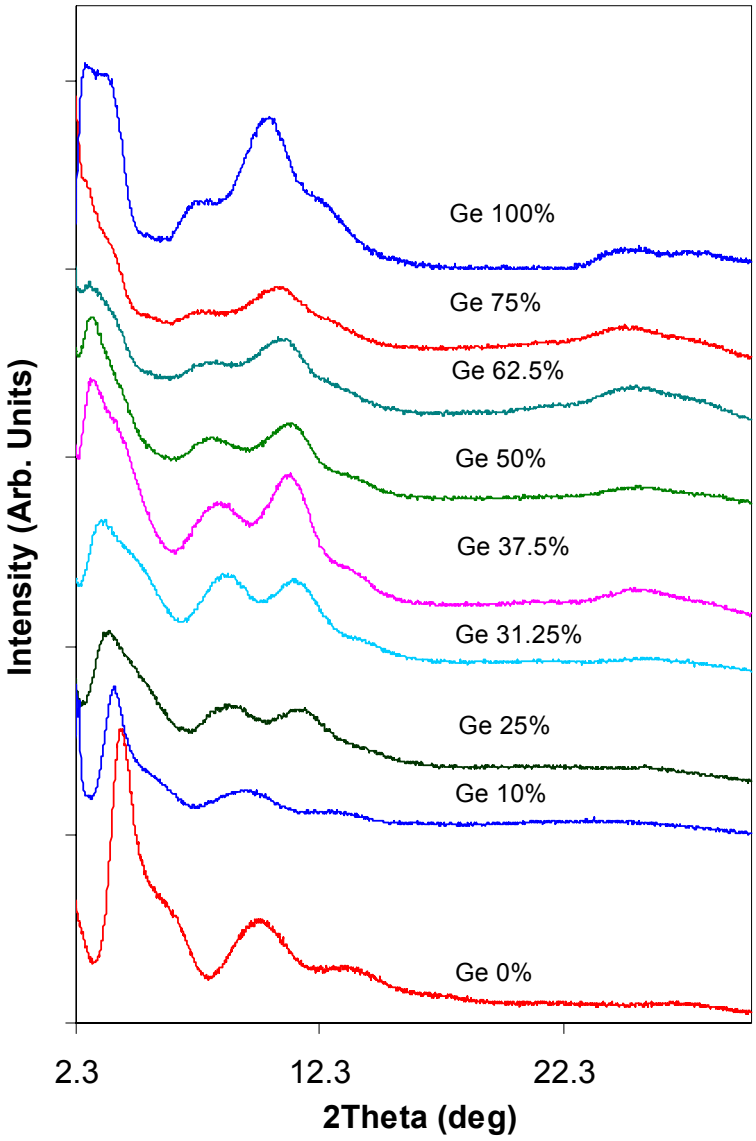

Figure 4-5: XRD spectra of mixed metal oxide nanotubes as function of Ge content.

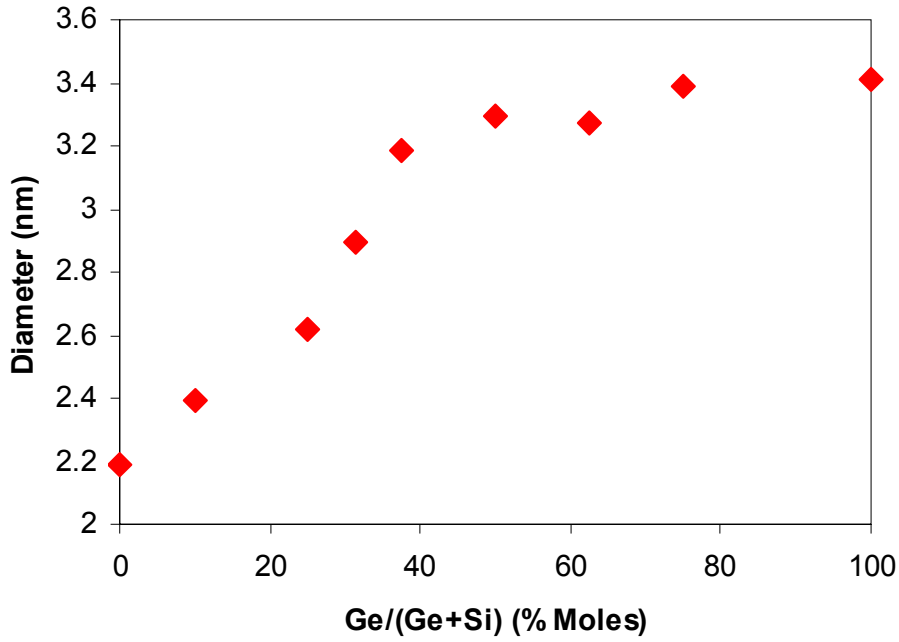

Figure 4-6: Diameter of mixed metal oxide nanotubes as a function of Ge content obtained from XRD analysis.

4.3.3 Length of Mixed Metal Oxide Nanotubes

Previously, it was observed by TEM imaging [80], that the length of the mixed metal oxide nanotubes decreases in length with the increase of Ge content. This is in agreement with the fact that the AlGe nanotubes are an order of magnitude shorter than its AlSi counterpart. Here we use DLS analysis to obtain a quantitative estimation of the length of the mixed metal oxide nanotubes. We recall that the Yamakawa rigid-rod model [100] used in our analysis is valid only for rods that have an aspect ratio (*L/d*) of greater than 20. Any nanotubes having aspect ratio less than 20 can be assumed to be a spherical particle with a diameter equal to the length of the nanotube. Figure 4-7 shows the length of the mixed metal oxide nanotubes as a function of Ge content. It shows the results of

the rigid rod and spherical approximation analysis. It is prudent to include both models in the plot since in this case the aspect ratio of the rods are not as clear as in the case of the pure AlGe and AlSi nanotubes. It is evident from Figure 4-7 that the nanotubes decreases in length with increase in Ge content and the rigid rod model converges with the spherical approximation at the 100% Ge content point. The reason for the decrease in nanotube length with increased Ge content is currently being investigated in our laboratory.

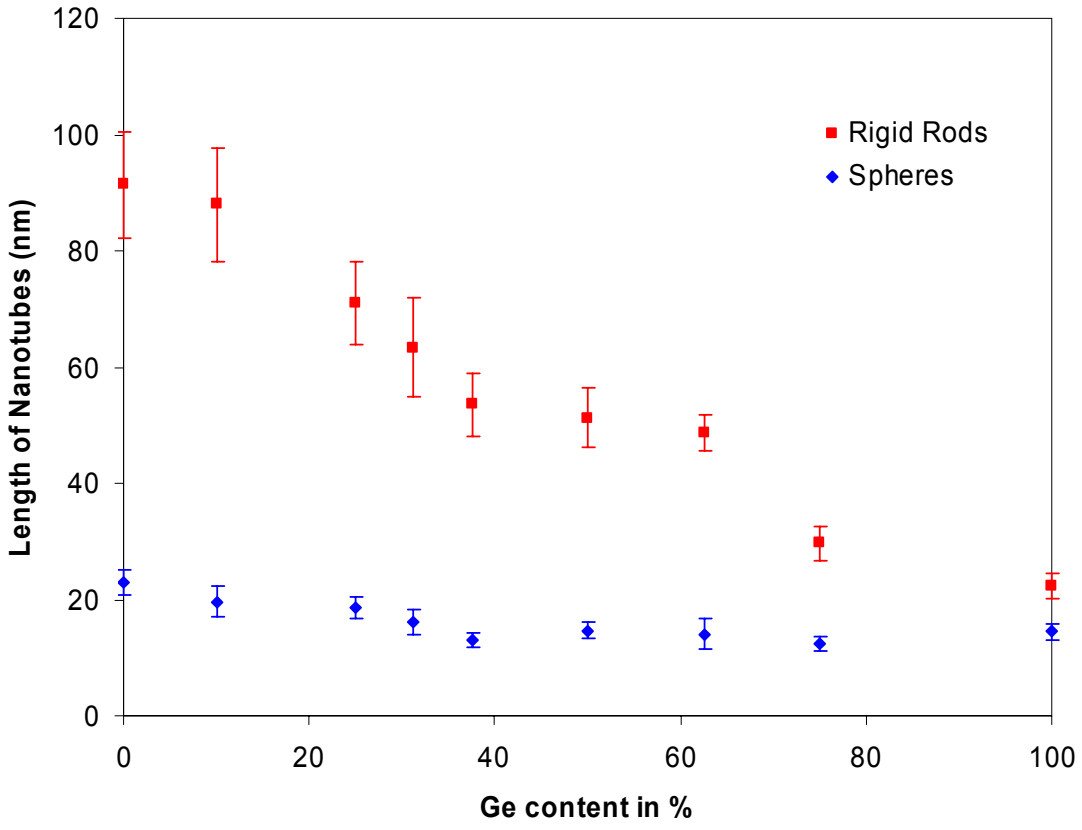

Figure 4-7: Length of nanotubes obtained from DLS analysis, both from rigid rod and spherical approximation models.

4.4 Conclusion

In parallel with our mechanistic investigation, we have demonstrated the capability of synthesizing and characterizing mixed metal oxide (AlSiGe) nanotubes wherein we can control the Si to Ge ratio in the product nanotube with analytical precision. Using FTIR and XPS analysis independently, it was shown that the actual composition of the product nanotubes coincides precisely to the composition added in the precursor solution. Furthermore, the dimensions of the AlSiGe nanotubes changes with composition. An increase in external diameter of the nanotubes with the increase in Ge content was observed by XRD analysis. DLS analysis, quantitatively established that the length of the nanotubes decreases with increase in Ge content. Thus, such precise changes of dimensions with composition is an important example of engineering of nanotubular objects with desired shape by controlling synthesis parameters.

Chapter 5 : Towards Generalization of the Mechanism of Formation of Single-Walled Mixed Metal Oxide Nanotubes

5.1 Introduction

As shown in the previous chapter, the dimensions of the present nanotube materials change with their composition. In a recently published work [114], our group reported the use of molecular dynamics simulations to show that there is a unique strain energy minimum that controls the diameter of the nanotubes. More recent work in our group (to be published separately) has verified the existence of the energy minimum for the mixed AlSiGe nanotubes and its correlation to the Ge content as shown by the experimental data of Chapter 5. Therefore, the control over the nanotube diameter is now well explained by our ongoing computational and theoretical efforts.

However, the above works do not address the question of why the length of the nanotubes is also a function of composition. If we assume that the kinetic model [136] derived for the AlGe nanotubes (Chapter 3) holds for the entire class of AlSiGe nanotubes, then we can investigate the changes in the quantitative model parameters resulting from higher Si content. Important questions are as follows: do the size and number of the amorphous nanoparticles change as a function of the Si content? Should the dynamic exchange between precursor solution and amorphous nanoparticles be considered non-equilibrium (i.e., can the amorphous nanoparticle accommodate a continuous influx of precursors even as it arranges into a nanotube? Is there a possible

role of aggregation processes that could change with Si content (due to changes in the surface charge and van der Waals properties) of the amorphous nanoparticles?

While the above questions require detailed consideration and possibly new types of experimental data (e.g., zeta potential measurements to determine surface properties), we present here preliminary results employing a similar "toolbox" of methods as used in Chapter 4. These results are presently inconclusive, but offer some qualitative insight and also suggest the required approaches for quantitative generalization of the mechanism. Specifically, we have used DLS and UV-Vis analysis to track the growth of AlSiGe nanotubes as a function of synthesis time. Three different compositions of AlSiGe nanotubes were investigated, namely 10%, 30% and 60% Ge content (with the remaining tetrahedral sites supplied by Si). As before, syntheses were run at four different temperatures and the data was collected over 300 h of synthesis.

5.2 Experimental Section

5.2.1 Synthesis

Depending on the desired content of Ge in the mixed metal oxide nanotubes, TetraEthylOrthoSilicate (TEOS – Si precursor) and TetraEthylOrthoGermanate (TEOG – Ge precursor) were added drop-wise to a stirred solution of 5 millimolar (mM) $AlCl_3$ solution until the Al:(Si+Ge) ratio was 1.8, and left to stand for 45 mins under vigorous stirring. Then a 0.1 N NaOH solution was added at the rate of 0.3 ml/min until the pH of

the solution reached 5.0. The pH was brought down immediately to 4.5 by drop-wise addition of a solution containing 0.1 M HCl and 0.2 M of acetic acid. The resulting clear solution was allowed to stir for 3 hrs and then reacted at 95ºC under reflux conditions for 300 h.

5.2.2 Characterization

For DLS and UV-Vis analyses, 5 mL samples were withdrawn from the reactor and filtered through a 0.2 μm pore size syringe filter to produce a dust-free sample containing only nanoparticles. DLS data were collected with a Wyatt DAWN EOS instrument. The scattering angle was 108º and the wavelength of the laser was 690 nm. The autocorrelator delay time (τ) was 1 μs. A series of 120 scans were performed on the sample, each with a 1-second acquisition time. UV-Vis data was obtained on a HP 8453 UV-Vis spectrophotometer. A quartz cuvette was used as a sample holder since it is optically transparent to UV radiation.

5.3 Results and Discussion

In this section we present the experimental data obtained for the growth of AlSiGe nanotubes, and investigate their formation and growth phenomena in the framework of the kinetic model presented in Chapter 3 for the AlGe nanotubes. The mathematical expressions, together with the procedure for obtaining the kinetic

parameters by fitting the experimental data, are elaborated in Chapter 3 and cross-referenced in this section.

Figure 5-1 to Figure 5-3 show the concentration of AlSiGe nanotubes with varying Ge content (10%, 30% and 60% Ge) as a function of synthesis time for four separate synthesis temperatures of 95°C, 85°C, 75°C and 65°C, as obtained by UV-Vis spectroscopy. The solid lines in Figure 5-1 to Figure 5-3 correspond to the least square fits to the kinetic model. The kinetic parameter *K*, obtained from the fits at different temperatures and composition are shown in Table 5-1. The kinetic parameters for the pure AlGe nanotubes are given in the table for comparison. The kinetic parameter and its significance will be discussed later in this section.

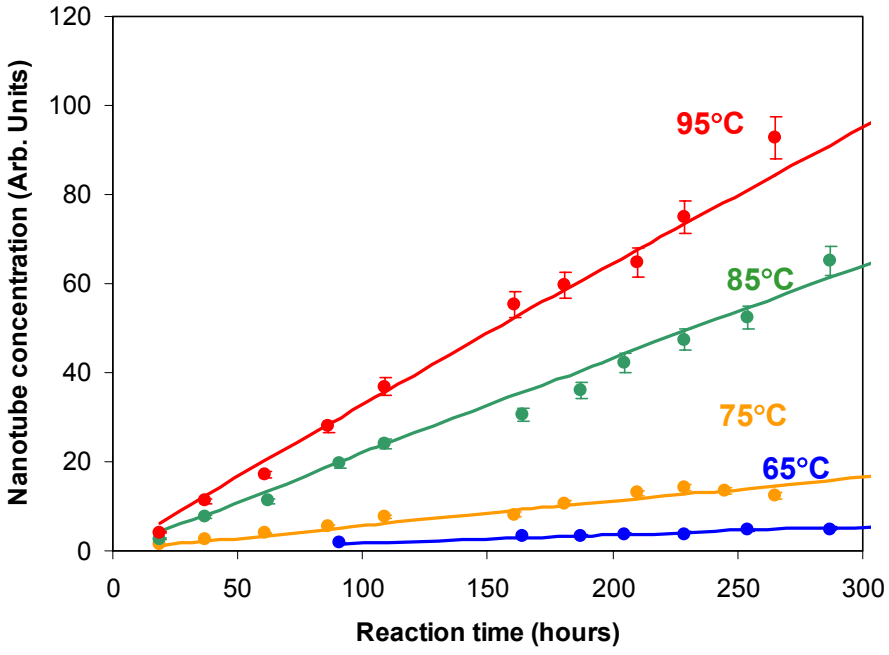

Figure 5-1: Concentration of AlSiGe nanotubes with 10% Ge content from UV-Vis absorption analysis, as a function of synthesis time and temperature.

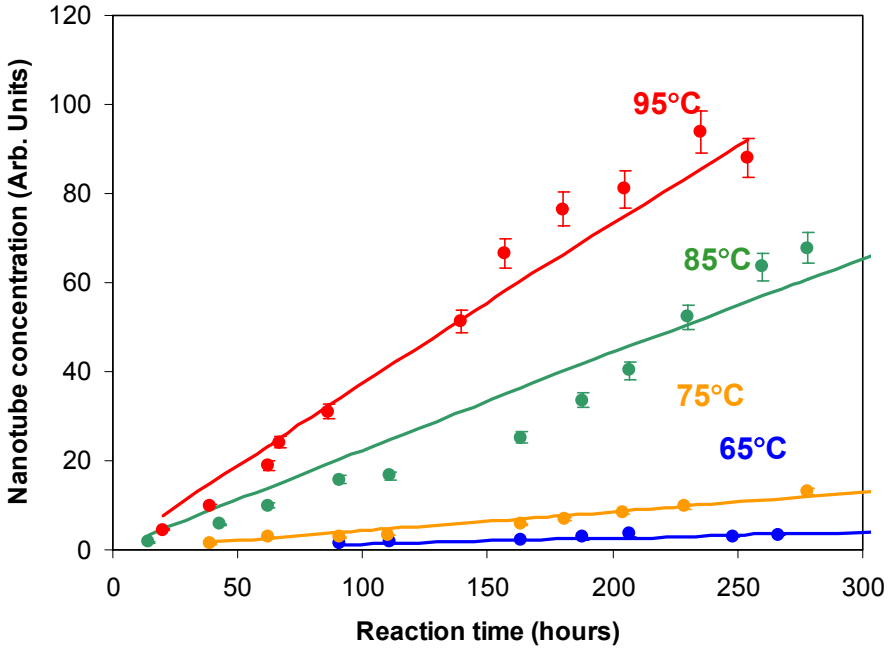

Figure 5-2: Concentration of AlSiGe nanotubes with 30% Ge content from UV-Vis analysis, as a function of synthesis time and temperature.

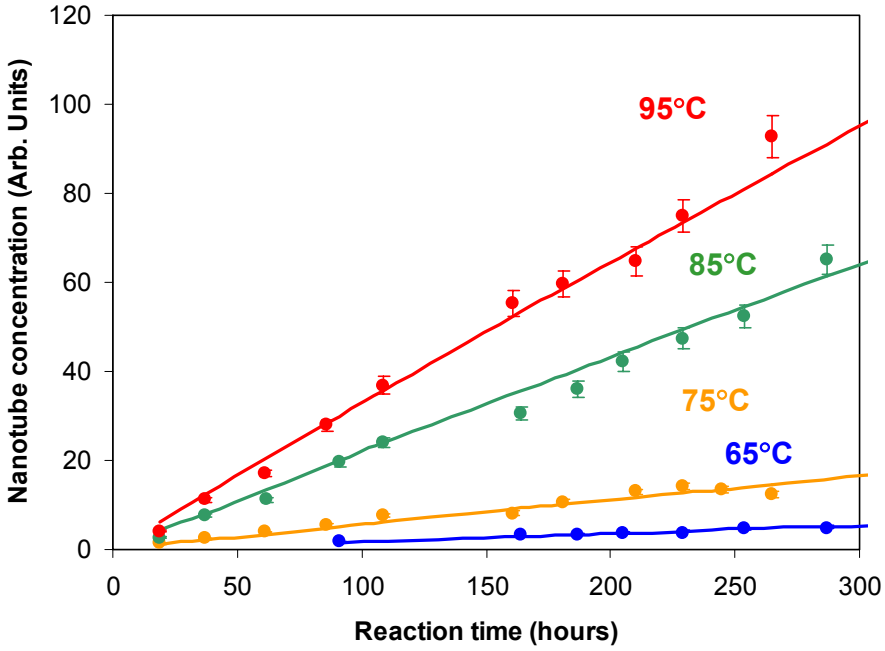

Figure 5-3: Concentration of AlSiGe nanotubes with 60% Ge content from UV-Vis analysis, as a function of synthesis time and temperature.

Table 5-1: Kinetic parameter *K*, at different nanotube compositions and temperatures obtained from fitting the concentration plots.

% Ge $\frac{Ge}{Ge+Si}\times 100$	***K*** **(h^{-1}) at different Synthesis Temperatures**			
	65°C	**75°C**	**85°C**	**95°C**
10%	1.92×10^{-4}	3.01×10^{-4}	1.63×10^{-3}	5.73×10^{-2}
30%	1.52×10^{-5}	5.01×10^{-5}	2.62×10^{-4}	4.42×10^{-4}
60%	2.08×10^{-5}	6.46×10^{-5}	2.56×10^{-4}	3.88×10^{-4}
100%	2.87×10^{-5}	4.39×10^{-4}	2.05×10^{-3}	5.78×10^{-3}

Figure 5-4 to Figure 5-6 show the average size of nanoparticles (nanotubes and amorphous nanoparticles) from DLS analysis as a function of synthesis time and temperatures for different AlSiGe nanotube compositions. Here the average nanoparticle size has been calculated from the DLS autocorrelation function by using the rigid rod model as explained in Chapter 1. From qualitative TEM [80] and quantitative DLS analysis (Figure 4-7), we know that the lengths of the AlSiGe nanotubes are longer than that of pure AlGe nanotubes. Recall that the rigid rod model is valid only for nanotubes with $L/d \geq 20$ and the spherical approximation is valid for nanotubes with $L/d \leq 5$. With significant Si content in the nanotubes, the spherical approximation does not hold. For example, for a nanotube with 20% Si content the length, L = 40 nm (Figure 4-7) and the diameter, d = 3.2 nm (Figure 4-6). Therefore, L/d = 12.5, and hence the spherical approximation does not hold. Finally, note that reproducible DLS data could not be obtained beyond approximately 100 hours of synthesis time for the reaction at 95°C in Figure 5-4. Since the Ge content is low, longer nanotubes are formed and eventually lead to difficulties in filtering the samples.

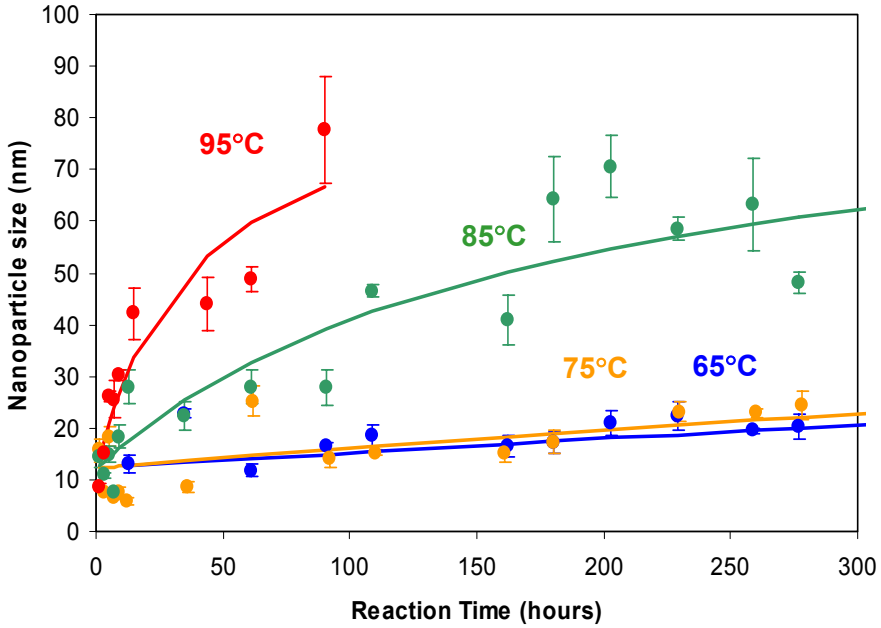

Figure 5-4: Average nanoparticle size obtained from DLS analysis and the corresponding fits for AlSiGe nanotubes with 10% Ge.

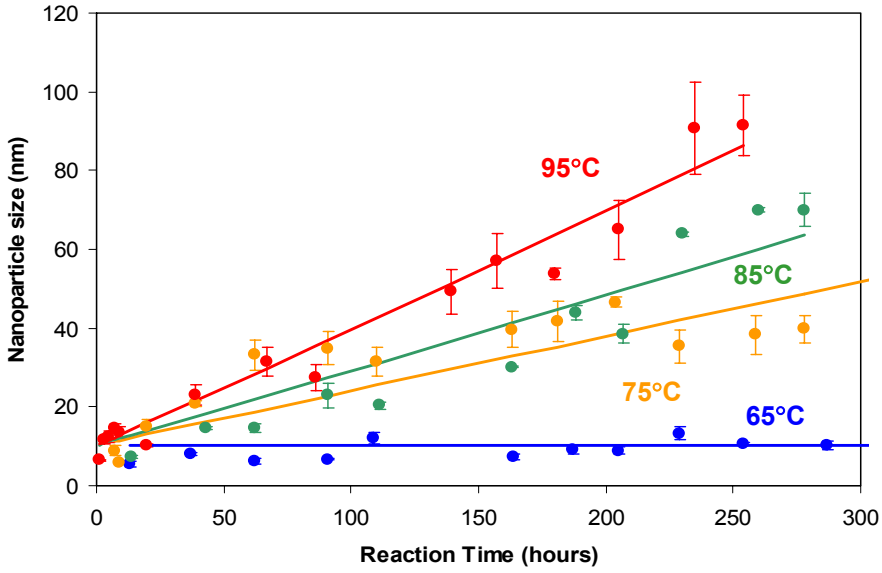

Figure 5-5: Average nanoparticle size obtained from DLS analysis and the corresponding fits for AlSiGe nanotubes with 30% Ge.

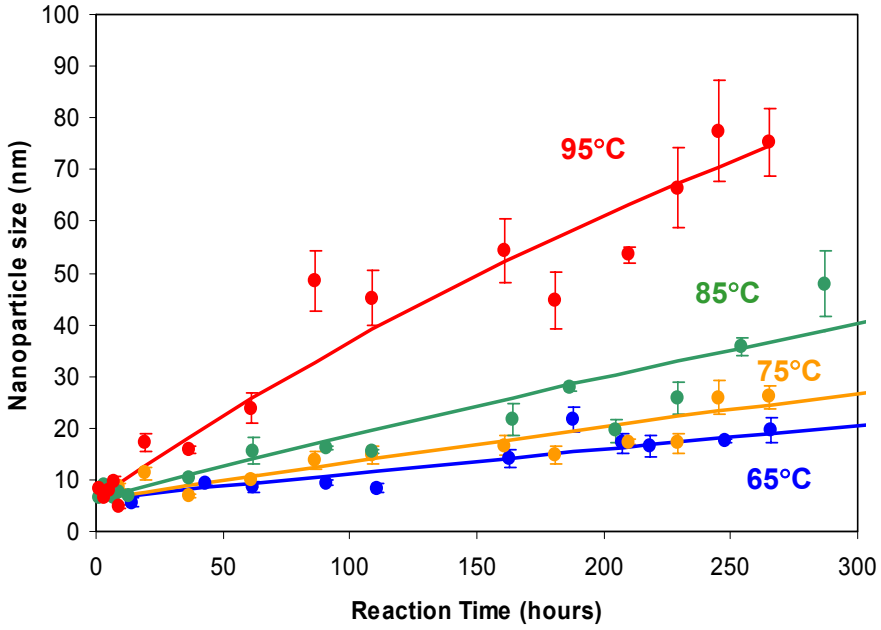

Figure 5-6: Average nanoparticle size obtained from DLS analysis and the corresponding fits for AlSiGe nanotubes with 60% Ge.

Table 5-2: Kinetic parameters k_2, diameter of ANPs (L_A) and length of nanotube (L_N) at different nanotube compositions and temperatures obtained from fitting the nanoparticle size DLS plots.

$\frac{Ge}{Ge+Si}\times 100$ % Ge	k_2 (h^{-1}) at different synthesis temperatures				L_A (nm)	L_N (nm)
	65°C	75°C	85°C	95°C		
10%	3.94×10^{-4}	5.16×10^{-4}	5.69×10^{-3}	2.50×10^{-2}	12	91
30%	3.99×10^{-8}	2.77×10^{-5}	3.75×10^{-5}	5.76×10^{-5}	10	4998
60%	2.09×10^{-4}	3.05×10^{-4}	5.25×10^{-4}	1.41×10^{-3}	6	248
100%	4.15×10^{-4}	1.11×10^{-3}	4.29×10^{-3}	9.16×10^{-3}	6	18

The solid lines in Figure 5-4 to Figure 5-6 are the model fits from which the kinetic parameters tabulated in Table 5-2 are obtained. The fitted nanotube lengths and kinetic parameters for the 30% Ge and 60% Ge syntheses do not appear to be physically realistic. We believe that this is primarily due to the high sensitivity of the DLS analysis

to the aspect ratio of the nanotubes. As explained in the previous paragraph, the spherical approximation does not hold for nanotubes with less than 80% Ge content, and the rigid rod model does not hold for nanotubes with more than 20% Ge content. The AlSiGe nanotubes with 30% and 60% Ge content lie in the intermediate range, where neither model is valid. This problem is compounded by the fact that the presence of the spherical ANPs also alters the DLS diffusivity substantially due to an averaging effect. A detailed discussion of this effect is given in the next paragraph. However, the length of nanotubes and diameter of the ANPs obtained by the fit for the AlSiGe nanotubes with 10% Ge show reasonable values (Table 5-2). An important finding is that the size of the initial AlSi ANP is more than twice the size of the ANP formed in the AlGe nanotube synthesis. Thus, more precursors are packed in the nanoparticle, leading to the formation of much longer nanotubes (~ 91 nm) as explained later in this chapter.

The diffusivity obtained from the DLS autocorrelation function is the concentration weighted average of the diffusivities of rods (nanotubes) and spheres (ANPs). Restating Equation 3.12 expressed in Chapter 3:

$$\overline{L}_{DLS} = \frac{L_A C_A + L_N C_N}{C_A + C_N} \tag{3.12}$$

At high Ge content (very short rods, spherical approximation is valid), this equation remains valid because L_A and L_N are comparable. At low Ge content, $L_N >> L_A$, and Equation 3.12 essentially transforms to $\overline{L}_{DLS} \sim L_N$, and thus still remains useful. For the

nanotubes with intermediate Ge content, neither is the diffusivity a linear function of length (spherical approximation invalid), nor is the length sufficiently large to mask the contribution from the ANPs. Thus, Equation 3.12 does not correctly express the length of the AlSiGe nanotubes with intermediate Ge content (20% < Ge < 80%). For such cases, a DLS analysis needs to be developed wherein the diffusivities of ANPs and the nanotubes are separately identified from the autocorrelation function itself.

Figure 5-7 shows the Arrhenius plots for the AlSiGe nanotubes with different Ge content. The activation energies obtained from the slopes of the plots are given in Table 5-3. In accordance with our discussion regarding the DLS analysis of AlSiGe nanotubes with 30% and 60% Ge content, the preliminary value of activation energy obtained for k_2 is considered unrealistic and is being reported for the sake of completeness. Table 5-3 shows that the activation energy $E_a(k_2)$ for the formation of AlSiGe nanotubes with 10% Ge, differs substantially from the pure AlGe (i.e. 100% Ge) case. However, this inference is inconclusive and has been drawn from just two nanotube syntheses (10% Ge and 100% Ge). For validation of this result, more detailed experimental studies are required and are underway, specifically measurements on AlSiGe nanotubes with 20%, 80% and 90% Ge. These materials can be described adequately with the current DLS analysis method.

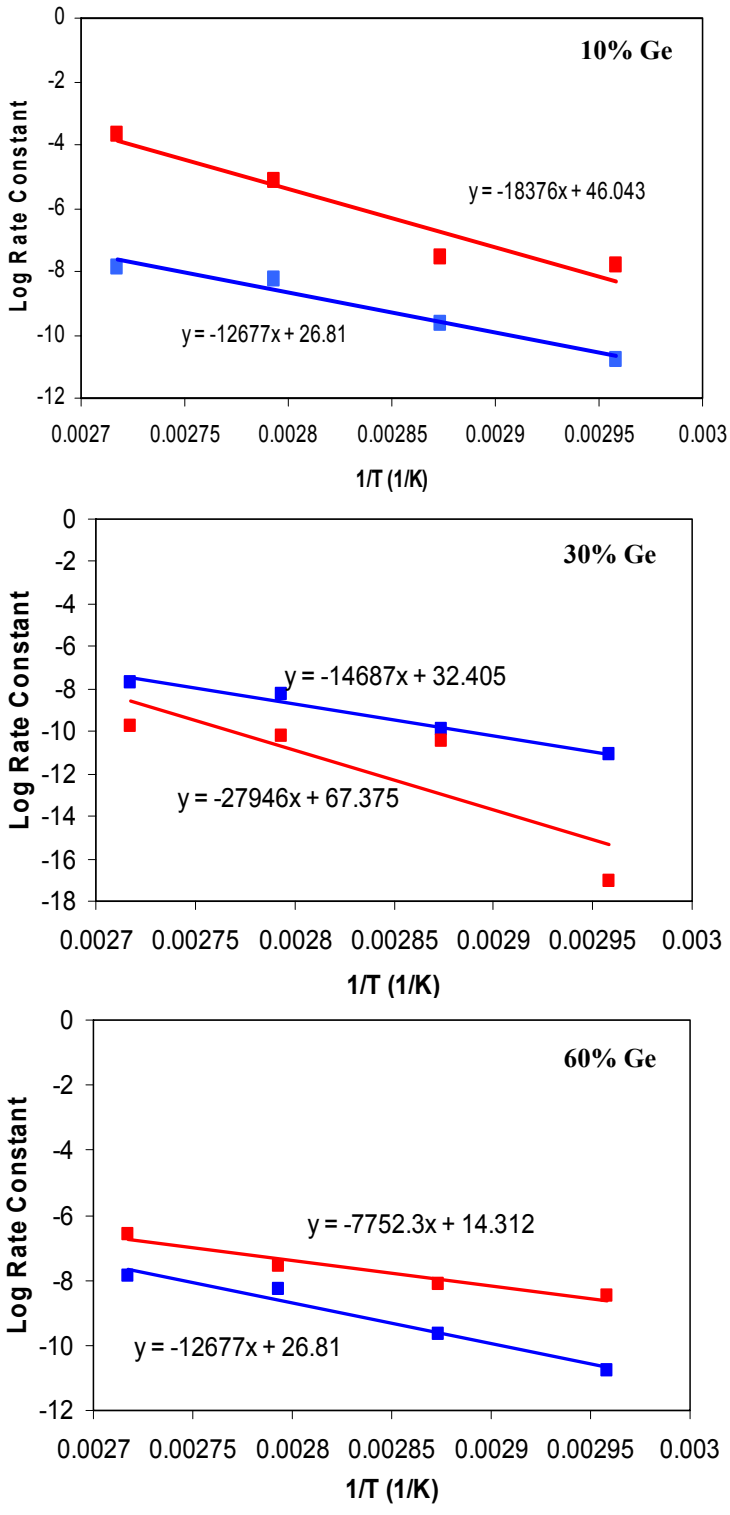

Figure 5-7: Arrhenius plots for AlSiGe nanotubes with indicated Ge content. The activation energies are obtained from the slope of the plots. The red and blue points correspond to rate constants K and k_2.

Table 5-3: Activation energy from the Arrhenius plots shown in Figure 5-7.

% Ge $\frac{Ge}{Ge+Si}\times 100$	Activation Energy E_a (kJ/mole)	
	$E_a(K)$	$E_a(k_2)$
10%	123	153
30%	122	99
60%	105	95
100%	181	110

In the above discussion based on the DLS and UV-Vis analyses, we have assumed that the "first-pass" kinetic model of Chapter 4 holds quantitatively without any refinements. On fitting the experimental data with the model, and excluding the 30% and 60% Ge data for reasons explained above, we have some reason to believe that the longer length of nanotubes at higher Si content may indeed be the result of the formation of larger ANPs. The fitted size of ANPs formed in the 10% Ge synthesis is 12 nm, which evolves into nanotubes of 91 nm. The fitted size of ANPs formed during the synthesis of (18 nm long) AlGe nanotubes is 6 nm. If we assume that the packing density of Al species in the ANPs is almost constant, we can then estimate the required size of ANP from the length of the nanotube finally formed. We know that for the AlGe nanotubes we have 72 Al atoms per unit cell (0.84 nm) of the nanotube. Therefore, the number of Al atoms in the 17.60 nm AlGe nanotube is; $(72/0.84)\times 18 = 1509$. This is the number of Al atoms in a single ANP of size 6 nm. Therefore, the Al packing density is $1509/\left[(4/3)\pi(6/2)^3\right] = 14$ Al atoms/nm^3. The length of the AlSiGe nanotube with 10% Ge is 91 nm, and therefore the total number of Al atoms; $(72/0.84)\times 91 = 7755$. If the packing density of Al remains the same, i.e. 14 Al atoms/nm^3, then we have $7755/\left[(4/3)\pi(L_A/2)^3\right] = 14$, yielding L_A = 11 nm. This estimate is close to the fitted size of the ANP, i.e. 12 nm. It is to be noted that the number of Al atoms in a unit cell of the

nanotube differs considerably with composition because of the different diameters of each material. For example, AlGe and AlSi nanotubes have 72 and 48 Al atoms per unit cell respectively.

5.4 Conclusions

In this Chapter, we have described preliminary progress in quantitatively generalizing the mechanistic model of AlGe nanotube formation developed in Chapter 3 to the larger class of AlSiGe nanotubes. Our initial results seem to provide clues to understand why the nanotube length changes with composition. The size of the nanotube is dependent on the amount of precursors condensed in the ANP, which in turn depends on the size of the ANP. Our experiments indicate that for AlSiGe nanotube with 10% Ge content, the size of ANP is 12 nm, which is more than twice the size of ANPs formed during the AlGe nanotube synthesis (6 nm). With a simple calculation, we have estimated that the diameter of ANP required to pack enough precursor material to make a 91 nm nanotube is 11 nm, which is close to the value obtained from the experiments. However, no further definite statements can be made regarding the data, since it has been found that the present DLS analysis method is invalid for the AlSiGe nanotubes with 30% and 60% Ge content. We are presently carrying out further experiments to investigate materials that are closer to the two ends of the AlSiGe nanotube spectrum i.e. with Ge content less than 20% or greater than 80%. A modified DLS analysis would be required to analyze the experimental data from intermediate compositions. At the same time, more detailed models that account for any possible aggregation processes (supported by the necessary

surface property data) as well as refinements to account for the non-equilibrium nature of the ANP formation process, will allow generalization of the mechanism to allow a more robust framework for future nanotube engineering research.

Chapter 6 : Conclusions and Recommendations for Future Work

6.1 Summary of Present Work

Nanotubes are important 'building block' materials for nanotechnology, but a synthesis process for short (sub-100-nm) solid-state nanotubes with structural order and monodisperse diameter has remained elusive. To achieve this goal, it is critical to possess a definitive mechanistic framework for control over nanotube dimensions and structure. In this thesis, we have elaborated the essential aspects of a comprehensive mechanistic framework that may allow the engineering of precisely tunable nanotube objects. Firstly, the phenomenological study of growth of AlSi and AlGe nanotubes gave new insight into the effect of synthesis time on the growth of the nanotubes, and showed unusual behavior that could not be explained with existing nanotube growth models. The ensuing mechanistic investigation on AlGe nanotubes provided a clear explanation of the phenomenological observations, and led to the conclusion that amorphous nanoparticles are a key intermediate in the nanotube synthesis. The mechanism could be described with a simple mathematical model. In a parallel study, we successfully demonstrated compositional and dimensional control of mixed metal oxide (AlSiGe) nanotubes, and provided critical experimental input to validate computational and theoretical research by other group members on nanotube diameter control. Finally, we took substantial steps towards generalizing the quantitative kinetic model to encompass a larger class of mixed metal oxide nanotubes.

In our view, the present work has established a conceptual framework as well as reliable experimental procedures to allow pursuit of an important goal in nanoscale chemical processing, viz. the engineering of oxide nanotube materials with controlled composition, structure, and dimensions. Success in this endeavor will allow us to incorporate the vast range of technologically relevant properties of oxide materials into nanotube objects. The number of applications that can be envisioned for metal oxide nanotube materials is very large, especially in context of rapid improvements in methods for integrating nanoparticle components into functioning devices. In the concluding sections of this thesis, some future directions of particular interest (separate from the ongoing mechanistic studies) are outlined, in which successful results would be also considered as significant advances in nanoscale science and engineering.

6.2 Future Directions in Nanotube Engineering

6.2.1 Nanotube Functionalization

Imogolite nanotubes have been investigated for use as a catalyst support [29, 137] and for methane storage [138]. However, based on the unique properties of these nanotubes, one may envision many other potential applications. For example, the AlGe nanotubes, which are as short as 18 nm and with an outside diameter of 3.3 nm, are attractive candidates for use in artificial ion channel devices due to their well-defined solid-state structure, hydrophilic interior and short length. Artificial ion channels have high potential as novel biomolecule sensing devices, particularly for high speed DNA and

protein analysis [17]. These devices operate by detecting chain biopolymers as they translocate through a nanoscale ion-conducting channel. The variation in the ion conductance of the channel, when correlated to the biopolymer properties, can lead to novel sensing strategies with single-molecule resolution and high speed. Intrinsic limitations on the stability and reliability of nanoscale ion channels made from 'soft matter' such as proteins, have led to a requirement for solid-state hydrophilic ion channels of appropriate length and diameter [139]. Similarly, others have proposed the construction of nanocomponents such as nanoelectrical cables (containing a conducting polymer wire with an insulating nanotube sheath) by threading of polymers into short nanotubes. A number of recent simulation studies [140-142] using carbon nanotube models (< 5 nm in length) have suggested the potential for the above applications.

To realize these potential applications, it is critical to develop the ability to control the functionality of the internal and external nanotube surfaces. For example, the external surface of the nanotube should be hydrophobic for incorporation as an artificial ion channel in a lipid bilayer membrane. This is to ensure that it has favorable interactions with the aliphatic lipid tail so that it anchors strongly in the bilayer. On the other hand, for nanoelectrical cables, the internal surfaces should be hydrophobic to ensure favorable polymer-nanopore interactions. The aluminosilicate/aluminogermanate nanotubes offer a unique advantage in that their external and internal surfaces are chemically different (aluminum hydroxide and silanol/germanol respectively).

6.2.1.1 Nanopore Functionalization

The present nanotubes could be functionalized with organic functional groups, both on the interior as well as exterior surfaces. In situ functionalization could be carried out by replaced by a functional group attached to the silicon/germanium atom, i.e. ≡Si-OH will be replaced by ≡Si-X for AlSi nanotubes.

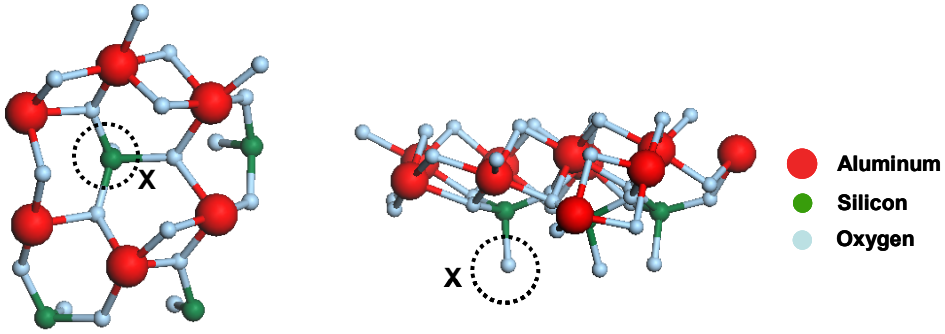

Figure 6-1: 6-membered aluminum hydroxide ring with pendent silinol/germanol groups comprising the SBU of the nanotubes. A side view of the SBU showing the position of the functional group (X) attached to the silicon/germanium atom.

A Structural Building Unit (SBU) of the nanotube is the six membered ring of aluminum hydroxide with a silanol/germanol pendant (Figure 6-1). The group marked X in the Figure refers to the organic functional group. X can be chosen for any desired property of the nanotube pore. In a regular AlSi nanotube synthesis, the silicon precursor TetraEthylOrthoSilicate (TEOS) is hydrolyzed in mildly acidic conditions to yield $Si(OH)_4$. Three of the four hydroxide groups in the silicate tetrahedron react with the aluminum hydroxide sheets by an oxo bridge to form the nanotube wall [74, 76, 89, 120]. The fourth hydroxide group is pendant in the nanotube. If TEOS is replaced by any of the chemical species shown in Figure 6-2, wherein the Si-X (X = methyl, methoxy,

ethylammonium, ethoxy) bond is stable in acidic pH, the resulting nanotube would have a pendant X group in the nanopore, leading to functionalized nanotubes.

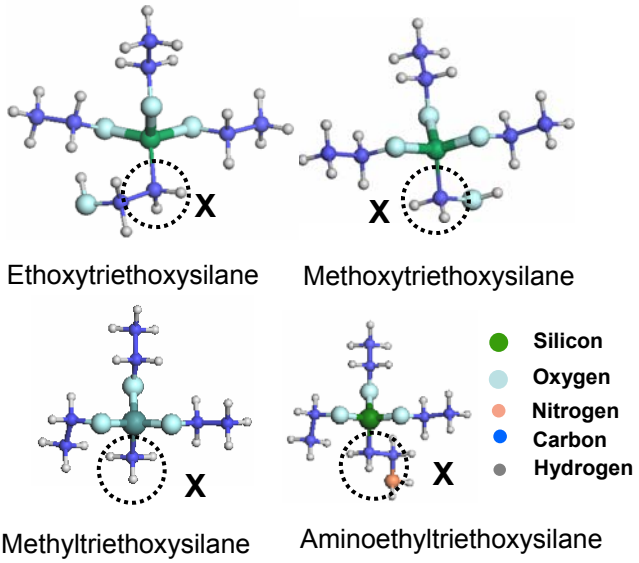

Figure 6-2: Silicate precursors with one of the valences occupied by a non-hydrolyzable Si-C bond where a functional group (X) is attached to the Si atom.

Systematic synthesis experiments could be performed with varying ratios of silicate precursors (TEOS and functionalized silicate precursors) keeping all the other synthesis steps unchanged. The formation of nanotubes can be confirmed by XRD, TEM and ED analysis. The pore size of the functionalized nanotubes can be measured with nitrogen adsorption. Fourier Transform Infra-Red (FTIR), Raman, and solid state ^{29}Si and ^{13}C MAS NMR spectroscopy can be used to ascertain whether the functional groups are attached to the Si groups in the interior of the nanotubes. However, some issues regarding the compatibility of the organosilane precursors in an aqueous environment need to be addressed. Some of the silicate precursors have hydrophobic groups (methyl, ethyl) attached to the silicon. Since the nanotube synthesis is in aqueous solution, the

hydrophobic silicate precursors might aggregate and condense with each other rather than being incorporated in the nanotube. This problem can be dealt with by diluting the functionalized silicate precursors with TEOS, keeping Al to Si atomic ratio constant. Since TEOS is hydrolyzable with the product having no hydrophobic groups, this may prevent the partially hydrolyzed functionalized silicate precursors from clustering and condensing. Another approach could involve selection of more hydrophilic (e.g., hydroxymethyl or aminomethyl) functional groups. In mildly acidic conditions, hydrolysis of ethoxysilicate bond (Si-OC_2H_5) is slow [82] and furthermore, the presence of organic functional groups in any of the valences of silicon decreases the rate of hydrolysis of the silicate precursors [83, 143, 144]. This problem could be addressed by choosing compounds like functionalized chlorosilanes, e.g. $(Cl)_3SiCH_2Cl$ (methylchloridetrichlorosilane), which are reported to be much more easily hydrolyzable than alkoxysilanes [82].

6.2.1.2 Transition Metal Oxide Nanotubes

Like aluminum, many other metals (e.g., Mg, Ga, In, Fe, Cr, Cu) are known to form layered oxides and hydroxides. Thus, it is natural to attempt the synthesis of nanotubes with transition elements in the outer wall, whether by themselves or in combination with aluminum. This modification could drastically alter the nanotube properties (optical, magnetic, etc).

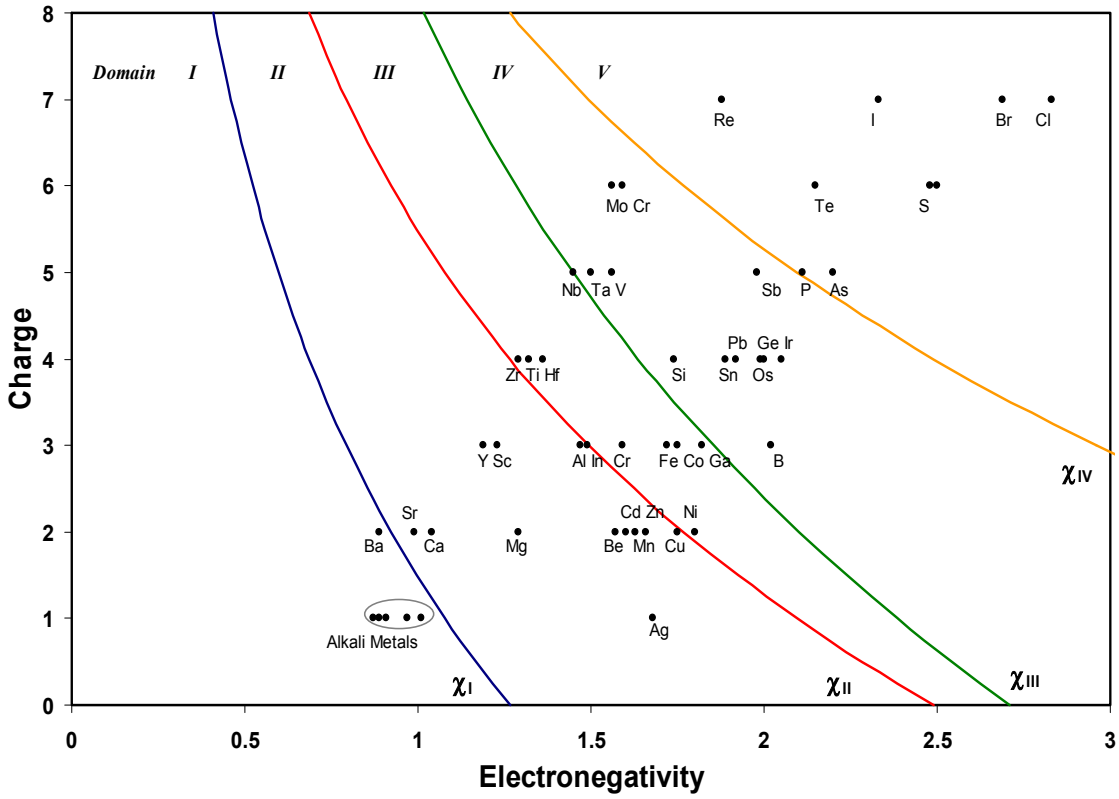

Figure 6-3: Charge versus electronegativity diagram of elements.

Suitable elements for substitution of Al are the trivalent elements which are close to Al in the charge-electronegativity diagram shown in Figure 6-3. Elements like Ga, In, Sc, and Fe are known to octahedrally coordinate with oxygen to form hydroxides and oxyhydroxides of layered structure [145], which is an important attribute as shown by our mechanistic investigation. Also we know from our mechanistic work that formation of the M-O-Si bridges(M represents the octahedrally coordinated metal) must occur very early in the reaction for a successful nanotube synthesis. Thus, careful control of pH and hydrolysis/condensation rates as well as monitoring of the reaction with techniques discussed in this thesis, are likely to be critical components in exploring metal substitution reactions.

Substitution elements can also be introduced in the synthesis as precursors in dilute mixture with Al. Typically 1% to 10% molar ratio of X (X/(Al+X)×100) where X = Ga, In, Sc or Fe can be administered with the Si precursor. After separation and dialysis, solid state characterization analysis can be conducted. XRD, TEM and ED analysis can show whether nanotubes was formed in the synthesis and correspondingly XPS analysis can indicate the composition of the products. This combination can fully characterize the substitution products.

The interaction of Al with the substitution metal must be ensured for a successful synthesis. To such an end the concentration plays a major role. The substituting element should not be too concentrated to interfere with Al in the process of forming the Al-O-Si bridges that lead to the formation of the nanotubes, and, should not be too dilute to get inadequate signal from analytical characterization tool (XPS). Through careful experimentation this optimum concentration can be found.

6.2.2 Electronic and Optical Properties of Aluminosilicate/germanate Nanotubes

The relationship between structure and electronic properties of nanoscale materials is of high importance particularly in field of electronics and optics [59, 131]. Semiconducting materials have been known to change electronic structure quite drastically with shape and size primarily due to electron confinement effects[115, 146]. Nanoparticles with cylindrical geometry have an inherent advantage in comparison with

spherical nanoparticles, because they have two controllable dimensions [115, 132, 146]. Optical activity of materials is characterized by optical absorption at certain wavelengths, and by optical emission at particular wavelengths through processes such as photoluminescence (PL). Photoluminescence is a process in which a material absorbs a photon, thus transitioning to a higher electronic energy state, and then radiates one or more photons to return to the ground state. Although there are many types of PL (due to different pathways a electron can take to come back to ground state), the type of PL of interest to us is fluorescence, wherein the emitted photon is of a longer wavelength than the absorbed one.

Aluminosilcate/germanate nanotubes shows a strong absorption in the UV/near-visible range at 320 nm, which also shifts with composition (Figure 6-4). From the leading edge of the absorption peak, the band gap of the nanotubes is calculated to be 3.6 eV (GaN, used in semiconductor lasers, has a band-gap of 3.4 eV at 0 K [147]). Previous work on boehmite (layered AlOOH, Figure 3-2) powders showed strong PL activity with emission in the blue region [148]. The reason behind this property is controversial [149], and several authors have proposed that the primary reason for such optical activity in ceramic materials is due to internal defects and hydroxyl groups (e.g., Al-OH, Si-OH, Ti-OH) in the materials [150].

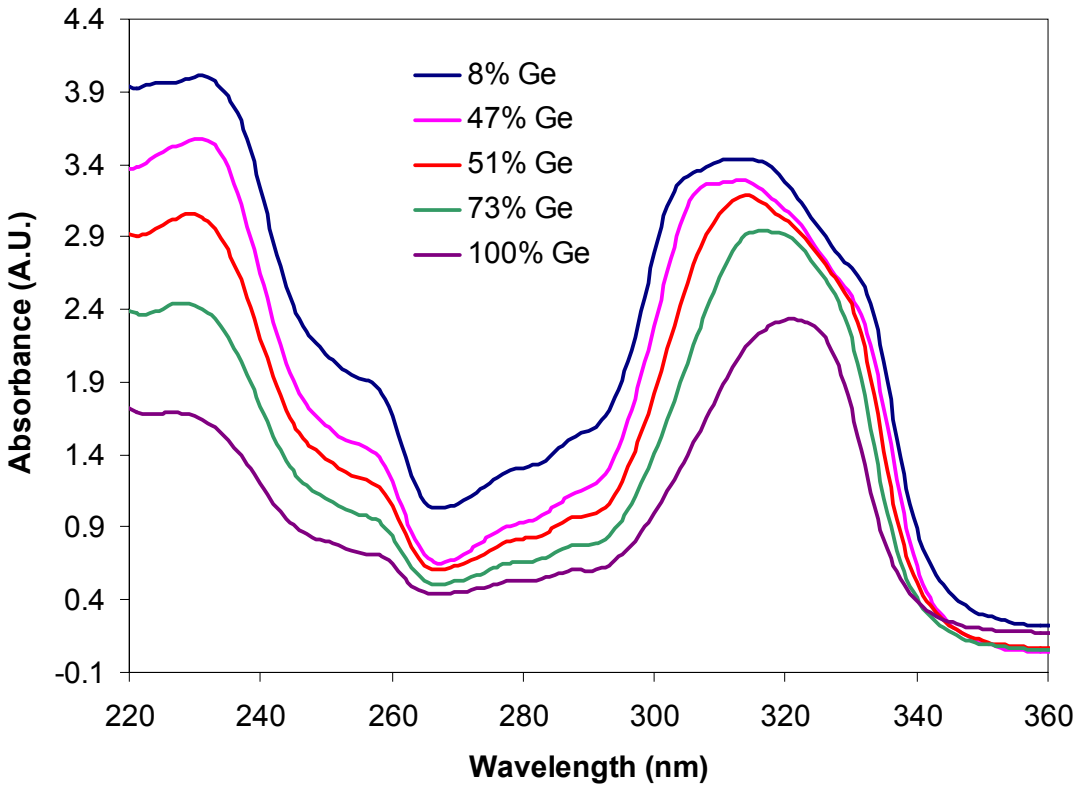

Figure 6-4: UV-Vis absorption spectra of aluminosilicogermanate (AlSiGe) nanotubes.

Furthermore, the observed optical absorption at 3.6 eV is unusual in comparison to bulk aluminosilicate materials (which have band gaps in excess of 4 eV). The role of nanoscale phenomena such as excitons [59] which give rise to a number of optical absorbances in strongly insulating boron nitride nanotubes, as well as the effects of hydroxyl groups and possible structural defects, are subjects of future investigation. Thus, the theoretical, computational, and experimental study of the electronic and optical properties of the present nanotubes, with consideration of potential nanoscale confinement effects, could yield several interesting phenomena with potential technological relevance. Additionally, the synthesis of transition metal oxide nanotubes

would allow facile control over these electronic and optical properties. Such advances in nanotube synthesis, enabled in part by the mechanistic investigations and concepts presented in this thesis, could potentially create an entirely new class of metal oxide nanotube objects that are attractive components for assembling a future generation of nanoscale electronic and photonic devices.

References

1. Rosei, F., *Nanostructured surfaces: challenges and frontiers in nanotechnology.* Journal of Physics-Condensed Matter, 2004. **16**(17): p. S1373-S1436.

2. Niemeyer, C.M., *Nanoparticles, proteins, and nucleic acids: Biotechnology meets materials science.* Angewandte Chemie-International Edition, 2001. **40**(22): p. 4128-4158.

3. Hamley, I.W., *Nanotechnology with soft materials.* Angewandte Chemie-International Edition, 2003. **42**(15): p. 1692-1712.

4. Feynman, R.P., *There is Plenty of Room at the Bottom*, in *http://www.zyvex.com/nanotech/feynman.html*. 1959. (May 2007)

5. Whitesides, G.M. and B. Grzybowski, *Self-assembly at all scales.* Science, 2002. **295**(5564): p. 2418-2421.

6. Heath, J.R., P.J. Kuekes, G.S. Snider, and R.S. Williams, *A defect-tolerant computer architecture: Opportunities for nanotechnology.* Science, 1998. **280**(5370): p. 1716-1721.

7. Vinu, A., K.Z. Hossain, and K. Ariga, *Recent advances in functionalization of mesoporous silica.* Journal of Nanoscience and Nanotechnology, 2005. **5**(3): p. 347-371.

8. Aviram, A. and M.A. Ratner, *Molecular Rectifiers.* Chemical Physics Letters, 1974. **29**(2): p. 277-283.

9. Aviram, A. and M.A. Ratner, *Molecular Rectifiers - Conceptual Basis.* Bulletin of the American Physical Society, 1974. **19**(3): p. 341-341.

10. Ratner, M.A. and A. Aviram, *Molecular Rectifiers - Model Calculations.* Bulletin of the American Physical Society, 1974. **19**(3): p. 341-341.

11. Joachim, C., J.K. Gimzewski, and A. Aviram, *Electronics using hybrid-molecular and mono-molecular devices.* Nature, 2000. **408**(6812): p. 541-548.

12. Aviram, A., *Molecules for Memory, Logic, and Amplification.* Journal of the American Chemical Society, 1988. **110**(17): p. 5687-5692.

13. Ellenbogen, J.C. and J.C. Love, *Architectures for molecular electronic computers: 1. Logic structures and an adder designed from molecular electronic diodes.* Proceedings of the Ieee, 2000. **88**(3): p. 386-426.

14. Niemeyer, C.M., *Nanotechnology: Tools for the biomolecular engineer.* Science, 2002. **297**(5578): p. 62-63.

15. Singh, A.K., V. Kumar, and Y. Kawazoe, *Design of a very thin direct-band-gap semiconductor nanotube of germanium with metal encapsulation.* Physical Review B, 2005. **71**(7).

16. Tseng, G.Y. and J.C. Ellenbogen, *Nanotechnology - Toward nanocomputers.* Science, 2001. **294**(5545): p. 1293-1294.

17. Nakane, J.J., M. Akeson, and A. Marziali, *Nanopore sensors for nucleic acid analysis.* Journal of Physics-Condensed Matter, 2003. **15**(32): p. R1365-R1393.

18. Martin, C.R. and P. Kohli, *The emerging field of nanotube biotechnology.* Nature Reviews Drug Discovery, 2003. **2**(1): p. 29-37.

19. Lieber, C.M., *One-dimensional nanostructures: Chemistry, physics & applications.* Solid State Communications, 1998. **107**(11): p. 607-616.

20. Avouris, P., *Molecular electronics with carbon nanotubes.* Accounts Of Chemical Research, 2002. **35**(12): p. 1026-1034.

21. Balasubramanian, K. and M. Burghard, *Biosensors based on carbon nanotubes.* Analytical And Bioanalytical Chemistry, 2006. **385**(3): p. 452-468.

22. Baughman, R.H., A.A. Zakhidov, and W.A. de Heer, *Carbon nanotubes - the route toward applications.* Science, 2002. **297**(5582): p. 787-792.

23. Tasis, D., N. Tagmatarchis, A. Bianco, and M. Prato, *Chemistry of carbon nanotubes.* Chemical Reviews, 2006. **106**(3): p. 1105-1136.

24. Dresselhaus, M.S., G. Dresselhaus, and A. Jorio, *Unusual properties and structure of carbonnanotubes.* Annual Review of Materials Research, 2004. **34**: p. 247-278.

25. Chen, C.M. and E.H. Peng, *Nanopore sequencing of polynucleotides assisted by a rotating electric field.* Applied Physics Letters, 2003. **82**(8): p. 1308-1310.

26. Marziali, A. and M. Akeson, *New DNA sequencing methods.* Annual Review of Biomedical Engineering, 2001. **3**: p. 195-223.

27. Lee, S.B., D.T. Mitchell, L. Trofin, T.K. Nevanen, H. Soderlund, and C.R. Martin, *Antibody-based bio-nanotube membranes for enantiomeric drug separations.* Science, 2002. **296**(5576): p. 2198-2200.

28. Duren, T., L. Sarkisov, O.M. Yaghi, and R.Q. Snurr, *Design of new materials for methane storage.* Langmuir, 2004. **20**(7): p. 2683-2689.

29. Marzan, L.L. and A.P. Philipse, *Synthesis of Platinum Nanoparticles in Aqueous Host Dispersions of Inorganic (Imogolite) Rods.* Colloids and Surfaces a-Physicochemical and Engineering Aspects, 1994. **90**(1): p. 95-109.

30. Iijima, S., *Helical Microtubules of Graphitic Carbon.* Nature, 1991. **354**(6348): p. 56-58.

31. Rao, C.N.R. and M. Nath, *Inorganic nanotubes.* Dalton Transactions, 2003(1): p. 1-24.

32. Tenne, R., *Advances in the synthesis of inorganic nanotubes and fullerene-like nanoparticles.* Angewandte Chemie-International Edition, 2003. **42**(42): p. 5124-5132.

33. Rosentsveig, R., A. Margolin, Y. Feldman, R. Popovitz-Biro, and R. Tenne, *WS2 nanotube bundles and foils.* Chemistry of Materials, 2002. **14**(2): p. 471-473.

34. Law, M., J. Goldberger, and P.D. Yang, *Semiconductor nanowires and nanotubes.* Annual Review of Materials Research, 2004. **34**: p. 83-122.

35. Remskar, M., *Inorganic nanotubes.* Advanced Materials, 2004. **16**(17): p. 1497-1504.

36. Tenne, R. and C.N.R. Rao, *Inorganic nanotubes.* Philosophical Transactions Of The Royal Society Of London Series A-Mathematical Physical And Engineering Sciences, 2004. **362**(1823): p. 2099-2125.

37. Xiong, Y.J., B.T. Mayers, and Y.N. Xia, *Some recent developments in the chemical synthesis of inorganic nanotubes.* Chemical Communications, 2005(40): p. 5013-5022.

38. Mukherjee, S., V.A. Bartlow, and S. Nair, *Phenomenology of the growth of single-walled aluminosilicate and aluminogermanate nanotubes of precise dimensions.* Chemistry of Materials, 2005. **17**(20): p. 4900-4909.

39. Tenne, R., *Inorganic nanotubes and fullerene-like nanoparticles.* Nature Nanotechnology, 2006. **1**(2): p. 103-111.

40. Wong, E.W., P.E. Sheehan, and C.M. Lieber, *Nanobeam mechanics: Elasticity, strength, and toughness of nanorods and nanotubes.* Science, 1997. **277**(5334): p. 1971-1975.

41. Ding, R.G., G.Q. Lu, Z.F. Yan, and M.A. Wilson, *Recent advances in the preparation and utilization of carbon nanotubes for hydrogen storage.* Journal of Nanoscience and Nanotechnology, 2001. **1**(1): p. 7-29.

42. Zheng, M., A. Jagota, E.D. Semke, B.A. Diner, R.S. McLean, S.R. Lustig, R.E. Richardson, and N.G. Tassi, *DNA-assisted dispersion and separation of carbon nanotubes.* Nature Materials, 2003. **2**(5): p. 338-342.

43. Tenne, R., L. Margulis, M. Genut, and G. Hodes, *Polyhedral and Cylindrical Structures of Tungsten Disulfide.* Nature, 1992. **360**(6403): p. 444-446.

44. Patzke, G.R., F. Krumeich, and R. Nesper, *Oxidic nanotubes and nanorods - Anisotropic modules for a future nanotechnology.* Angewandte Chemie-International Edition, 2002. **41**(14): p. 2446-2461.

45. Armstrong, A.R., J. Canales, and P.G. Bruce, *WO2Cl2 nanotubes and nanowires.* Angewandte Chemie-International Edition, 2004. **43**(37): p. 4899-4902.

46. Zhu, Y.Q., W.K. Hsu, H. Terrones, N. Grobert, B.H. Chang, M. Terrones, B.Q. Wei, H.W. Kroto, D.R.M. Walton, C.B. Boothroyd, I. Kinloch, G.Z. Chen, A.H. Windle, and D.J. Fray, *Morphology, structure and growth of WS2 nanotubes.* Journal of Materials Chemistry, 2000. **10**(11): p. 2570-2577.

47. Matsui, H., P. Porrata, and G.E. Douberly, *Protein tubule immobilization on self-assembled monolayers on Au substrates.* Nano Letters, 2001. **1**(9): p. 461-464.

48. Nuraje, N., I.A. Banerjee, R.I. MacCuspie, L.T. Yu, and H. Matsui, *Biological bottom-up assembly of antibody nanotubes on patterned antigen arrays.* Journal of the American Chemical Society, 2004. **126**(26): p. 8088-8089.

49. Banerjee, I.A., L.T. Yu, and H. Matsui, *Location-specific biological functionalization on nanotubes: Attachment of proteins at the ends of nanotubes using Au nanocrystal masks.* Nano Letters, 2003. **3**(3): p. 283-287.

50. Silva, G.A., C. Czeisler, K.L. Niece, E. Beniash, D.A. Harrington, J.A. Kessler, and S.I. Stupp, *Selective differentiation of neural progenitor cells by high-epitope density nanofibers.* Science, 2004. **303**(5662): p. 1352-1355.

51. Semetey, V., C. Didierjean, J.P. Briand, A. Aubry, and G. Guichard, *Self-assembling organic nanotubes from enantiopure cyclo-N,N '-linked oligoureas: Design, synthesis, and crystal structure.* Angewandte Chemie-International Edition, 2002. **41**(11): p. 1895-+.

52. Gao, X.Y. and H. Matsui, *Peptide-based nanotubes and their applications in bionanotechnology.* Advanced Materials, 2005. **17**(17): p. 2037-2050.

53. Fuhrhop, J.H. and W. Helfrich, *Fluid and Solid Fibers Made of Lipid Molecular Bilayers.* Chemical Reviews, 1993. **93**(4): p. 1565-1582.

54. Ghadiri, M.R., J.R. Granja, R.A. Milligan, D.E. McRee, and N. Khazanovich, *Self-Assembling Organic Nanotubes Based on a Cyclic Peptide Architecture.* Nature, 1993. **366**(6453): p. 324-327.

55. Desantis, P., Morosett.S, and R. Rizzo, *Conformational-Analysis of Regular Enantiomeric Sequences.* Macromolecules, 1974. **7**(1): p. 52-58.

56. Yang, P.D., H.Q. Yan, S. Mao, R. Russo, J. Johnson, R. Saykally, N. Morris, J. Pham, R.R. He, and H.J. Choi, *Controlled growth of ZnO nanowires and their optical properties.* Advanced Functional Materials, 2002. **12**(5): p. 323-331.

57. Dai, L., X.L. Chen, J.K. Jian, M. He, T. Zhou, and B.Q. Hu, *Fabrication and characterization of In2O3 nanowires.* Applied Physics a-Materials Science & Processing, 2002. **75**(6): p. 687-689.

58. Dong, W.T. and C.S. Zhu, *Use of ethylene oxide in the sol-gel synthesis of alpha-Fe2O3 nanoparticles from Fe(III) salts.* Journal of Materials Chemistry, 2002. **12**(6): p. 1676-1683.

59. Scholes, G.D. and G. Rumbles, *Excitons in nanoscale systems.* Nature Materials, 2006. **5**(9): p. 683-696.

60. Lu, J.G., P.C. Chang, and Z.Y. Fan, *Quasi-one-dimensional metal oxide materials - Synthesis, properties and applications.* Materials Science & Engineering R-Reports, 2006. **52**(1-3): p. 49-91.

61. Wen, X.G., S.H. Wang, Y. Ding, Z.L. Wang, and S.H. Yang, *Controlled growth of large-area, uniform, vertically aligned arrays of alpha-Fe2O3 nanobelts and nanowires.* Journal of Physical Chemistry B, 2005. **109**(1): p. 215-220.

62. Bae, S.Y., H.W. Seo, and J.H. Park, *Vertically aligned sulfur-doped ZnO nanowires synthesized via chemical vapor deposition.* Journal of Physical Chemistry B, 2004. **108**(17): p. 5206-5210.

63. Umar, A., S.H. Kim, Y.S. Lee, K.S. Nahm, and Y.B. Hahn, *Catalyst-free large-quantity synthesis of ZnO nanorods by a vapor-solid growth mechanism: Structural and optical properties.* Journal of Crystal Growth, 2005. **282**(1-2): p. 131-136.

64. Ichinose, I., K. Kurashima, and T. Kunitake, *Spontaneous formation of cadmium hydroxide nanostrands in water.* Journal of the American Chemical Society, 2004. **126**(23): p. 7162-7163.

65. Hulteen, J.C. and C.R. Martin, *A general template-based method for the preparation of nanomaterials.* Journal of Materials Chemistry, 1997. **7**(7): p. 1075-1087.

66. Guo, M., P. Diao, and S.M. Cai, *Hydrothermal growth of well-aligned ZnO nanorod arrays: Dependence of morphology and alignment ordering upon preparing conditions.* Journal of Solid State Chemistry, 2005. **178**(6): p. 1864-1873.

67. Wang, J.M. and L. Gao, *Wet chemical synthesis of ultralong and straight single-crystalline ZnO nanowires and their excellent UV emission properties.* Journal of Materials Chemistry, 2003. **13**(10): p. 2551-2554.

68. Liu, B. and H.C. Zeng, *Hydrothermal synthesis of ZnO nanorods in the diameter regime of 50 nm.* Journal of the American Chemical Society, 2003. **125**(15): p. 4430-4431.

69. Cao, M.H., Y.H. Wang, C.X. Guo, Y.J. Qi, C.W. Hu, and E.B. Wang, *A simple route towards CuO nanowires and nanorods.* Journal of Nanoscience and Nanotechnology, 2004. **4**(7): p. 824-828.

70. Yuan, Z.Y. and B.L. Su, *Titanium oxide nanotubes, nanofibers and nanowires.* Colloids and Surfaces a-Physicochemical and Engineering Aspects, 2004. **241**(1-3): p. 173-183.

71. Zhu, D.L., H. Zhu, and Y.H. Zhang, *Microstructure and magnetization of single-crystal perovskite manganites nanowires prepared by hydrothermal method.* Journal of Crystal Growth, 2003. **249**(1-2): p. 172-175.

72. Falini, G., E. Foresti, M. Gazzano, A.E. Gualtieri, M. Leoni, I.G. Lesci, and N. Roveri, *Tubular-shaped stoichiometric Chrysotile nanocrystals.* Chemistry-a European Journal, 2004. **10**(12): p. 3043-3049.

73. Pauling, L., *The structure of me chlorites.* Proceedings of the National Academy of Sciences of the United States of America, 1930. **16**: p. 578-582.

74. Cradwick, P.D., K. Wada, J.D. Russell, Yoshinag.N, C.R. Masson, and V.C. Farmer, *Imogolite, a Hydrated Aluminum Silicate of Tubular Structure.* Nature-Physical Science, 1972. **240**(104): p. 187-&.

75. Russel, J.D., W.J. McHardy, and A.R. Fraser, *imogolote : A unique Aluminosilicate.* Clay Minerals, 1969. **8**: p. 87-99.

76. Wada, K. and Yoshinag.N, *Structure of Imogolite.* American Mineralogist, 1969. **54**(1-2): p. 50-&.

77. Farmer, V.C., A.R. Fraser, and J.M. Tait, *Synthesis of Imogolite - Tubular Aluminum Silicate Polymer.* Journal of the Chemical Society-Chemical Communications, 1977(13): p. 462-463.

78. Farmer, V.C., B.F.L. Smith, and J.M. Tait, *Stability, Free-Energy and Heat of Formation of Imogolite.* Clay Minerals, 1979. **14**(2): p. 103-107.

79. Wada, S.I., A. Eto, and K. Wada, *Synthetic Allophane and Imogolite.* Journal of Soil Science, 1979. **30**(2): p. 347-&.

80. Wada, S. and K. Wada, *Effects of Substitution of Germanium for Silicon in Imogolite.* Clays and Clay Minerals, 1982. **30**(2): p. 123-128.

81. Schneider, C., F. Doucet, S. Strekopytov, and C. Exley, *The solubility of an hydroxyaluminosilicate.* Polyhedron, 2004. **23**(18): p. 3185-3191.

82. Mochizuki, D., A. Shimojima, T. Imagawa, and K. Kuroda, *Molecular manipulation of two- and three-dimensional silica nanostructures by alkoxysilylation of a layered silicate octosilicate and subsequent hydrolysis of alkoxy groups.* Journal of the American Chemical Society, 2005. **127**(19): p. 7183-7191.

83. Sefcik, J., S.E. Rankin, S.J. Kirchner, and A.V. McCormick, *Esterification, condensation, and deprotonation equilibria of trimethylsilanol.* Journal of Non-Crystalline Solids, 1999. **258**(1-3): p. 187-197.

84. Davis, M.E. and R.F. Lobo, *Zeolite and Molecular-Sieve Synthesis.* Chemistry of Materials, 1992. **4**(4): p. 756-768.

85. de Moor, P., T.P.M. Beelen, and R.A. van Santen, *In situ observation of nucleation and crystal growth in zeolite synthesis. A small-angle X-ray scattering investigation on Si-TPA-MFI.* Journal of Physical Chemistry B, 1999. **103**(10): p. 1639-1650.

86. Davis, T.M., T.O. Drews, H. Ramanan, C. He, J.S. Dong, H. Schnablegger, M.A. Katsoulakis, E. Kokkoli, A.V. McCormick, R.L. Penn, and M. Tsapatsis,

Mechanistic principles of nanoparticle evolution to zeolite crystals. Nature Materials, 2006. **5**(5): p. 400-408.

87. Kirschhock, C.E.A., R. Ravishankar, L. Van Looveren, P.A. Jacobs, and J.A. Martens, *Mechanism of transformation of precursors into nanoslabs in the early stages of MFI and MEL zeolite formation from TPAOH-TEOS-H2O and TBAOH-TEOS-H2O mixtures.* Journal of Physical Chemistry B, 1999. **103**(24): p. 4972-4978.

88. Knight, C.T.G., J.P. Wang, and S.D. Kinrade, *Do zeolite precursor species really exist in aqueous synthesis media?* Physical Chemistry Chemical Physics, 2006. **8**(26): p. 3099-3103.

89. Bursill, L.A., J.L. Peng, and L.N. Bourgeois, *Imogolite: an aluminosilicate nanotube material.* Philosophical Magazine a-Physics of Condensed Matter Structure Defects and Mechanical Properties, 2000. **80**(1): p. 105-117.

90. Wilson, M.A., G.S.H. Lee, and R.C. Taylor, *Tetrahedral rehydration during imogolite formation.* Journal of Non-Crystalline Solids, 2001. **296**(3): p. 172-181.

91. Exley, C., C. Schneider, and F.J. Doucet, *The reaction of aluminium with silicic acid in acidic solution: an important mechanism in controlling the biological availability of aluminium?* Coordination Chemistry Reviews, 2002. **228**(2): p. 127-135.

92. Horvath, G. and K. Kawazoe, *Method for the Calculation of Effective Pore-Size Distribution in Molecular-Sieve Carbon.* Journal of Chemical Engineering of Japan, 1983. **16**(6): p. 470-475.

93. Saito, A. and H.C. Foley, *Curvature and Parametric Sensitivity in Models for Adsorption in Micropores.* Aiche Journal, 1991. **37**(3): p. 429-436.

94. Wyn, B., *Dynamic light scattering : the method and some applications*. Monographs on the physics and chemistry of materials ; 49. 1993, Oxford [England] : New York :: Clarendon Press ; Oxford University Press,. xvi, 735 p. :.

95. Barrett, S.M., P.M. Budd, and C. Price, *The Synthesis and Characterization of Imogolite.* European Polymer Journal, 1991. **27**(7): p. 609-612.

96. Farmer, V.C., M.J. Adams, A.R. Fraser, and F. Palmieri, *Synthetic Imogolite - Properties, Synthesis, and Possible Applications.* Clay Minerals, 1983. **18**(4): p. 459-472.

97. Parent, M.A. and J.B. Moffat, *A Comparison of Methods for the Analysis of Adsorption-Desorption Isotherms of Microporous Solids.* Langmuir, 1995. **11**(11): p. 4474-4479.

98. Ackerman, W.C., D.M. Smith, J.C. Huling, Y.W. Kim, J.K. Bailey, and C.J. Brinker, *Gas Vapor Adsorption in Imogolite - a Microporous Tubular Aluminosilicate.* Langmuir, 1993. **9**(4): p. 1051-1057.

99. Gil, A. and L.M. Gandia, *Microstructure and quantitative estimation of the micropore-size distribution of an alumina-pillared clay from nitrogen adsorption at 77K and carbon dioxide adsorption at 273K.* Chemical Engineering Science, 2003. **58**(14): p. 3059-3075.

100. Yamakawa, H. and M. Fujii, *Translational Friction Coefficient of Wormlike Chains.* Macromolecules, 1973. **6**(3): p. 407-415.

101. Claire, K. and R. Pecora, *Translational and rotational dynamics of collagen in dilute solution.* Journal of Physical Chemistry B, 1997. **101**(5): p. 746-753.

102. Aragon, S.R., *Angular-Dependence of Light-Scattering Structure Coefficients for Large Anisotropic Particles.* Journal of Chemical Physics, 1980. **73**(4): p. 1576-1580.

103. Pecora, R., *Spectral Distribution of Light Scattered by Monodisperse Rigid Rods.* Journal of Chemical Physics, 1968. **48**(9): p. 4126-&.

104. Phalakornkul, J.K., A.P. Gast, and R. Pecora, *Rotational dynamics of rodlike polymers in a rod/sphere mixture.* Journal of Chemical Physics, 2000. **112**(14): p. 6487-6494.

105. Cush, R., D. Dorman, and P.S. Russo, *Rotational and translational diffusion of tobacco mosaic virus in extended and globular polymer solutions.* Macromolecules, 2004. **37**(25): p. 9577-9584.

106. Lima, A.M.D., J.T. Wong, M. Paillet, R. Borsali, and R. Pecora, *Translational and rotational dynamics of rodlike cellulose whiskers.* Langmuir, 2003. **19**(1): p. 24-29.

107. Donkai, N., H. Inagaki, K. Kajiwara, H. Urakawa, and M. Schmidt, *Dilute-Solution Properties of Imogolite.* Makromolekulare Chemie-Macromolecular Chemistry and Physics, 1985. **186**(12): p. 2623-2638.

108. Phalakornkul, J.K., A.P. Gast, and R. Pecora, *Rotational and translational dynamics of rodlike polymers: A combined transient electric birefringence and dynamic light scattering study.* Macromolecules, 1999. **32**(9): p. 3122-3135.

109. Yilgor, I., E. Yurtsever, and B. Erman, *Conformational analysis of model poly(ether urethane) chains in the unperturbed state and under external forces.* Macromolecules, 2002. **35**(26): p. 9825-9831.

110. Sauer, T. and G. Wegner, *Small-Angle X-Ray-Scattering from Dilute-Solutions of Substituted Phthalocyaninato Polysiloxanes.* Macromolecules, 1991. **24**(9): p. 2240-2252.

111. Faust, B.C., W.B. Labiosa, K.H. Dai, J.S. Macfall, B.A. Browne, A.A. Ribeiro, and D.D. Righter, *Speciation of Aqueous Mononuclear Al(Iii)-Hydroxo and Other Al(Iii) Complexes at Concentrations of Geochemical Relevance by Al-27 Nuclear-Magnetic-Resonance Spectroscopy.* Geochimica Et Cosmochimica Acta, 1995. **59**(13): p. 2651-2661.

112. Swaddle, T.W., *Silicate complexes of aluminum(III) in aqueous systems.* Coordination Chemistry Reviews, 2001. **219**: p. 665-686.

113. Little, R.B., *Mechanistic aspects of carbon nanotube nucleation and growth.* Journal of Cluster Science, 2003. **14**(2): p. 135-185.

114. Konduri, S., S. Mukherjee, and S. Nair, *Strain energy minimum and vibrational properties of single-walled aluminosilicate nanotubes.* Physical Review B, 2006. **74**(3).

115. Kan, S., T. Mokari, E. Rothenberg, and U. Banin, *Synthesis and size-dependent properties of zinc-blende semiconductor quantum rods (vol 2, pg 155, 2003).* Nature Materials, 2004. **3**(1): p. 72-72.

116. Steiner, D., D. Katz, O. Millo, A. Aharoni, S. Kan, T. Mokari, and U. Banin, *Zero-dimensional and quasi one-dimensional effects in semiconductor nanorods.* Nano Letters, 2004. **4**(6): p. 1073-1077.

117. Yu, H., J.B. Li, R.A. Loomis, L.W. Wang, and W.E. Buhro, *Two- versus three-dimensional quantum confinement in indium phosphide wires and dots.* Nature Materials, 2003. **2**(8): p. 517-520.

118. Chen, S.J., Y.C. Liu, C.L. Shao, C.S. Xu, Y.X. Liu, C.Y. Liu, B.P. Zhang, L. Wang, B.B. Liu, and G.T. Zou, *Photoluminescence study of ZnO nanotubes under hydrostatic pressure.* Applied Physics Letters, 2006. **88**(13).

119. Wirtz, L., A. Marini, and A. Rubio, *Excitons in boron nitride nanotubes: Dimensionality effects.* Physical Review Letters, 2006. **96**(12).

120. Tamura, K. and K. Kawamura, *Molecular dynamics modeling of tubular aluminum silicate: Imogolite.* Journal of Physical Chemistry B, 2002. **106**(2): p. 271-278.

121. Mintova, S., N.H. Olson, V. Valtchev, and T. Bein, *Mechanism of zeolite a nanocrystal growth from colloids at room temperature.* Science, 1999. **283**(5404): p. 958-960.

122. Cheng, C.H. and D.F. Shantz, *Nanoparticle formation and zeolite growth in TEOS/organocation/water solutions.* Journal Of Physical Chemistry B, 2005. **109**(15): p. 7266-7274.

123. Kragten, D.D., J.M. Fedeyko, K.R. Sawant, J.D. Rimer, D.G. Vlachos, R.F. Lobo, and M. Tsapatsis, *Structure of the silica phase extracted from silica/(TPA)OH solutions containing nanoparticles.* Journal Of Physical Chemistry B, 2003. **107**(37): p. 10006-10016.

124. Shimizu, L.S., A.D. Hughes, M.D. Smith, M.J. Davis, B.P. Zhang, H.C. zur Loye, and K.D. Shimizu, *Self-assembled nanotubes that reversibly bind acetic acid guests.* Journal of the American Chemical Society, 2003. **125**(49): p. 14972-14973.

125. Navrotsky, A., *Energetic clues to pathways to biomineralization: Precursors, clusters, and nanoparticles.* Proceedings Of The National Academy Of Sciences Of The United States Of America, 2004. **101**(33): p. 12096-12101.

126. Rimer, J.D., D.D. Roth, D.G. Vlachos, and R.F. Lobo, *Self-assembly and phase behavior of germanium oxide nanoparticles in basic aqueous solutions.* Langmuir, 2007. **23**(5): p. 2784-2791.

127. Drews, T.O., M.A. Katsoulakis, and M. Tsapatsis, *A mathematical model for crystal growth by aggregation of precursor metastable nanoparticles.* Journal of Physical Chemistry B, 2005. **109**(50): p. 23879-23887.

128. Nikolakis, V., E. Kokkoli, M. Tirrell, M. Tsapatsis, and D.G. Vlachos, *Zeolite growth by addition of subcolloidal particles: Modeling and experimental validation.* Chemistry Of Materials, 2000. **12**(3): p. 845-853.

129. Jolivet, J.-P., *Metal Oxide Chemistry and Synthesis: From Solution to Solid State*. 2003, West Sussex, England: Wiley.

130. Alivisatos, A.P., *Semiconductor clusters, nanocrystals, and quantum dots.* Science, 1996. **271**(5251): p. 933-937.

131. Brus, L.E., *Electron Electron and Electron-Hole Interactions in Small Semiconductor Crystallites - the Size Dependence of the Lowest Excited Electronic State.* Journal of Chemical Physics, 1984. **80**(9): p. 4403-4409.

132. Peng, X.G., L. Manna, W.D. Yang, J. Wickham, E. Scher, A. Kadavanich, and A.P. Alivisatos, *Shape control of CdSe nanocrystals.* Nature, 2000. **404**(6773): p. 59-61.

133. Balevicius, V. and H. Fuess, *Ion induced hypercritical point in tetrahydrofuran/water solutions.* Chemical Physics Letters, 2003. **377**(5-6): p. 530-536.

134. MacDonald, S.A., C.R. Schardt, D.J. Masiello, and J.H. Simmons, *Dispersion analysis of FTIR reflection measurements in silicate glasses.* Journal of Non-Crystalline Solids, 2000. **275**(1-2): p. 72-82.

135. Meneses, D.D., M. Malki, and P. Echegut, *Structure and lattice dynamics of binary lead silicate glasses investigated by infrared spectroscopy.* Journal of Non-Crystalline Solids, 2006. **352**(8): p. 769-776.

136. Mukherjee, S., K. Kim, and S. Nair, *Short, Highly Ordered, Single-Walled Mixed-Oxide Nanotubes Assemble from Amorphous Nanoparticles.* Journal of American Chemical Society, 2007. **129**(21): p. 6820-6826.

137. Imamura, S., T. Kokubu, T. Yamashita, Y. Okamoto, K. Kajiwara, and H. Kanai, *Shape-selective copper-loaded Imogolite catalyst.* Journal of Catalysis, 1996. **160**(1): p. 137-139.

138. Ohashi, F., S. Tomura, K. Akaku, S. Hayashi, and S.I. Wada, *Characterization of synthetic imogolite nanotubes as gas storage.* Journal of Materials Science, 2004. **39**(5): p. 1799-1801.

139. Kong, C.Y. and M. Muthukumar, *Modeling of polynucleotide translocation through protein pores and nanotubes.* Electrophoresis, 2002. **23**(16): p. 2697-2703.

140. Gao, H.J., Y. Kong, D.X. Cui, and C.S. Ozkan, *Spontaneous insertion of DNA oligonucleotides into carbon nanotubes.* Nano Letters, 2003. **3**(4): p. 471-473.

141. Kalra, A., S. Garde, and G. Hummer, *Osmotic water transport through carbon nanotube membranes.* Proceedings of the National Academy of Sciences of the United States of America, 2003. **100**(18): p. 10175-10180.

142. Hummer, G., J.C. Rasaiah, and J.P. Noworyta, *Water conduction through the hydrophobic channel of a carbon nanotube.* Nature, 2001. **414**(6860): p. 188-190.

143. Kozerski, G.E., R.H. Gallavan, and M.J. Ziemelis, *Investigation of trialkoxysilane hydrolysis kinetics using liquid chromatography with inductively coupled plasma atomic emission spectrometric detection and non-linear regression modeling.* Analytica Chimica Acta, 2003. **489**(1): p. 103-114.

144. Rankin, S.E., J. Sefcik, and A.V. McCormick, *Trimethylethoxysilane liquid-phase hydrolysis equilibrium and dimerization kinetics: Catalyst, nonideal mixing, and the condensation route.* Journal of Physical Chemistry A, 1999. **103**(21): p. 4233-4241.

145. Vegas, A. and R. Isea, *The cation array of the oxyhydroxides of trivalent metals.* Journal of Solid State Chemistry, 1997. **131**(2): p. 358-362.

146. Li, L.S., J.T. Hu, W.D. Yang, and A.P. Alivisatos, *Band gap variation of size- and shape-controlled colloidal CdSe quantum rods.* Nano Letters, 2001. **1**(7): p. 349-351.

147. Longeaud, C., J.A. Schmidt, and R.R. Koropecki, *Determination of semiconductor band gap state parameters from photoconductivity measurements. II. Experimental results.* Physical Review B, 2006. **73**(23).

148. Yu, Z.Q., C.X. Wang, X.T. Gu, and C. Li, *Photoluminescent properties of boehmite whisker prepared by sol-gel.* Journal of Luminescence, 2004. **106**(2): p. 153-157.

149. Ruckschloss, M., T. Wirschem, H. Tamura, G. Ruhl, J. Oswald, and S. Veprek, *Photoluminescence from Oh-Related Radiative Centers in Silica, Metal-Oxides and Oxidized Nanocrystalline and Porous Silicon.* Journal of Luminescence, 1995. **63**(5-6): p. 279-287.

150. Pedraza, A.J., *Interaction of UV laser light with wide band gap materials: Mechanisms and effects.* Nuclear Instruments & Methods in Physics Research Section B-Beam Interactions with Materials and Atoms, 1998. **141**(1-4): p. 709-718.